

MEASUREMENT OF AILERON HINGE MOMENTS AND THE EFFECT OF AILERON TRAILING EDGE THICKNESS

Sjouke Willem Schekman

A dissertation submitted to the Faculty of Engineering and the Built Environment, University of the Witwatersrand, Johannesburg, in fulfilment of the requirements for the degree of Master of Science in Engineering.

Johannesburg, July-2015

DECLARATION

I declare that this dissertation is my own, unaided work, except where otherwise acknowledged. It is being submitted for the degree Master of Science in Engineering in the University of the Witwatersrand, Johannesburg. It has not been submitted before for any degree or examination at any other university.

Signed this 23 July 2015

A handwritten signature in black ink, appearing to read 'Sjouke', written over a horizontal line.

Sjouke Willem Schekman

ABSTRACT

The objective of this research was twofold. The first objective was for the design and testing of a compact force measurement device, capable of fitting inside the wind tunnel model and measuring aileron hinge moments. Using the hinge moment balance, the second objective was to test the effect of varying the trailing edge thickness of the aileron. A plain type aileron, with a 20.6% chord and 40% span, was attached to a NACA 0012 wing. Four aileron test pieces with trailing edge thicknesses from 0.39%*c* to 1.22%*c* were used. An external balance capable of measuring the wing rolling and yawing moments was used in conjunction with the hinge moment balance. Validation of the results and performance of the hinge moment balance was done by comparisons to the data obtained from previous research and investigations using flow visualization. The results indicated that the system performed in a manner that was expected and predictable. The data from the hinge moment balance had an uncertainty of 4.2% which was deemed satisfactory for the purposes of this research. For the majority of the test cases the effects of the varied trailing edge thickness was found to be negligible. Small differences were noted at high angles of attack, above 15°, and high aileron deflections, above 20°. As these conditions were seen to be outside the typical flight envelope of general aviation aircraft, these small differences were seen as inconsequential. It was concluded that the use of an aileron with a thicker trailing edge would not have a negative effect on the performance of the aileron while allowing for less restrictions on the manufacture of the aileron itself.

TABLE OF CONTENTS

Declaration.....	ii
Abstract.....	iii
Table of Contents.....	iv
List of Figures.....	vii
List of Tables.....	xii
1 Introduction.....	1
1.1 Background.....	1
1.2 Motivation.....	4
1.3 Objectives.....	4
2 Literature Survey.....	5
2.1 Previous Research.....	5
2.1.1 Blunt Trailing Edges.....	6
2.1.2 Data Accuracy.....	10
2.1.3 Testing Methodology.....	10
2.2 Aileron Performance Characterization.....	11
2.2.1 Rolling Performance.....	11
2.2.2 Adverse Yaw.....	12
2.2.3 Control Loads.....	13
2.3 Low Reynolds Number Testing.....	13
2.4 Hinge Moment Measurement Techniques.....	15
2.5 Test Model Configurations.....	17
3 Method.....	18
3.1 Test Matrix.....	18
3.2 Test Equipment Requirements.....	19
4 Facilities and equipment.....	20
4.1 Wind tunnel.....	21
4.2 External Balance.....	22
4.3 Test Model.....	25
4.3.1 Design.....	25
4.3.2 Manufacture.....	26

4.3.3	Lateral Control Device.....	27
4.3.4	Hinge Moment Balance.....	30
4.4	Data Acquisition.....	31
4.4.1	Data Acquisition Device (DAQ).....	31
4.4.2	Atmospheric Data	32
4.4.3	Power Supply	33
4.4.4	Wiring	34
4.5	Flow Visualization.....	34
5	Data Processing.....	35
6	Error Propagation.....	37
6.1	Data Uncertainty.....	37
6.2	Signal Sensitivity.....	37
6.2.1	Loadcells Signal Sensitivity	37
6.2.2	Potentiometer Signal Sensitivity	39
6.2.3	Ghosting Effect	40
6.2.4	Signal Drift.....	41
6.3	Data Distribution and Manipulation	42
7	Calibration.....	44
7.1	External Balance Calibration.....	44
7.2	Hinge Moment Calibration.....	47
7.3	Aileron Deflection.....	49
8	Results and Discussion.....	51
8.1	Typical Data Set	51
8.2	Flow Visualization Results.....	56
8.3	Comparisons to Previous Research	62
8.4	Variation of Aileron Trailing Edge Thickness	68
9	Conclusions.....	80
10	Recommendations	81
11	References.....	82
	Appendix A : Previous Research Data.....	87
	Appendix B : Engineering Drawings	91

Appendix C : Equipment Datasheets	102
Appendix D : Derivation of Uncertainty	115
Appendix E : Loadcell Sensitivity Check Setup and Procedures.....	118
E.1. External Balance Loadcells	118
E.2. Hinge Moment Balance Loadcell	118
Appendix F : Calibration Setup and Procedures	120
F.1. External Balance.....	120
F.2. Hinge Moment Balance	121
F.3. Aileron Deflection	122
Appendix G : external Balance Cross Coupling Effect.....	124
Appendix H : Test Precautions	125
Appendix I : Full List of Results.....	126

LIST OF FIGURES

Figure 1.1: Three different trailing edge angles (Toll, 1946).....	1
Figure 1.2: Frequency and distribution of previous publications.....	2
Figure 2.1: Plain Flap Type Aileron indicating definition of aileron chord used in calculations (Rogallo & Purser, 1941).....	6
Figure 2.2: Examples of Frise ailerons investigated in previous tests (Toll, 1946).....	6
Figure 2.3: Lift of an 0018 airfoil with and without a blunt trailing edge, produced by cutting off the trailing edge (Hoerner & Borst, 1985).....	7
Figure 2.4: Change in drag coefficient of a streamline body brought on by removal of bodies trailing edge (Hoerner, 1965).....	8
Figure 2.5: Typical aerofoil profile used when investigating thickened trailing edges (van Dam & Kahn, 2008).....	9
Figure 2.6: Example of Gurney Flap and Trailing Edge T-Strip (Cavanaugh, et al., 2007).....	9
Figure 2.7: Example of Divergent Trailing Edge (Kroo, 2004).....	9
Figure 2.8: Aerofoil data for NACA 0012 conducted for a range of Reynolds numbers between 170 000 and 3 180 0000 (Jacobs & Sherman, 1937).....	14
Figure 2.9: Separation occurring on an airfoil at a low angle of attack, at low a Reynolds number (a) and an increased Reynolds number (b) (van Dyke, 2005).....	15
Figure 2.10: Previously used Hinge Moment Measurement Arrangement (Monish, 1930).....	16
Figure 2.11: Test setup as used by Rogallo (Rogallo & Lowry, 1942).....	16
Figure 2.12: Cable-tension recorder as employed by Goranson (1946) during flight tests.....	17
Figure 4.1 Wind tunnel cross section and internal dimensions.....	21
Figure 4.2: External Balance Axis System.....	21
Figure 4.3 External Balance Isometric View.....	24
Figure 4.4: External Balance 3 View.....	24
Figure 4.5 Wing Alignment Plate.....	25
Figure 4.6: Half wing cut-outs.....	27
Figure 4.7: Aileron profile to be tested.....	27
Figure 4.8: Aileron Design.....	29
Figure 4.9: Internal Hinge Moment Balance Configuration.....	30
Figure 5.1: Property mapping due inversion of the wing about the x-y plane.....	36
Figure 6.1: Variation in yawing moment loadcell signal, measured in $\mu\epsilon$, with an increase in mass directly applied to the loadcell.....	38
Figure 6.2: Variation in hinge moment loadcell signal, measured in $\mu\epsilon$, with an increase in mass directly applied to the loadcell.....	39
Figure 6.3: Change in loadcell signals, measured in $\mu\epsilon$, recorded for each loadcell when a yawing moment was applied.....	40
Figure 6.4: Variation of rolling moment loadcell signal over a 20 hour period plotted against the variation in ambient air temperature over the same time.....	41

Figure 6.5: Distribution of rolling moment raw signal data, measured in $\mu\epsilon$, obtained from a single test plotted against a Gaussian distribution, 15° AoA, Thickness 2, $\delta=-10^\circ$, $V=14.7\text{m/s}$.	42
Figure 6.6: Comparison of raw and filtered rolling moment signal data from example test, 15° AoA, $\delta=10^\circ$, $V=14.5\text{m/s}$. Lowpass filter of 5Hz applied.	43
Figure 7.1: Rolling moment calibration results for the rolling moment loadcell	44
Figure 7.2: Rolling moment calibration results for the yawing moment loadcell	46
Figure 7.3: Hinge moment balance calibration plot	47
Figure 7.4: Aileron deflection calibration plot of deflection against voltage recorded	49
Figure 8.1: Zeroed yawing moment loadcell signals, including reversed signals, -5° and $+5^\circ$ AoA, plain sealed aileron, Thickness 2, $V=14.6\text{m/s}$.	52
Figure 8.2: Comparison of data before and after application of calibration for yawing moment loads at 5° AoA, plain sealed aileron, Thickness 2, $V=14.6\text{m/s}$	54
Figure 8.3: Comparison of data before and after application of calibration for rolling moment loads at 5° AoA, plain sealed aileron, Thickness 2, $V=14.6\text{m/s}$	55
Figure 8.4: Yawing Moment Coefficients at 5° AoA, Thickness 2, $V=14.6\text{m/s}$	55
Figure 8.5: Variation of hinge moment strain uncertainty with aileron deflection for 5° and 10° AoA, Thickness 2, $V=14.6\text{m/s}$	56
Figure 8.6: Rolling moment coefficient trend (a) and corresponding flow field (b) for 12.5° AoA, Thickness 2, $V=14.6\text{m/s}$	57
Figure 8.7: Rolling moment coefficient trend (a) and corresponding flow field (b) for 15° AoA, Thickness 2, $V=14.5\text{m/s}$	58
Figure 8.8: Flow visualization at 12.5° AoA, aileron deflection at -30° (a) and $+30^\circ$ (b), Thickness 2, $V=14.7\text{m/s}$	59
Figure 8.9: Rolling moment coefficient trend (a) and corresponding flow field (b) for 20° AoA, Thickness 2, $V=14.8\text{m/s}$	60
Figure 8.10: Rolling moment coefficients with modified trend line for 20° AoA, Thickness 2, $V=14.8\text{m/s}$	61
Figure 8.11: Hinge Moment Coefficients for a NACA 0012 at 12.5° AoA, plain sealed 0.206c 0.4b/2 aileron Thickness 2, $V=14.6\text{m/s}$	62
Figure 8.12: Comparison between delta rolling moment coefficients for primary test data, Thickness 2, 10° AoA, $V=14.7\text{m/s}$, and data obtained from Rogallo (1941).	64
Figure 8.13: Comparison between delta yawing moment coefficients for primary test data, Thickness 2, and data obtained from Rogallo (1941), 10° AoA, $V=14.7\text{m/s}$.	66
Figure 8.14: Comparison between hinge moment coefficients for primary test data, Thickness 2, and data obtained from Rogallo (1941), 10° AoA, $V=14.7\text{m/s}$.	67
Figure 8.15: Comparison of delta rolling moment coefficients for 4 aileron trailing edge thicknesses, 5° AoA, $V=14.6\text{m/s}$	70
Figure 8.16: Comparison of delta rolling moment coefficients for 4 aileron trailing edge thicknesses, 5° , 12.5° and 15° AoA, $V=14.6\text{m/s}$	71

Figure 8.17: Comparison of delta rolling moment coefficients for 4 aileron trailing edge thicknesses, 20° AoA, V=14.8m/s	72
Figure 8.18: Delta yawing moment coefficient trends for each AoA, aileron Thickness 2, V=14.8m/s	73
Figure 8.19: Comparison of delta yawing moment coefficients for 4 aileron trailing edge thicknesses, 5° AoA, V=14.6m/s	74
Figure 8.20: Comparison of delta yawing moment coefficients for 4 aileron trailing edge thicknesses, 15° AoA, V=14.5m/s	75
Figure 8.21: Comparison of delta yawing moment coefficients for 4 aileron trailing edge thicknesses, 20° AoA, V=14.8m/s	75
Figure 8.22: Comparison of delta yawing moment coefficient variation with delta rolling moment coefficient, for 4 aileron trailing edge thicknesses, 5° AoA, V=14.6m/s.....	76
Figure 8.23: Comparison of delta yawing moment coefficient variation with delta rolling moment coefficient, for 4 aileron trailing edge thicknesses, 20° AoA, V=14.8m/s.....	76
Figure 8.24: Comparison of hinge moment coefficients for 4 aileron trailing edge thicknesses, 5° AoA, V=14.6m/s	77
Figure 8.25: Comparison of hinge moment coefficients for 4 aileron trailing edge thicknesses, 15° AoA, V=14.5m/s	77
Figure 8.26: Comparison of hinge moment coefficients for 4 aileron trailing edge thicknesses, 20° AoA, V=14.8m/s	78
Figure A.1: Aerodynamic characteristics of a 0.20c by 0.37 b/2 plain grease-sealed aileron without balance on an NACA 23012 airfoil. V, 40mph (Rogallo & Purser, 1941)	87
Figure A.2: Typical rolling and hinge moment coefficient curves for plain ailerons (Jones & Weick, 1937).....	88
Figure A.3: Aerofoil section characteristics of a NACA0012 as affected by variations of the Reynolds number (Jacobs & Sherman, 1937).....	89
Figure A.4: Separation occurring on an airfoil at a low angle of attack, at low a Reynolds number (a) and an increased Reynolds number (b) (Jacobs & Sherman, 1937)	90
Figure B.1: External Balance ISO View	92
Figure B.2: External Balance 3 View	93
Figure B.3: External Balance Cage.....	94
Figure B.4: Balance Arm	95
Figure B.5: Wing Alignment Plate	96
Figure B.6: Wing Assembly.....	97
Figure B.7: Wing Half	98
Figure B.8: Aileron Assembly	99
Figure B.9: Hinge Moment Balance Overview.....	100

Figure B.10: Hinge Moment Balance	101
Figure E.1: Setup used in the calibration of the hinge moment loadcell through the application of load directly to the loadcell.....	119
Figure F.1: Calibration setup used for rolling moment calibration	120
Figure F.2: External Balance calibration configuration	121
Figure F.3: Hinge moment balance calibration setup.....	122
Figure F.4: Aileron Deflection calibration configuration	123
Figure G.1: Diagram explaining yawing moment load direction depending on applied rolling moment direction	124
Figure I.1: Comparison of delta rolling moment coefficients for 4 aileron trailing edge thicknesses, 0° AoA, V=14.9m/s	126
Figure I. 2: Comparison of delta rolling moment coefficients for 4 aileron trailing edge thicknesses, 5° AoA, V=14.6m/s	126
Figure I. 3: Comparison of delta rolling moment coefficients for 4 aileron trailing edge thicknesses, 10° AoA, V=14.7m/s	127
Figure I. 4: Comparison of delta rolling moment coefficients for 4 aileron trailing edge thicknesses, 12.5° AoA, V=14.6m/s	127
Figure I. 5: Comparison of delta rolling moment coefficients for 4 aileron trailing edge thicknesses, 15° AoA, V=14.5m/s	128
Figure I. 6: Comparison of delta rolling moment coefficients for 4 aileron trailing edge thicknesses, 17.5° AoA, V=14.7m/s	128
Figure I. 7: Comparison of delta rolling moment coefficients for 4 aileron trailing edge thicknesses, 20° AoA, V=14.8m/s	129
Figure I. 8: Comparison of delta yawing moment coefficients for 4 aileron trailing edge thicknesses, 0° AoA, V=14.9m/s	129
Figure I. 9: Comparison of delta yawing moment coefficients for 4 aileron trailing edge thicknesses, 5° AoA, V=14.6m/s	130
Figure I. 10: Comparison of delta yawing moment coefficients for 4 aileron trailing edge thicknesses, 10° AoA, V=14.7m/s	130
Figure I. 11: Comparison of delta yawing moment coefficients for 4 aileron trailing edge thicknesses, 12.5° AoA, V=14.6m/s	131
Figure I. 12: Comparison of delta yawing moment coefficients for 4 aileron trailing edge thicknesses, 15° AoA, V=14.5m/s	131

Figure I. 13: Comparison of delta yawing moment coefficients for 4 aileron trailing edge thicknesses, 17.5° AoA, V=14.7m/s	132
Figure I. 14: Comparison of delta yawing moment coefficients for 4 aileron trailing edge thicknesses, 20° AoA, V=14.8m/s	132
Figure I. 15: Comparison of hinge moment coefficients for 4 aileron trailing edge thicknesses, 0° AoA, V=14.9m/s	133
Figure I. 16: Comparison of hinge moment coefficients for 4 aileron trailing edge thicknesses, 5° AoA, V=14.6m/s	133
Figure I. 17: Comparison of hinge moment coefficients for 4 aileron trailing edge thicknesses, 10° AoA, V=14.7m/s	134
Figure I. 18: Comparison of hinge moment coefficients for 4 aileron trailing edge thicknesses, 12.5° AoA, V=14.6m/s	134
Figure I. 19: Comparison of hinge moment coefficients for 4 aileron trailing edge thicknesses, 15° AoA, V=14.5m/s	135
Figure I. 20: Comparison of hinge moment coefficients for 4 aileron trailing edge thicknesses, 17.5° AoA, V=14.7m/s	135
Figure I. 21: Comparison of hinge moment coefficients for 4 aileron trailing edge thicknesses, 20° AoA, V=14.8m/s	136

LIST OF TABLES

Table 4.1: Aileron Trailing Edge Thicknesses	28
Table 6.1: Approximate loads and change in signal values to be measured by each of the three loadcells during testing.	39
Table E.1: Mass loads applied during calibration of sting balance loadcells.....	118
Table E.2: Mass loads applied during direct calibration of hinge moment loadcell	118
Table F.1: Moment arms and masses applied during calibration.....	121
Table F.2: Moment loads applied during calibration of hinge moment measurement balance.	122

1 INTRODUCTION

1.1 Background

The previous research into aileron performance has typically focused on the measurement of the rolling, yawing and hinge moments produced by an aileron during flight conditions. The hinge moment characteristics of ailerons have been found to be heavily dependent on the aileron contour near the trailing edge (Toll, 1946). The manipulation of the aileron trailing edge, during experiments in the past, centred primarily on the aileron trailing edge angle, as shown in Figure 1.1. In all cases, especially the work undertaken by the N.A.C.A., a thin aileron trailing edge was desired and used. From the 1980's onwards there has been an increased interest in the application of blunt trailing edges.

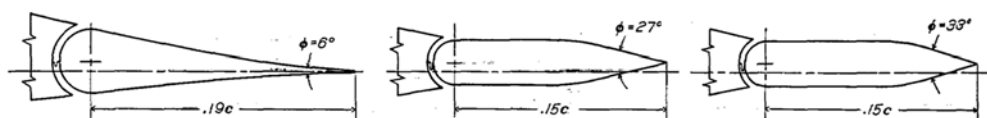


Figure 1.1: Three different trailing edge angles (Toll, 1946).

Research into the area of aileron design for low speed aircraft has remained relatively stagnant ever since. Alternatives to conventional ailerons have been investigated and include the use of wing warping and fluidic flow control (Shrouder, 2010). These methods, however, are complex and expensive to implement. General aviation and light sport aircraft, therefore, still make use of the conventional aileron type which was first implemented in 1908 by Glenn Curtiss (Abzug & Larrabee, 2002).

Publications from the 1930's to 2015 have been reviewed, covering two primary topics: the measurement of aileron hinge moments and characterisation of aileron performance from these measurements, and the use of blunt trailing edges on ailerons. A summary of the frequency and distribution of these publications, over this time frame, for these two topics is shown in Figure 1.2. This summary was compiled from a review of papers published through N.A.C.A., the AIAA, the journal of Experiments in Fluids, ICAS and the journal of Measurement Sciences and Technology. Further searches were made through search engines such as Google Scholar, Scopus and Engineering Village. Key phrases used were aileron (or elevator, elevon and rudder), hinge moment and blunt trailing edge. This dissertation was to focus on the application of aileron research for general aviation aircraft. This meant that test conditions would deal with sub-sonic test cases and only research covering such flight regimes would be of use.

The majority of research done into aileron hinge moments was made during the 1930's and 1940's. This research was conducted under the National Advisory Committee for Aeronautics (N.A.C.A.) by authors such as Fred Weick, Abe Silverstein and S. Katzoff. The tests encompassed the use of wind tunnel tests, analytical investigations and flight tests for subsonic

low speed cases. From the 1950's onwards the research focused on lateral control effectiveness when travelling at transonic and supersonic speeds. This includes works by Xu et al (2011), Tamayama et al (2003) and Pezzella et al (2014). The interest in ailerons at these speeds focused on the behaviour of the ailerons in the presence of shock waves, typically resulting in aileron buzz. These papers were then looking into ways of modelling and manipulating the phenomenon, which is not relevant to general aviation aircraft and as such this current research. The later research for subsonic speed cases, was done on the lateral control characteristics of a particular aircraft, such as the Curtis P-40 Warhawk (Goranson, 1946), the Northrop M2-F2 lifting body (Kempel, 1971) and Boeing 727 (Nagaraja , et al., 1982). Other research, into hinge moment measurement covered specific effects such as that which icing has on the hinge moments (Gurbacki & Bragg, 2001); the increase in unsteady hinge moments resulting in a satisfactory indicator of ice build-up, this in turn allowing for possible early warning systems to be developed. Extrapolating meaningful information from the results in order to aid in the validation of results or for the comparison of results would have been difficult. It would also have been unnecessary as the earlier work covered sufficient information for these purposes.

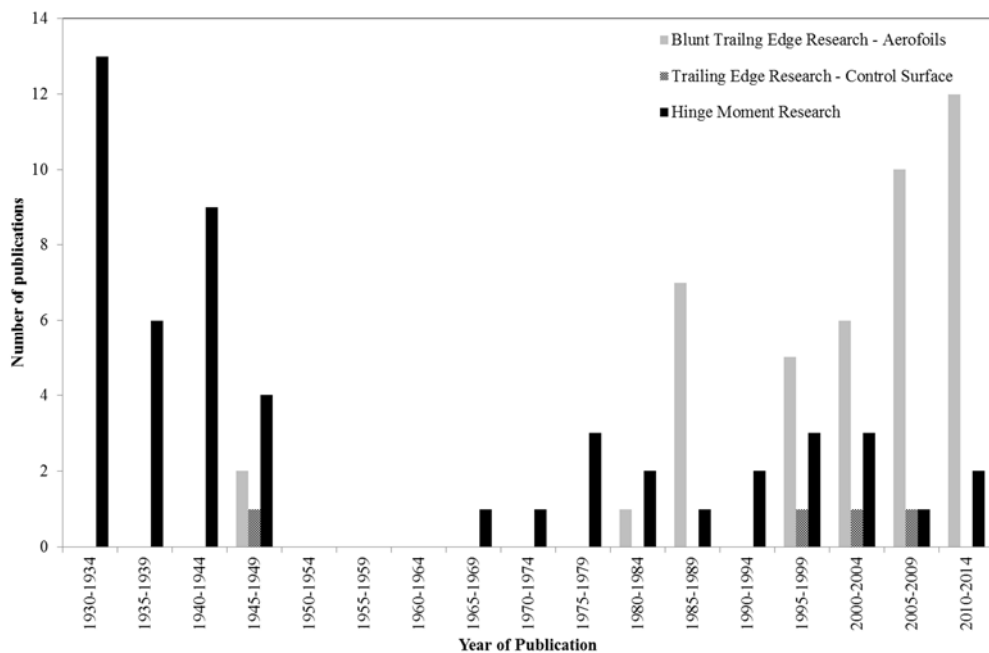


Figure 1.2: Frequency and distribution of previous publications

Interest in blunt trailing edges increased from the 1980's onwards. Earlier work had been conducted however it seems a practical application of blunt trailing edges only was properly realised in the late 20th century. The majority of this research did not, however, focus on the application of blunt trailing edges to control surfaces. Most of the research focused on applications for thick aerofoils used in wind turbines or on supercritical aerofoils. This includes research by Gammal et al (2010), Cooperman et al (2010) and Standish & van Dam (2003). The results of these publications and their relevance to applications for ailerons will be discussed in later sections. No publications could be found on the application of blunt trailing

edges to ailerons. Those reports, in the Figure 1.2, referring to control surface trailing edge research are either for the use of a blunt trailing edge on a slat (Khorrami, et al., 2000) or for other trailing edge modifications (serrated edges rather than blunt trailing edges (Lemes & Catalano, 2004)). A report was found from 1950, published by NACA, for the application of blunt trailing edges on an aileron, however this was for a super-sonic case; the blunt trailing edge eliminated the occurrence of control reversal during the transonic range (Strauss & Fields, 1950). As control reversal is not a factor that needs considering for general aviation this data is therefore of little use in the current scope of research.

1.2 Motivation

The manipulation of control surface hinge moments in aircraft has its advantages. Regulations, such as FAR 23.395, state minimum design factors that need be applied to the computed aileron hinge moment when designing the control system for an aircraft. Regulations also exist for limiting the maximum allowable force or torque that a pilot can be expected to apply. By manipulating the hinge moment required, the system can therefore be designed more efficiently. This could result in the possibility of a lighter and/or cheaper control system. Basic aircraft performance analysis techniques, such as those suggested by Torenbeek (1976), show that an aircraft with a lower mass, due to a lighter actuation system, would be capable of carrying a larger payload, or for the same load it would use less fuel. The lowering of the mass of the actuation system would in some part reduce the rolling mass moment of inertia of the wing; allowing for a more responsive aircraft. A decrease in the hinge moments of a particular aileron could potentially allow for an aileron with a larger span to be used; aileron hinge moments being proportional to the aileron span. Conversely an increase in hinge moments would allow for smaller ailerons and therefore the use of larger flaps which would improve the take-off and landing performance of the aircraft.

One area that remains relatively untested in the manipulation of aileron hinge moments deals with the aileron trailing edge thickness. A general trend with the design of aerofoils for general aviation aircraft is to have them manufactured with thin, sharp trailing edges. This is reflected in the common reference to theoretical aerodynamics such as the Kutta condition. The issue is that the requirement for a sharp trailing edge increases the difficulty in the manufacturing of the aileron. The use of blunt trailing edges on wings has been investigated previously, with works by Hoerner (1950) and Baker (2008). Their work showed that blunt trailing edges offered an increase in the maximum lift produced by a wing along with an increase in the aerodynamic drag. Hoerner commented on the possible application of these effects on the performance of ailerons (Hoerner & Borst, 1985). By allowing for a thicker trailing edge, the aileron manufacturing costs and complexity could be reduced. There is, then, merit in the investigation into the use of ailerons with thicker trailing edges.

1.3 Objectives

The following objectives were undertaken for the research specified in this dissertation.

1. Design and test a hinge moment balance capable of accurately measuring the aileron hinge moments that occur.
2. Compare and validate the results obtained from the hinge moment balance with those obtained from previous tests.
3. Investigate the effect of a change in the aileron trailing edge thickness on the aileron performance.

2 LITERATURE SURVEY

2.1 Previous Research

The previous research into aileron performance has been extensive. As stated in the previous chapter, the majority of the research, that is pertinent to this dissertation, was conducted in the 1930's and 1940's. The experiments conducted by Toll, Wenzinger, Katzoff, and Heald, among others, looked at various aspects of aileron performance. These included:

- The effectiveness of ailerons at high angles of attack (Wenzinger & Weick, 1932)
- Adverse yaw affects (Heald, 1933)
- Lateral stability (Toll, 1946)
- The downwash and wake behind ailerons (Katzoff, et al., 1938)
- Auto rotation tests (Toll, 1946)
- Effect of wing shape (Wenzinger, 1937), (Shortal & Weick, 1933)
- The lift distribution over ailerons (Bacon, 1924)
- Effect of altitude (Toll, 1946)
- Application of roughness strips on the aileron trailing edges (Toll, 1946)
- Aileron oscillations (Toll, 1946)
- Effect of balancing and sealing (Sears, 1942), (Rogallo & Purser, 1941)

Throughout the above mentioned experiments, multiple lateral control types were investigated. This included, but was not limited to, the following aileron types:

- Plain flap (ordinary) (Wenzinger & Weick, 1931)
- Frise (Noyes & Weick, 1932)
- Floating tip (Harris & Weick, 1932)
- Slot lip (Shortal & Weick, 1935)
- Split and upper surface (Wenzinger & Weick, 1934)
- Spoiler (Shortal & Weick, 1932)
- Various combinations of the above types (Toll, 1946),

Plain flap type ailerons, as shown in Figure 2.1 are the most common aileron type used in the research of lateral control performance. This can be seen through reference to the Summary of Lateral-Control Research (Toll, 1946). Typically plain flap type ailerons would have a chord ratio of between 10% and 40% to that of the wing. Aileron span to wing semi-span ratios of 60% to 30% were used with the longer span ailerons having a shorter chord and vice versa. Wenzinger (1931) considered a standard aileron size to be 25% of the wing chord and 40% of the semi-span. These dimensions are common in previous research into aileron performance. Rogallo tested an aileron with a chord 20% that of the wing chord and a span 37% that of the wing semi-span (1941). As the current test data would be compared to the data obtained from

Rogallo's work, for reasons to be discussed further on, similar aileron dimensions would be implemented for the current tests.

One reason for the popularity of the plain flap type is that aerodynamic theory can be successfully applied to the calculation of the rolling and yawing moments of plain ailerons (Jones & Weick, 1937). This makes it easier to validate data obtained from tests and predict loads to be encountered. The rolling and hinge moment trends are also approximately linear functions of the aileron deflection for a plain aileron. Plain ailerons also have the advantage of being easier to manufacture than the more complex shapes such as Frise ailerons.

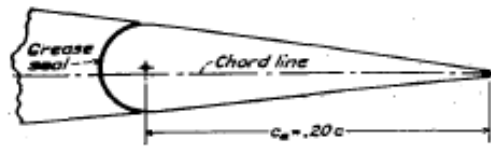


Figure 2.1: Plain Flap Type Aileron indicating definition of aileron chord used in calculations (Rogallo & Purser, 1941)

The common alternative for plain ailerons is the Frise aileron type, as used on the Cessna 172R. This aileron type has the advantage of reduced adverse yaw affects and reduced hinge moments in comparison to plain ailerons. Noyes (1932), however, stated that a plain aileron using differential deflections can be designed to achieve the same adverse yaw advantages as those obtained by Frise ailerons. At high angles of attack the plain ailerons also provide a better level of control than Frise ailerons. The leading edge shape of a Frise aileron is crucial to its performance. An example of the different shapes investigated is shown in Figure 2.2. Relatively small changes in the aileron geometry, such as that in Figure 2.2 (a) resulted in significant changes in the aileron performance. These changes ranged from an introduction of violent shaking of the controls due to a separation of the airflow from the aileron leading edge, to a change in the coefficient of rotation (refer to chapter 2.2.1) of 20%. The higher level of accuracy required in the manufacture of Frise ailerons makes them more difficult to work with in wind tunnel tests.

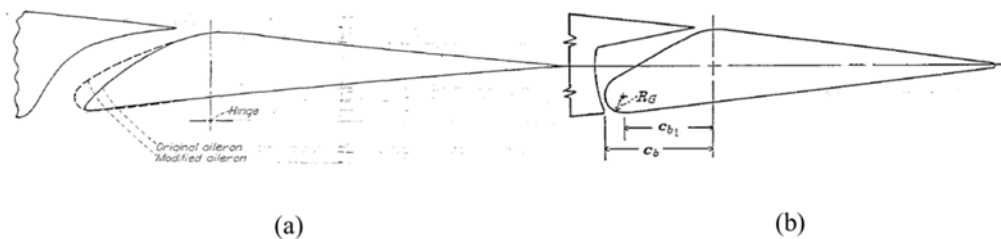


Figure 2.2: Examples of Frise ailerons investigated in previous tests (Toll, 1946)

2.1.1 Blunt Trailing Edges

Throughout the tests, mentioned in the previous chapter, the optimum dimensions of the ailerons were also investigated. The dimensions affected included the trailing edge angle, the

aileron chord, span and taper, the alignment of the aileron hinge lines and the curving of the aileron tips (Jones & Weick, 1937), (Shortal & Weick, 1933). Despite the results from previous research into blunt trailing edges, indicating the application of the noted effects on aspects of aileron performance (Hoerner & Borst, 1985), research into the matter has seen little to no light.

Aerofoils as opposed to ailerons with a blunt trailing edge, however, have been investigated. This included works by Thompson & Whitelaw (1989), Drela (1989), Standish & van Dam (2003), Cooperman et al (2010) and El-Gammal et al (2010) to name a few. Research by Baker (2008) acknowledged that one of the effects of blunt trailing edges was the decreased sensitivity to premature boundary layer transition due to a reduced foil adverse pressure gradient. The reduced pressure gradient was also noted as being responsible for an increase in the lift curve slope as well as increased maximum lift coefficient. This effect can be seen in Figure 2.3.

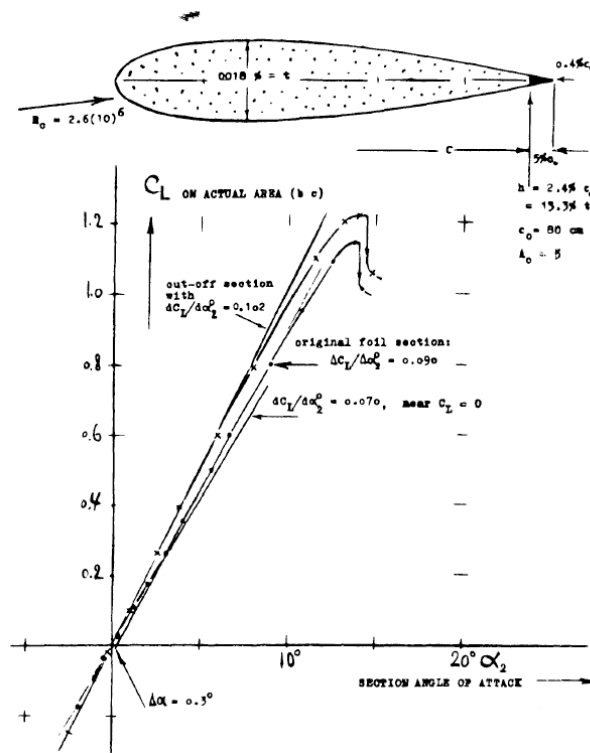


Figure 2.3: Lift of an 0018 airfoil with and without a blunt trailing edge, produced by cutting off the trailing edge (Hoerner & Borst, 1985)

Blunt trailing edges have likely been avoided in the past because of the drag penalty. An example of this effect is shown in Figure 2.4. The increased drag is caused by the blunt edge creating a steady or periodic low pressure flow in the near wake of the aerofoil (Baker, et al., 2008). The reduction of the drag penalty has been investigated, with research by Dam and Kahn (2008) on trailing edge modifications to reduce this. These include splitter plates, trailing edge serrations, base cavities and wedges.

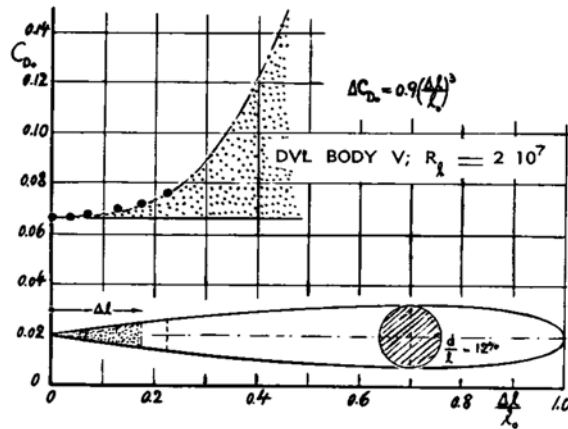


Figure 2.4: Change in drag coefficient of a streamline body brought on by removal of bodies trailing edge (Hoerner, 1965)

Research into blunt trailing edges is typically focused on applications for turbine or propeller blades. These aerofoil profiles typically feature high thickness to chord (t/c) ratios, of 25% or higher (Standish & van Dam, 2003). An example of such a profile is shown in Figure 2.5. Some research, however, has been performed on the application of blunt trailing edges on thinner aerofoils. Smith and Schaefer (1950), for example, investigated blunt trailing edges on the NACA 0012 with similar results as those obtained for the aerofoils with higher t/c values.

Typically the previous research used blunt trailing edges that were the result of the truncation of the wing trailing edge rather than the increase in thickness. More recent studies such as that by Baker et al (2008) and van Dam (2008) have investigated the effect of increasing the trailing edge thickness of the aerofoil symmetrically about the chord line while maintaining the aerofoil t/c ratio. Results of this research indicated similar results as those from the trailing edge truncation, with higher resultant maximum lift coefficients but corresponding higher drag values when compared to conventional trailing edge thicknesses. Considering the C_L/C_D ratio of the wing, however, it was seen that for trailing edge truncation there was no advantage to the C_L/C_D . It was only for a thickening of the trailing edge and maintaining of the wing t/c ratio, that a small advantage could be found (Hoener, 1950). This improvement was noted for a thickness ratio of 0.5% of the wing chord. The application of blunt trailing edges, therefore, needs to be carefully considered as to whether the benefit of increased lift is higher than the penalty of an increase in drag.

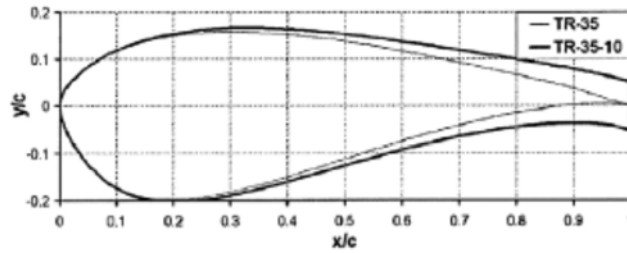


Figure 2.5: Typical aerofoil profile used when investigating thickened trailing edges (van Dam & Kahn, 2008)

Apart from thickened trailing edges, the effect brought on by blunt trailing edges have also been achieved through the use of T-strips and Gurney Flaps. Examples of each are shown below in Figure 2.6. T-strips and Gurney Flaps both result in an increase in the slope of the lift curve and an increase in the maximum lift coefficient (Cavanaugh, et al., 2007). This is similar to the effect of blunt edging brought on by the thickening of the aerofoil trailing edge, as mentioned previously. A rearward shift in the aerodynamic centre of the aerofoil was also noticed for both T-strips and Gurney flaps. Gurney flaps have the added effect of a negative shift in the zero-lift angle of attack and an increased nose-down pitching moment. This shift of the zero-lift angle of attack is expected as the Gurney flap increases the effective camber of the aerofoil. Both T-strips and Gurney flaps resulted in an increase in the drag that was non-linear with device height.

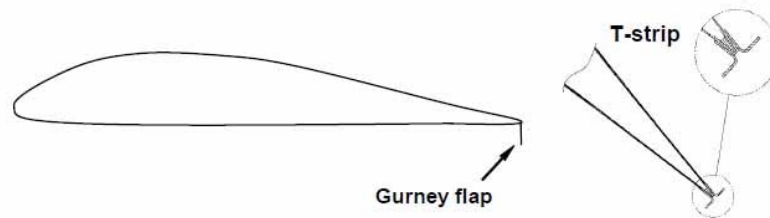


Figure 2.6: Example of Gurney Flap and Trailing Edge T-Strip (Cavanaugh, et al., 2007)

A variation of the principle behind blunt trailing edges is the divergent trailing edge, illustrated in Figure 2.7. Results offered by this type of trailing edge indicate a similar performance to blunt trailing edges with a steeper lift curve. The divergent trailing edge does, however, exhibit a decrease shock-induced drag compared to blunt trailing edges at transonic speeds. This explains why research into divergent trailing edges typically focuses on their application on supercritical aerofoils travelling at transonic speeds (Lotz & Thompson, 1996).



Figure 2.7: Example of Divergent Trailing Edge (Kroo, 2004)

For the current investigation into blunt trailing edges for ailerons to be used on general aviation aircraft, the following points were noted:

- The testing of a divergent trailing edge was of little value due its advantages only in the transonic flight envelope, outside of the typical flight envelope of general aviation aircraft.
- A blunt trailing edge created by the symmetrical thickening of the trailing edge was seen as a superior method as opposed to the truncation of the trailing edge.
- Gurney Flaps and T-Strips provide similar results as that of a conventional blunt trailing edge, as shown in Figure 2.4.

Gurney Flaps and T-Strips typically still require the use of a sharp trailing edge of the aerofoil to be used. A further application of blunt trailing edges on ailerons was to reduce the tolerances to which the trailing edges are typically manufactured. It was thus decided that for the current investigation into blunt trailing edges on ailerons the use of a conventional blunt trailing edge, brought on by the symmetrical thickening of the trailing edge, would be made.

2.1.2 Data Accuracy

In order to get an understanding of the sort of accuracy and resolution in the data, obtained in previous tests, the results and techniques from these experiments were compiled together. The earlier research, done in the 1930's and 40's, was the primary focus of this search. This was because, as mentioned previously, research conducted thereafter shifted focus away from the low speed, unswept wing cases that were seen as the primary application of this research.

Of this earlier research the techniques employed in the investigation into ordinary ailerons on rectangular wings (Wenzinger & Weick, 1931) formed the backbone of the remaining investigations. Papers by Rogallo (1941), Noyes (1932) and Wenzinger (1932), to name a few, all maintained the same or similar levels of accuracy. These were as follows:

- Lift was measured with a precision of $\pm 1\%$.
- The drag was measured with a precision of $\pm 3\%$.
- Rolling, yawing and hinge moment coefficients were similarly precise to within $\pm 3\%$.
- The angle of attack was measured with a precision of $\pm 0.1^\circ$ and the angle of yaw was precise to within $\pm 0.2^\circ$. Although not strictly stated it was assumed that the aileron deflection angle was similarly accurate.

2.1.3 Testing Methodology

Reviewing the previous research it was seen that, in general, aileron deflection increments of 10° between each test point were used. These were used for the majority of the research in aileron performance such as the works by Wenzinger (1931), (1932). Research by Rogallo (1941) and Sears (1942) investigating the effects of modifications to pre-existing ailerons was, however, seen to use 5° deflection changes. It is reasoned that the smaller deflections were used so as to allow for a greater resolution of the effects of the modifications made. It was thus

assumed that 10° deflection changes would be suitable for the testing of a different aileron type, such as a split flap type aileron compared to plain flap type. 5° increments were, however, more desirable when investigating modifications to an aileron, such as the effect of different trailing edge thicknesses.

The aileron deflection range over which previous tests were conducted was typically of the order of $\pm 25^\circ$ as used by Rogallo (1941). Deflections as high as 80° were tested, however such high deflections were rare and only typically used for the investigation of a new aileron type (Wenzinger & Weick, 1931).

The increments in angle of attack, tested previously, are not as consistent as the aileron deflection increments. In general only one or two readings would be made in the lower angle of attack range of 0° to 10° . As stall was approached the increments in angle of attack decreased to a change of around 3° to 5° . Research undertaken by Rogallo (1941) focused on only two angles of attack, one low and one high. Others, such as that by Sears (1942), performed tests at 2° increments for the full angle of attack range from 0° to 16° . The latter method is seen as unnecessary; the data from these tests showing the rolling and hinge moments to follow a linear trend for the lower angles of attack.

The angle of attack range for which ailerons were tested were typically between 0° and 20° . Negative angles of attack would only be investigated when cambered aerofoils were used. As with the aileron deflections, angles of attack higher than 20° were tested; some tests going as high as 60° (Wenzinger & Weick, 1931).

It was reasoned that testing at extreme aileron deflections and angles of attack would be unnecessary. General aviation aircraft typically do not operate outside of the typical ranges stipulated here. This is largely due to the separation of the airflow from the surface of the wing and aileron. For the case of stalls and spins it is commonly accepted practice that the ailerons should not be deflected during either a stall or spin recovery. Typically the deflection of an aileron during a stall can lead to the introduction of a spin and if already in a spin, an increased level of spin. The application of aileron research conducted at these high angles of attack and deflection is therefore very limited.

2.2 Aileron Performance Characterization

The investigation of aileron performance in the past has focused on the following factors: rolling performance, adverse yaw, control loads, lags in response and control free stability. Any further research into aileron performance would need to focus on one or more of these factors in order for any sort of meaningful comparison to be made. Lags in response and control free stability refer to dynamic cases and are beyond the scope of this research.

2.2.1 Rolling Performance

The coefficient of rotation has been shown, by analytical studies and the investigation by Gilrith and Turner (1941), to be the most convenient method for specifying the rolling performance of

an aircraft. The equation used is given below. For a maximum roll rate likely to occur in flight in gusty conditions this coefficient was determined to have a value of 0.05 (Wenzinger & Weick, 1931).

$$\frac{pb}{2V} = \frac{C_l'}{C_{l_p}} \quad 2.1$$

Where: p angular velocity of roll, radians/sec; b span of the wing, m; V true airspeed, m/s; C_l' rolling-moment coefficient; C_{l_p} damping coefficient.

Typically, however, most research presents its results for the rolling moment coefficient only. It is possible to calculate the helix angle and the calculated damping coefficient using this data, the method of which is specified by Toll (1946). The rolling moment coefficient is calculated using the following equation:

$$C_l' = \frac{L'}{qSb} \quad 2.2$$

Where: L' rolling moment, N.m; q dynamic pressure of the airstream ($\frac{1}{2}\rho V^2$), kg/m²; S wind tunnel test model plan form area, m

Depending on the research done the rolling moment coefficients may be different as this is due to the way in which the rolling moment is measured and calculated. For example the use of rotation tests will allow for the rolling moment due to the wings rolling to be measured. Rogallo (1941) calculated the rolling moments as the difference in load experienced when the aileron was at zero deflection and when it was deflected. This method is the one chosen for the purposes of this research, with the rolling moment in equation 2.2 being calculated in this manner. The use of this method was understood to allow for a simpler external balance to be used during testing. The primary focus of the research was the measurement of the aileron hinge moments and not the measurement of the rolling and yawing moments. By using a simpler external balance, for the purposes of measuring the rolling and yawing moments, it minimized the chances of faulty data sets and made testing easier to manage.

2.2.2 Adverse Yaw

Adverse yaw effects brought on by aileron deflections is commonly investigated when trying to ascertain the nature of the lateral control device. Adverse yaw is caused by the combined effects of an inherent yawing moment brought on by a rolling wing and a yawing moment caused by the operation of the lateral control device. For this reason care should be taken when comparing this aerodynamic coefficient between research papers as, with the rolling moment coefficient, the yawing moment coefficient will depend on the manner in which the moment is measured and calculated.

The equation used for calculating the yawing moment coefficient was as follows

$$C_n' = \frac{N'}{qSb} \quad 2.3$$

Where: N' yawing moment, N.m.

For the purposes of this research the same technique as used by Rogallo (1941), and as used for the rolling moments, was used in the measurement and calculation of the yawing moments. The reasons for which were explained in the previous chapter. In this way the yawing moment used in the above equation was the difference between the moment at zero aileron deflection and with the aileron deflected.

2.2.3 Control Loads

The control loads specified for lateral control devices in previous research is either presented as stick loads that a pilot would experience during flight or the hinge moment coefficient. Stick loads are typically only given for research conducted during flight tests and are of little use in comparisons unless for aircraft of a similar type or if the control system specifications are known. The most useful way in which aileron loads are specified, therefore, is through the hinge moment coefficient, calculated using the equation below:

$$C_{Ha} = \frac{H_a}{qc_a^2 b_a} \quad 2.4$$

Where: H_a hinge moment of the aileron, N.m; c_a aileron chord, m; b_a is the aileron span in, m

The hinge moment used here is the absolute value measured and not, like the rolling and yawing moments, a difference in the load from a zero deflection and the measured deflection. It should be noted however that the aileron chord used in the above equation is measured from the aileron hinge line to its trailing edge, as shown in Figure 2.1, and not from the aileron leading edge. This is a typical convention used in the analysis of aileron performance characteristics. A result of this is that the nose shape of the aileron is not taken into account. Toll (1946), however, provided correction factors that can be applied to the aileron hinge moments to compensate for different aileron nose shapes.

2.3 Low Reynolds Number Testing

Due to limitations placed on the current research by the available facilities, tests are conducted at Reynolds Numbers of around 300 000. Most of the research conducted previously on aileron performance was conducted at Reynolds numbers of one million or higher. This difference in Reynolds numbers means that the nature of the airflow over the aerofoils will be different. The significance of this will be discussed below.

Jacobs (1937) performed research on the effect of low Reynolds numbers on common aerofoil characteristics. The discussion into the effect, as laid out by Jacobs, deals mostly with airflow separation. At high angles of attack the energy in the airflow ultimately becomes too low leading to the separation of the airflow over the aerofoil upper surface, this separation affecting the maximum lift of the wing; the lower the Reynolds number, the lower the maximum lift

possible. This can be seen in the results shown in Figure 2.8 for the effect of Reynolds number on the maximum lift coefficient (a larger copy of this image is given in Figure A.3). The trend of the drag coefficient, at high angles of attack, also changes as the Reynolds number is decreased; the drag being higher for a lower Reynolds number at a given angle of attack.

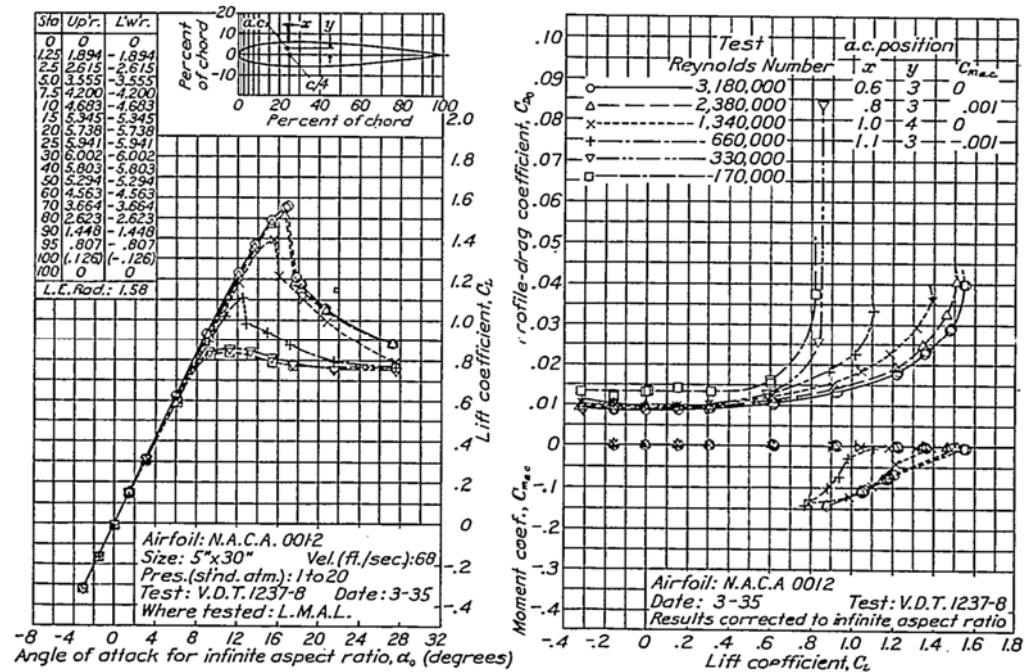


Figure 2.8: Aerofoil data for NACA 0012 conducted for a range of Reynolds numbers between 170 000 and 3 180 000 (Jacobs & Sherman, 1937).

Furthermore Jacobs found that while operating in the Reynolds number range, of 400 000 to 800 000, two or more drag values were possible (Jacobs & Sherman, 1937). This dual solution would have either a high or low drag value occurring if the system was disturbed. Operating in this range of Reynolds numbers was therefore not advisable. At the low Reynolds numbers achievable in the current wind tunnel facilities it would thus be preferable to operate below this range. The maximum lift coefficients obtained from tests conducted at 300 000 and 1000 000 would therefore be very different at high angles of attack. Likewise the drag coefficients, at high angles of attack would be different as well.

Lower Reynolds numbers were been noted by Jacobs (1937) to have an effect on the wing at low angles of attack. Figure 2.9 shows an aerofoil at a low angle of attack for a low Reynolds number (a) and a higher Reynolds number (b). The Figures presented by Jacobs (shown in Figure A.4) are similar to those shown in Figure 2.9, however the images are of a low quality which is why they are not presented here. The observations by Jacobs on his flow visualization are assumed to still be relevant. It was noted by Jacobs that separation of the laminar boundary layer would always be present at a point near the nose if the Reynolds number is not sufficiently high enough to make the flow turbulent at that point. As the Reynolds number is increased a transition region occurs along the separated boundary layer, where the laminar flow slowly

transitions to the fully developed turbulent layer. The transition region moves forward towards to the leading edge, as the Reynolds number is increased. The resulting turbulence thickens the boundary layer between the dead air, beneath the separated airflow, and the overrunning flow. The thickening of the boundary layer ultimately leads to the separated airflow being reattached. While not clearly stated by Jacobs (1937), it was assumed that the low Reynolds numbers referred to are of the order of 50 000. This assumption was based on the lowest Reynolds number for which the data was presented; this value, as seen in Figure 2.8, being 170 000. At low angles of attack, in Figure 2.8, there is a lack of any noticeable difference in trends or magnitudes of the aerodynamic coefficients. It was therefore assumed that the effect of the low Reynolds number, discussed here and observed by Jacobs (1937), is not prevalent at Reynolds numbers above 170 000 at low angles of attack. In order to ensure that any meaningful comparisons could be made between the previous research, conducted at higher Reynolds numbers, and the current research it would be necessary to operate at a Reynolds number above 170 000 in order to ensure that the laminar boundary layer did not separate.

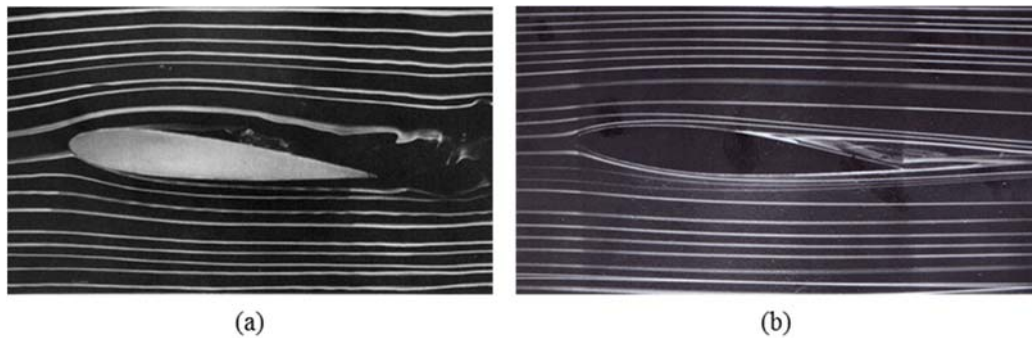


Figure 2.9: Separation occurring on an airfoil at a low angle of attack, at low a Reynolds number (a) and an increased Reynolds number (b) (van Dyke, 2005)

Operating at a Reynolds number of 300 000 was therefore seen as the optimal value. In this way the test conditions were well below the dual solutions cases occurring above 400 000 and high enough to ensure the separation of the laminar boundary layer did not occur. A Reynolds number of 300 000 was also within the capabilities of the current wind tunnel testing facilities being used.

2.4 Hinge Moment Measurement Techniques

Previous methods used in the measurement of aileron hinge moments were investigated. It was seen that the methods and techniques used in the past for the measurement of hinge moments were varied. Most the techniques used for wind tunnel testing by NACA were of a similar type as shown below in Figure 2.10.

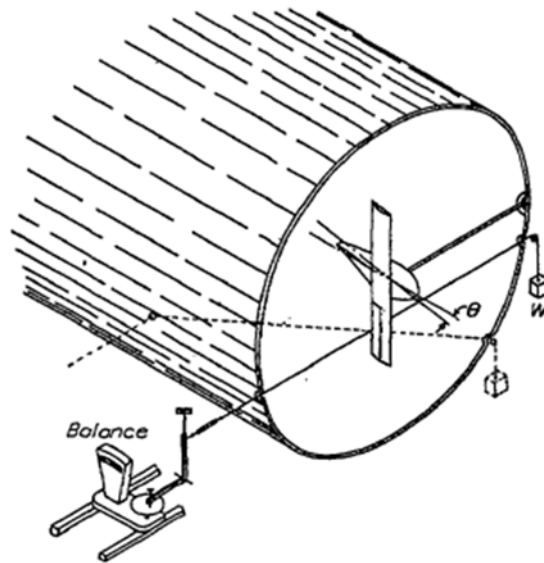


Figure 2.10: Previously used Hinge Moment Measurement Arrangement (Monish, 1930)

Problems with this technique are that there are intrusions into the airflow that may cause adverse effects on the results. Although it was stated by Monish that these affects were negligible it was still viewed as unsatisfactory as to need such intrusions. Another measurement type, shown in Figure 2.11, presents slightly less of an intrusion into the airflow.

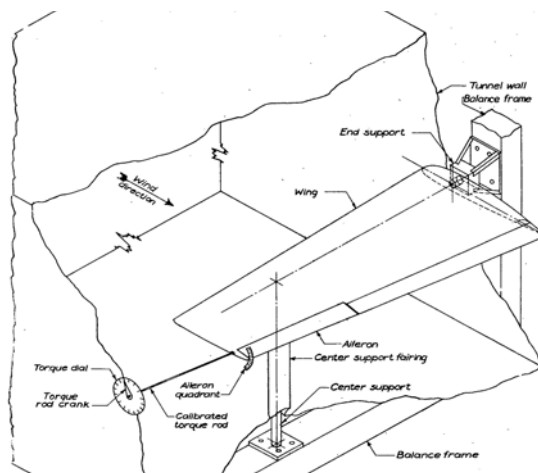


Figure 2.11: Test setup as used by Rogallo (Rogallo & Lowry, 1942)

None of the above mentioned measurement techniques were seen as satisfactory mainly due to the intrusions into the airflow. With tests having to be conducted at the lower Reynolds numbers, as previously mentioned, intrusions in the airflow may have increased the difficulty in the measurement of yawing moment values. These intrusions were largely necessary due to the space limitations in the wind tunnel model. This meant that a hinge moment measurement system mounted internal of the wing structure was only employed on full scale flight test models, as shown below, used on the P-40 (Goranson, 1946). In this method the measurement balance is connected in line with the actuation system for the aileron and any load introduced

into the aileron from the airflow would be read by the strain gages on the deflection member. While this method shows promise it would need to be modified to fit inside and be implemented inside a smaller wind tunnel test model.

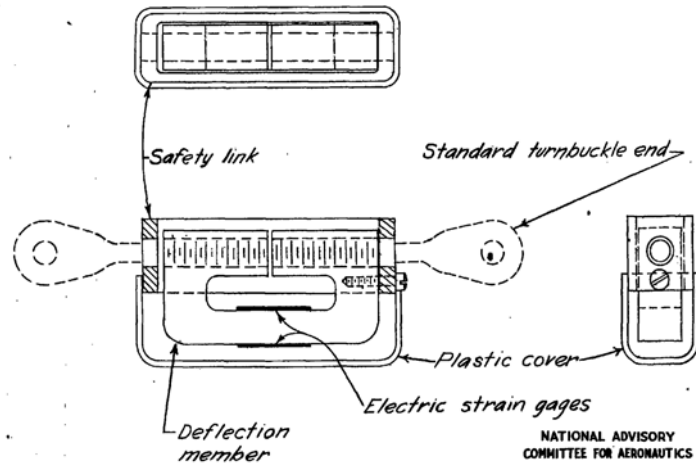


Figure 2.12: Cable-tension recorder as employed by Goranson (1946) during flight tests.

2.5 Test Model Configurations

From various reports written for the National Advisory Committee for Aeronautics it was seen that when testing the performance of an aileron a half span model was typically used. R. Heald (1933), stated that when studying the performance of an aileron it is convenient to either make use of a half span model with a reflecting plane or a complete span with a single aileron, either on the port or starboard side. It was reasoned that the convenience of a half span model stems from the fact that only half the wing need fit inside the wind tunnel thereby allowing for the model to have a larger aspect ratio and higher Reynolds numbers can thus be achieved. By testing only one aileron on a full span model it removes the requirement of having to ensure precision deflections of the two control surfaces. It also makes the construction and operation of such a model simpler.

3 METHOD

The three objectives of this research were for the design and testing of a balance capable of accurately measuring the hinge moment of an aileron during testing, the validation of the results obtained from the hinge moment balance design and investigation into the effects of differing aileron trailing edge thicknesses on the aileron hinge moment. The tests would be conducted on a static system with no investigation into the dynamic loads. In order to ensure these objectives were met and a comprehensive test regime was followed, a test matrix was drawn up. This ensured that all aspects to be covered would be tested.

The use of CFD simulations was seen as not being appropriate for this research. This was based on the added uncertainties associated with the use of CFD results and difficulties associated in measuring the resulting hinge moments (Soinne, 2000). For these reasons no CFD simulations were undertaken.

3.1 Test Matrix

The following factors would be varied during testing:

- Angle of Attack (0° ; 5° ; 10° ; 12.5° ; 15° ; 17.5° ; 20°)
- Aileron deflection (-25° to $+25^\circ$ in increments of 5°)
- Aileron trailing edge thickness (between 0.25% and 1.5% of wing chord)

For each test the rolling, yawing and hinge moments produced by the aileron would be measured and recorded.

Previous research, as mentioned in chapter 2.1.2, used 5° increments in angle of attack when testing aileron performance. Initial tests showed that these increment levels proved to be inadequate in the stalling region of between 10° and 20° angle of attack. It was therefore decided to make use of 2.5° increments in this angle of attack range. 5° increments would still be used for the lower angles of attack as this was seen as adequate for realization of any occurrences or areas of interest.

The average aileron deflection increment used in previous research was approximately 5° . Smaller increments were desired to allow for a greater resolution of the results and data trends. It was realised that this would not always be possible, especially at high aileron deflections; increments as small as 2° would be attempted during testing nevertheless.

Aileron trailing edge thickness would be varied in order to determine what effect the differing thicknesses had on the aerodynamic coefficients of the wing. Four distinct trailing edge thicknesses would be focused on. The range of thicknesses tested would encompass the critical 0.5% h/c noted by Hoerner (1985). For each case a set aileron test piece would be installed, the angle of attack set and the deflections run through.

Each test would consist of the zero load signals being recorded before the tunnel was activated. Data would then be recorded with the tunnel at the test speed. The wind tunnel would then be turned off and the test model set for the next configuration. At each point the balance forces, air temperature, pressure and humidity, air speed inside the tunnel and measured aileron deflection would be recorded. A separate file was recorded for each test case, a naming convention using the speed setting and deflection being used to allow for easy reading in of the data later as well as for easy reference.

In light of the effect of the lower Reynolds numbers on the airflow over the wing and aileron, discussed in chapter 2.3, it was decided to carry out flow visualization of certain test conditions. These test conditions would be chosen based on an investigation of the test results.

The precautions followed during testing can be found in Appendix H.

3.2 Test Equipment Requirements

The following points contain the list of requirements for the test equipment and facilities. These were created to ensure that the above test matrix could be complied with and a sufficient level of accuracy could be obtained. The values given were based on the findings and conclusions made throughout chapter 2.

Requirements

- Tests should be conducted at a Reynolds number of 300 000.
- A common aerofoil type should be used.
- A plain flap type aileron should be used.
- The aileron chord should be ~20% of the wing chord
- The aileron span should be ~40% of the wing semi-span
- A maximum aileron deflection of $\pm 25^\circ$ should be possible
- Have a minimum achievable aileron deflection increment of 5°
- The measured aileron deflection should be measured with a precision of $\pm 0.1^\circ$
- The angle of attack should be measured with a precision $\pm 0.1^\circ$
- Rolling, yawing and hinge moment coefficients should be measured with a precision of $\pm 3\%$

4 FACILITIES AND EQUIPMENT

The following chapters, summarised here, detail the facilities and equipment used during experimentation. Wind tunnel tests were the main focus of this research. The 1.49m x 1.49m draw down wind tunnel, in the North West Engineering building of the University of the Witwatersrand, was selected for this purpose. The wind tunnel allowed for air speeds of 15m/s to be reached during testing.

A rectangular plan form NACA0012, 0.75m semi-span by 0.38m chord, wing was cast and machined from a polyurethane resin. The wing was mounted vertically in the wind tunnel and had an aileron with a 20.6% chord and 40% span. A hinge moment balance was designed and installed inside the wind tunnel model allowing for the actuation of the aileron and measurement of its hinge moment during testing. The hinge moment balance had a resolution of 0.06% of the maximum applied loading. Aileron deflection was measured through the use of a small voltage potentiometer that allowed for an uncertainty of $\pm 0.1^\circ$ in the measured deflection.

For the purposes of measuring the wings aerodynamic loads a 3 axis external balance was installed underneath the wind tunnel. This balance was used to measure the rolling and yawing moments produced by the wing during tests. The rolling and yawing moments would be measured with a resolution of 0.13% and 0.17% of the applied aerodynamic loads respectively. Rolling, yawing and hinge moment loads were all measured through the use of off the shelf loadcells.

Loadcell signals and the measured voltage across the potentiometer was recorded digitally through the use of a 16 bit NI USB6211 DAQ and Labview software. High levels of signal noise were encountered in initial experiments and this was addressed as best possible through the use of filters and averaging functions built into the recording software. The sensors were powered by a custom built power supply utilising six 12V lead acid batteries and voltage regulators ensuring isolation from the mains supply and associated signal noise issues. The power supply allowed for a constant supply voltage for up to 20 hours of continuous testing.

Air Temperature, ambient air pressure, airflow dynamic pressure and humidity were all measured and recorded during testing. The temperature was measured by a k-type thermocouple plugged into a 20 bit USB-TC01 Temperature DAQ allowing for a resolution of $\pm 0.6^\circ\text{C}$. The pressure manometer, used for the measurement of ambient air pressure, had a precision of $\pm 1\%$. The velocity was measured through the use of a Digital pocket manometer and pitot tube with a precision of 3%. A weather station measured the air humidity with a precision of 1%.

4.1 Wind tunnel

The drawdown wind tunnel is fitted with a 6 blade Howden CT6 10ft diameter fan. At maximum power the wind tunnel is capable of producing airspeeds of approximately 18m/s inside the wind tunnel's 1.49m x 1.49m test section. The high vibration that occurs at the higher speed range means that the tunnel is rarely run at this speed. This vibration is likely due to the tunnels' diffuser being incorrectly sized for the setup in place. As a result, the highest safe operating speed is set at approximately 15m/s. The wind tunnel cross sectional profile is shown in Figure 4.1.

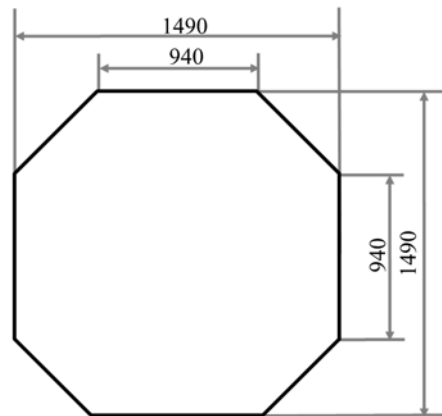


Figure 4.1 Wind tunnel cross section and internal dimensions

Coordinate system

A right-hand wind axis coordinate system, fixed with respect to the tunnel, was used for the external balance load measurement aspect of the testing. This is represented in Figure 4.2 below, the x-axis aligned with the tunnel flow direction as indicated. The right hand model fixed axis was employed when measuring the hinge moment from the lateral control device. These coordinate systems were used throughout the testing.

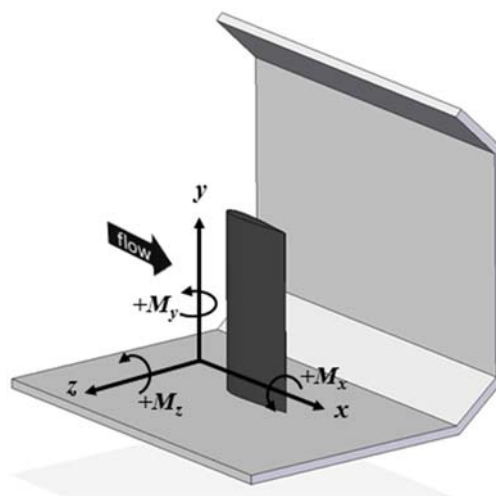


Figure 4.2: External Balance Axis System

4.2 External Balance

Design

The external balance was capable of measuring the rolling and yawing moments of the wind tunnel model. By only having to consider these two aerodynamic moments, the design of the balance was largely simplified and allowed for the use of existing components. The primary focus of the research was the investigation of aileron hinge moments and wing loads were seen as being of secondary interest.

As mentioned previously, the roll and yaw would be calculated using the same methodology as employed by Rogallo and Purser (1941). In this method the rolling moment is calculated from the difference in the measured load with the aileron at zero deflection and in the reaction loads with the aileron deflected. Using this method and expected tunnel conditions the maximum loads that each of the loadcells were expected to experience could be calculated. This allowed for external balance dimensions to be specified such that there would sufficient resolution of the signals during a test but also such that they would not be overloaded. Using the data obtained from previous tests and the final dimensions of the balance, the three loadcells were expected to experience the following approximate loads during testing:

Loadcell	Total Load [N]	Load due to Moments [N]
Rolling Moment	~60	~20
Yawing Moment	~30	~6

The total load would be comprised of both the aerodynamic forces and moments. These were calculated to ensure that the loadcells were not overloaded during testing. The load, due to the rolling and yawing moments, were calculated to ensure the measurement system would have sufficient sensitivity to resolve the measured moments. These were the maximum expected rolling and yawing moments based off Rogallo's data (Rogallo & Purser, 1941); being ~1.0N.m and ~0.3N.m respectively.

The loadcells and balance arm were mounted inside a pre-existing cage, shown in Figure 4.3, mounted to the bottom of the wind tunnel flooring. The cage acted as a rigid mounting platform for various components that were to be installed, a high level of framework and the use of 25mm square hollow steel tube was seen as being satisfactorily capable of having the cage remain rigid during testing conditions. The cage walls were fitted with mounting plates that allowed for a relatively high level of customization in the configurations and arrangement of the loadcells. This allowed the position and configuration of the loadcells to be fine-tuned for optimal results as well as allowing for the implementation of future modifications.

Zemic L6D Loadcells were used for the measurement of the three moments. The rolling moment was measured using a 10kg model while a 6kg model was used for the yaw

measurement. The 6kg model allowed for a greater load resolution, this being seen as required for the measurement of the yaw load. The loadcell capacities also ensured a 1.5 safety factor for the loadcells to account for any extra load that may be applied. Detailed specifications of the loadcells can be found in Appendix C and are summarised below. The excitation voltage is that used during tests.

Gage Factor (G)	2.0 ± 0.2
Gage Resistance (Ω)	350 ± 3
Excitation voltage (V_{EX})	$9V \pm 0.1$

The loadcells were rigidly mounted to the balance cage and connected to the balance arm through silver steel rods. These connector rods had rose joints bolted on the ends, one with left hand thread and the other with right hand thread. This allowed the distance between the loadcells and the balance arm and hence alignment of the balance arm, to be easily adjusted.

The balance arm, as labelled in Figure 4.3, was mounted to the base plate of the cage through another rose joint. This rose joint was screwed into the base plate and created an effective 2-axis pin joint, allowing for the free rotation of the balance arm about the rolling and yawing axis. The rose joint had the added advantage of preventing the vertical translation of the balance arm. This was shown through previous testing to create unwanted additional loading and introduced hysteresis.

The use of rose joints minimised the cross coupling of the measured loads by only allowing movement in a particular axis as well as preventing off axis loading being applied to the loadcells. Small movements in the rose joints, for both the loadcell connections and balance arm, were noticed during assembly. These movements could not be completely eliminated but were minimized as far as possible.

Figure 4.3 shows the external balance in its final configuration with Figure 4.4 (a), (b) and (c) showing the top, side and front views respectively. The black arrow in Figure 4.3 indicates the direction of the airstream in the wind tunnel with regards to the balance.

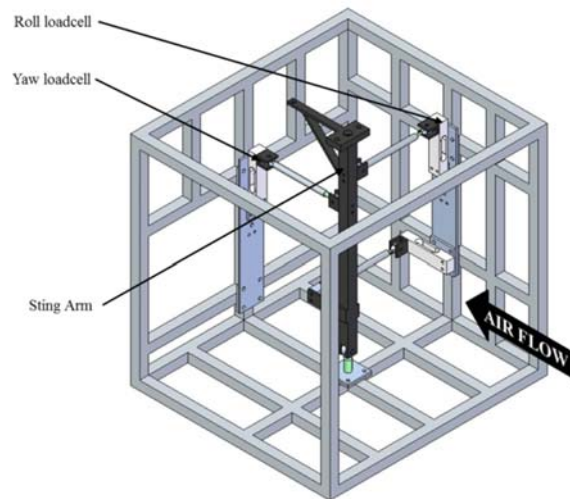


Figure 4.3 External Balance Isometric View

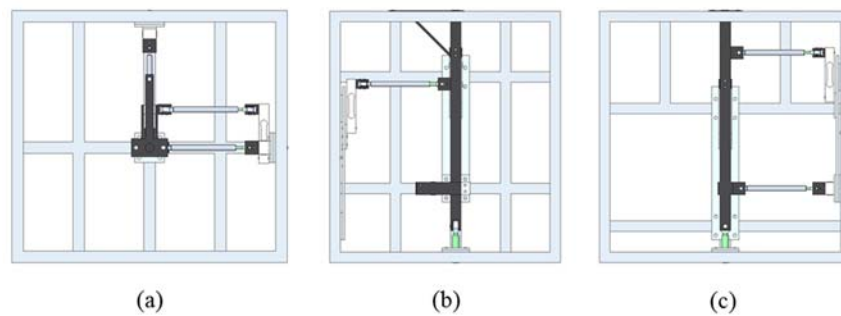


Figure 4.4: External Balance 3 View

Mounted on top of the balance arm was an alignment plate, shown in Figure 4.5. The plate allowed for the wing to be mounted to the balance and aligned to a desired angle of attack. Holes were drilled along the trailing edge of the plate in 2.5° increments about the central leading edge hole. The wing would pivot about the central leading edge hole at its quarter chord point. The trailing edge holes would then be used to align the wing to a desired angle of attack through the use of a removable pin.

Previous tests using 5 degree increments were found to give an inadequate indication of the point at which stall occurred. 2.5° increments were seen as being sufficiently small enough while still being practical for the purposes of testing and manufacturing. In order to ensure the accuracy of the angle increments of the plate, the component was laser cut, the process having a reported tolerance of $\pm 0.02^\circ$. This accuracy was confirmed through measurements made on the finished plate. While a slider in a groove would have provided a theoretically infinite number of angles of attack at which to perform tests this method was shown, in previous tests, to be insufficiently repeatable.

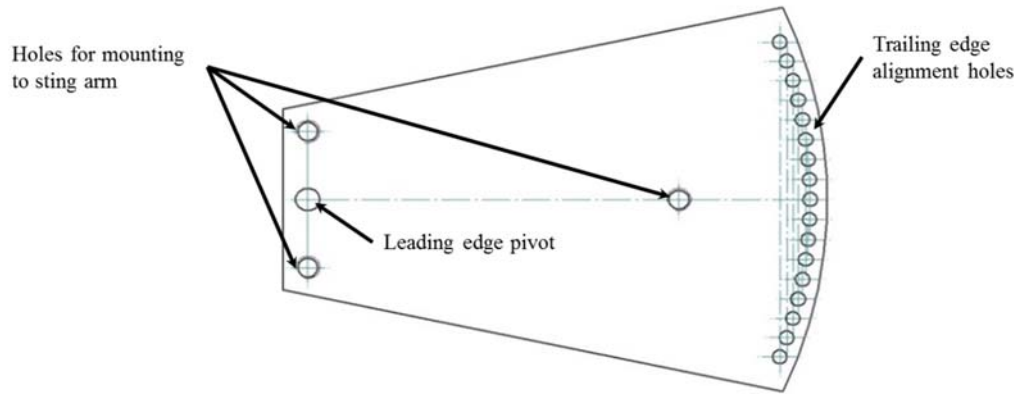


Figure 4.5 Wing Alignment Plate

Installation

The external balance was preassembled before being installed beneath the wind tunnel. This was done to ensure a more accurate alignment of sub components to one another, further preventing the possibility of off axis loading being applied to the loadcells. All components were securely fastened to prevent any vibration or shifting of the components which would have introduced unwanted noise into the system.

Alignment of the rods, connecting the balance arm to the loadcells, as well as the balance arm itself was done through the use of a digital protractor offering a precision of 0.01° . The inclinations of the balance arm was adjusted through the rotation of the connector rods, the opposite direction thread on each end allowing the connector rod length to be increased or decreased as necessary.

3mm plywood board was cut to shape and fit around the wing alignment plate during testing to prevent flow occurring between the board and wall into the wind tunnel through the hole cut for the external balance arm. This cross flow on the wing can induce separation and low cycle oscillating aerodynamic loading of the wing. This would reduce the quality of the measurements taken. A gap of about 5mm was allowed to prevent the plywood board inhibiting the movement of the balance and wing.

4.3 Test Model

4.3.1 Design

Research into the use of casting resins showed that these materials could be made to be lighter than equivalently sized aluminium wings but had the advantage of allowing for internal components to be securely mounted. The design of the hinge moment measurement balance, as discussed in chapter 4.3.4, meant that components such as motors and loadcells would need to be mounted internally. Consequently a Fastcast Polyurethane resin, designated F18 by the manufacturer, was chosen to be used to manufacture the model. Reasons for the choice of F18 were that it exhibits good impact resistance, low shrinkage, and a low viscosity. The casting

resin could also have a filler agent added to the mixture. This adjusted the mechanical properties, such as the strength and weight of the model without affecting the pouring viscosity. Q-CEL 5020 glass micro balloons were used as the filler as this was shown, through a series of test pieces made, to further reduce the model weight without compromising the strength integrity and machinability of the F18.

Based on the test equipment requirements, NACA 0012 wing profile moulds were used. The historical popularity of this profile made it the most appropriate choice. The mould span of 800mm and chord of 400mm was limited by the largest mould that could be machined. An 800mm semi-span wing with an aileron mounted on the outboard end meant that the aileron would be approximately positioned in the middle of the wind tunnel cross section. This meant the aileron would be as far as possible from any wind tunnel wall boundary layers or edge effects.

A Reynolds number of 300 000 was desired for the tests, as set out by the test equipment requirements. With a 400mm wing chord the required wind tunnel speed would need to be approximately 15m/s in order to achieve this Reynolds number. This was within the capability of the current wind tunnel. This meant that both the current wing mould and wind tunnel would be suitable for the current set of tests.

Previous tests had shown the issues that arose with attempting to achieve a zero trailing edge thickness of the aerofoil, namely the brittleness of the trailing edge. For this reason the mould was designed to give the cast model a trailing edge thickness of 1mm.

4.3.2 Manufacture

The F18 casting resin consists of two parts. These were mixed in a 1:1 ratio by mass as recommended by the supplied documentation for the material. The glass micro balloons were measured to an approximate volumetric ratio of 1:2 to the casting resin. No documentation existed for the use of the glass micro balloons as a filler for the F18 and this ratio was determined experimentally. The large difference in densities between the F18 resins and the filler meant that it was easier to measure using a volumetric ratio rather than a mass ratio. The volumetric ratio of 1:2 was found to produce the best results by minimizing weight while maintaining sufficient levels of machinability and durability.

The castings were given 24 hours to set and cure. Internal cut-outs were machined into each wing half for the following purposes:

- Reduce model weight
- Alignment of each half for assembly
- Mounting to external balance
- Mounting of internal components (hinge moment balance, potentiometer and aileron actuator)

Based on limitations imposed during the machining process the final dimensions of the NACA 0012 wing were less than the maximum offered by the mould. The cut-outs and final dimensions are shown in Figure 4.6.

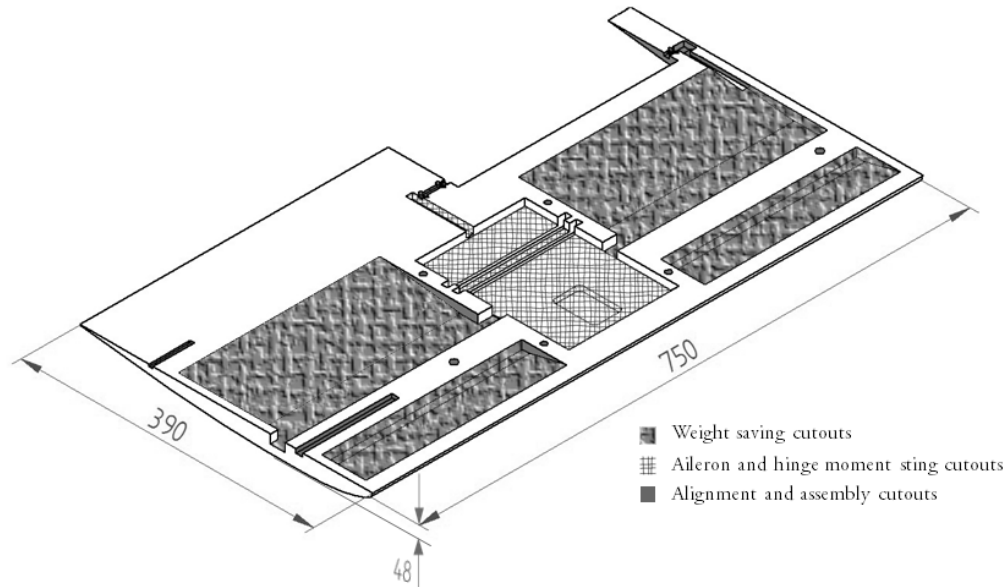


Figure 4.6: Half wing cut-outs

Silicon was used to seal the edges of the model wings together. The silicon doubled as a gluing agent that worked in conjunction with the two main assembly bolts. A small amount of warping along the wing trailing edge was found to have occurred. This resulted in the aileron assembly being able to vibrate in its housing during testing. The solution to this was an M3 bolt, installed near the trailing edge on the root side of the aileron. This eliminated the warp in the wing halves and prevented any unwanted movement of the aileron in its housing

4.3.3 Lateral Control Device

Dimensions

The profile dimensions and shape of the aileron that was tested are given below in Figure 4.7. The aileron had a span of 300mm or 40% of the wing span.

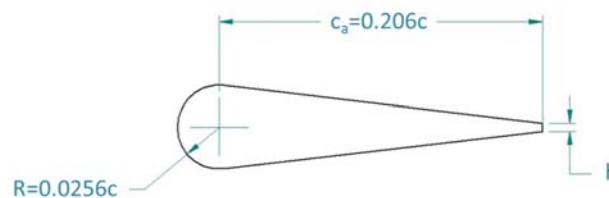


Figure 4.7: Aileron profile to be tested

The profile, shown in Figure 4.7, was chosen as most of the previous research done on lateral control devices made use of this design, especially the research done by Wenzinger and Weick (1931). For those papers that used a different profile there exists research to show the effects of the different shapes. Four different ailerons were to be tested, with the trailing edge thicknesses (dimension h in Figure 4.7) being varied in each. The following trailing edge thicknesses, represented as a percentage of the wing chord c , were tested:

Table 4.1: Aileron Trailing Edge Thicknesses

Aileron Test Piece	Trailing Edge Thickness
Thickness 1	0.39% c
Thickness 2	0.71% c
Thickness 3	0.96% c
Thickness 4	1.22% c

The above listed dimensions of the trailing edge thickness of the test ailerons were found to vary by approximately $0.026\%c$ due to manufacturing flaws. The remaining dimensions, the chord, span and leading edge radius, were kept constant.

Design

The design of the lateral control device was centred around the allowance for a quick and easy change between the various aileron test pieces. The idea was to not have to disassemble the wing between tests to change the aileron out. Disassembly would have meant a recalibration of the hinge moment and deflection measurement system would be required with each aileron change. There would then be no guarantee that the system performed the same way each time and comparisons between the four ailerons would be less reliable.

The final design that was chosen is shown in Figure 4.8. It makes use of a common leading edge rod that is then permanently fitted inside the wing and attached to the load and deflection measurement equipment. The leading edge rod was supported inside the wing on three low friction bearings. The separate ailerons tested fitted onto the leading edge rod via the pre-milled slots. Each aileron consisted of four ribs held together by aluminium plates forming the skin of the ailerons. Each rib had a tapped hole along its length used to attach the ailerons to the leading edge rod.

The use of a rib and skin system allowed for a lower mass of the aileron while still maintaining sufficient rigidity. Solid ailerons were investigated however their mass, regardless of material, was too high; the resulting high inertia of the aileron being seen as undesirable. Aluminium was chosen as the primary material used in the manufacture of the ailerons due to its relatively low density. While lighter materials exist, the structure of the aileron test pieces was easier to manufacture from aluminium.

Petroleum jelly was used to seal the gap between the aileron and wing surfaces. It was noted that the material added no discernible friction to the system and made an effective sealant (Monish, 1930).

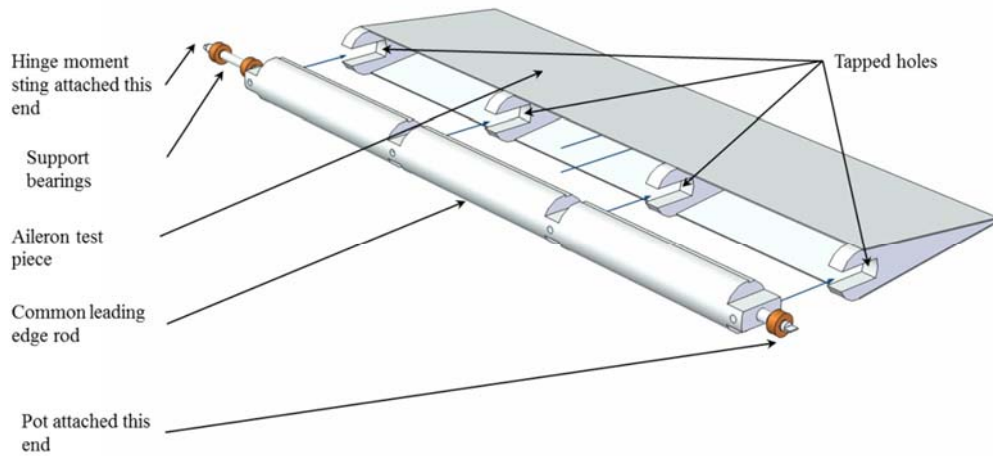


Figure 4.8: Aileron Design

Deflection Measurement

Aileron deflection was measured through the use of a $5k\Omega$ potentiometer (or pot). This was connected to the aileron leading edge rod, shown in Figure 4.8, on the outboard side of the wing. Space limitations at the trailing edge of the wing limited the size of the potentiometer. Despite the small size of the pot used, preliminary tests indicated the system was able to provide the required precision.

The pot was wired in series with a second resistor. The second resistor meant that a zero resistance case was not reached as the pot was adjusted. As the aileron deflected, the attachment from the aileron leading edge rod would rotate the dial on the pot. This adjusted its resistance and hence the voltage potential across the pot. The voltage potential was measured as the aileron deflected, allowing for the aileron deflection to be measured. The disadvantage of wiring the pot in series was that the measured voltage change would be non-linear as the pot angle was adjusted. The use of a Wheatstone bridge would have minimized the non-linearity. The aileron was, however, only operating over a small deflection range. Over this range it was found to be possible to optimize the simple series circuit to produce a relatively linear response over the deflection range tested. It was therefore seen as unnecessary to wire the potentiometer in a Wheatstone bridge circuit.

Over the desired full aileron deflection range of $\pm 30^\circ$ the voltage across the potentiometer would range from 2.3V to 3.7V. An aileron deflection of 5° would result in a change of approximately 0.1V. The significance of this is discussed further in chapter 6.2.2.

4.3.4 Hinge Moment Balance

The hinge moment balance, shown in Figure 4.9, was used for the measurement of the hinge moment produced by the aileron during testing and deflection of the aileron. The balance was mounted inside the region of the wing as indicated in Figure 4.6.

Load measurement was made through the use of a 5kg S-Type full bridge loadcell. The S-Type was chosen over alternate options as it allowed for the motor, loadcell and actuation arm to be placed in line with one another. This minimized the space taken up by the system inside the wing as well as the chance of eccentric loading being applied to the loadcell.

The balance was actuated through the use of a QJT-25JS-B 6V geared DC motor, mounted rigidly inside the wing. A custom threaded rod, connected to the motor, was screwed into one of the loadcell's tapped mounting points. As the motor rotates the threaded rod, the loadcell can be translated back and forth. On the other end of the loadcell was another custom made connection, acting as an actuation rod, linking the loadcell to the aileron leading edge rod. As the loadcell was then translated the actuation rod would push or pull on the connection to the aileron leading edge rod; this in turn deflecting the aileron. The connection between the aileron leading edge rod and actuation arm had a moment arm of 3.5mm.

Any load then applied to the aileron would translate into the actuation rod and thus into the loadcell. The measured load could then be calibrated to calculate the applied hinge moment load.

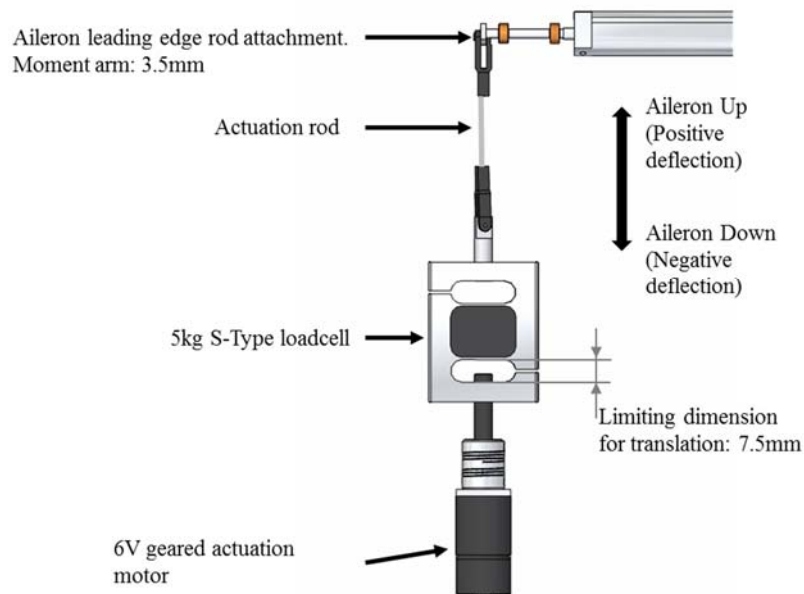


Figure 4.9: Internal Hinge Moment Balance Configuration

A moment arm of 3.5mm was chosen so as to magnify the hinge moment loads produced by the aileron during testing. The distance was optimized such that the loads introduced into the system, during testing would be easily picked up by the loadcell. These loads were based off the use of hinge moment data obtained from Rogallo (1941). Using his data, the expected hinge moment loads that the aileron would experience were calculated to apply a maximum load of approximately 15N on the loadcell.

The actuation motor was set to rotate at approximately 5RPM, depending on the loading it was seeing. This translated to an approximate aileron deflection of 2° every second. This allowed for a relatively high level of control of the aileron position when attaining a desired deflection.

In order to prevent unwanted movement of the loadcell inside the cavity of the wind tunnel model, lubricated rollers and guide arms were used. These held the loadcell in position, preventing its movement out of plane while not significantly inhibiting its ability to measure the applied loading.

Limited by the dimension of the loadcell, as indicated in Figure 4.9, the system was only allowed 7.5mm of rearward translation before the threaded rod would press against the inner wall of the loadcell and cause damage. Forward translation restrictions were similar at 9mm; the threaded rod disconnecting from the loadcell were it to be exceeded. With the aileron moment arm, however, this still allowed for a deflection of over 50° in both directions from zero deflection. The primary limiting factor to maximum possible deflection was, however, created by the link between the actuator rod and aileron leading edge rod. A maximum negative deflection of approximately $+10^\circ$ was achievable before the mechanism locked up against itself. A maximum negative deflection of approximately -45° was allowed before the mechanism would become over extended and was unable to return itself back to zero deflection unaided. In order to prevent this occurring, the aileron was not operated below a deflection of -40° .

Investigations of previous tests showed that any effective comparisons would ideally require deflections of $+25^\circ$ or higher. By using a symmetrical wing profile, however, it was seen that a negative aileron deflection with the wing at a positive angle of attack would be equivalent to a positive aileron deflection with the wing at a negative angle of attack. The wing would then be tested for the allowable aileron deflection range, of -25° to $+10^\circ$, for both the negative and positive angles of attack. Reversing the data for the negative angles of attack then ensured that a full swing of the aileron deflection could be tested. It also meant that for an aileron deflection range of -10° to $+10^\circ$ the data would ideally be repeated. This could be used to validate how well the external balance and hinge moment balance performed.

4.4 Data Acquisition

4.4.1 Data Acquisition Device (DAQ)

For the purposes of data acquisition a 16 channel NI USB-6211 multifunction DAQ was used. The DAQ had a 16 bit resolution, capable of input ranges of $\pm 0.2V$ to $\pm 10V$. Using an input

range of $\pm 0.2V$ the device had a precision, at full scale, of $0.088mV$ and a precision of $2.690mV$ when using an input range of $\pm 10V$. This uncertainty encompassed residual gain error, residual offset error and random noise. The signal resolution is quoted as $91.6\mu V$ and $4.8\mu V$ respectively for the two ranges. A maximum sampling rate of 250 kS/s was available, shared amongst all the channels. The full specifications of the DAQ can be found in Appendix C

Labview

Labview was used in order to process and record the data input into the DAQ. A sampling rate of 1000Hz was used for the measurements of the loadcell and potentiometer signals. While higher sampling rates were technically available from the DAQ, the computer system memory proved to be the limiting factor. Smaller sample rates would have been suitable for the purposes of the current testing as the loads were being examined under static conditions. It was decided, however, to rather have the system read in data at a higher rate as it was less likely that unwanted occurrences, such as blips in the supply voltage or the vibration of the wind tunnel, would affect the data in any substantial way. The effect of these disturbances and sampling rates is discussed later in chapter 6.

The data from the loadcells was recorded by Labview as strains rather than voltages. Preliminary tests showed that this setting produced a better signal quality than having the loadcell signals recorded as voltages. This is because the DAQ unit had inbuilt signal conditioning for strain inputs that further filtered the incoming signal. It was decided that the added uncertainty associated with the loadcell gauge factor used in converting the voltage input to a strain reading, still resulted in an overall better signal quality. The following equation is used by Labview to convert the voltage inputs into strain units.

$$\mu\varepsilon = \frac{1}{V_{EX} \times G \times 1000} \cdot V_{in} \quad 4.1$$

Where: $\mu\varepsilon$ micro strain; V_{EX} excitation voltage, V; G loadcell gauge factor; V_{in} measured voltage, mV

Input ranges for the loadcells were set at $\pm 1000\mu\varepsilon$ in Labview. This equated, using equation 4.1, to a voltage input range of $\pm 18mV$. The smallest range that the 16 bit DAQ could measure, however, was $\pm 200mV$. The signal resolution at this range was $4.8\mu V$ which equated to a resolution of $0.267\mu\varepsilon$ for the loadcells at full scale ($1000\mu\varepsilon$).

Further improvements to the signal were made through the use of filters and averaging functions. These are discussed further in chapter 6.

4.4.2 Atmospheric Data

Temperature DAQ

A separate single channel USB-TC01 temperature DAQ was used for the purposes of measuring the air temperature during the tests. This DAQ has a resolution of 20 bits allowing

for an accuracy of 0.6°C between 0°C and 65°C. A K-type thermocouple was plugged into the DAQ. The thermocouple was positioned in the wind tunnel, downstream of the test model and was shielded from the flow to eliminate convection effects.

Air Velocity

Airstream velocity was measured through the use of a DPM ST650M digital pocket manometer and pitot tube inserted into the airstream during testing. The device had a precision of 3% of the reading.

Pressure

Ambient air pressure was recorded during testing. This was done through the use of an AD-1000 pressure transducer. The transducer had a precision of $\pm 1\%$.

Humidity

The air humidity was manually recorded through the use of an Oregon BAR206 Weather Forecast Station. The device has a resolution of 1% for humidity.

4.4.3 Power Supply

Previous work conducted at the drawdown wind tunnel showed a high level of electronic noise was encountered; this being attributed in large part to the buildings' main power supply. Specifically an oscillating frequency was introduced into the system that the inbuilt filters of the data acquisition system had some difficulty in accurately filtering out. The use of a chargeable battery system was successful in isolating the electronics from the buildings power; this eliminating a lot of the noise encountered.

In order to power the actuation motor used in the hinge moment balance, a separate DC power supply was used. While this power supply was connected to the buildings power supply it was isolated from the rest of the instrumentation, being used solely to power the actuation motor and relays.

Battery Power Supply

6 12V lead acid batteries were used, each plugging into a custom made charging board that allowed the batteries to be charged in situ. It was found, however, that the charger had to be disconnected from the building power supply during the test otherwise the unwanted system noise found its way into the data.

The output voltage from each battery was regulated down to $9V \pm 0.1V$ using LM317 regulators before being sent to the instrumentation. In this way the input voltage to the loadcells and other instrumentation could be kept constant, at least until the battery voltage dropped too low. Through testing it was found that that from a full charge the batteries could operate for over 20hrs before the voltage supplied by the batteries would dip below 10V and the output voltage from the regulator would become inconsistent.

4.4.4 Wiring

In an effort to further reduce the signal noise that was encountered the use of shielded cable was investigated with positive results. In the end 2 core and 4 core shielded wiring were used in the wiring of the loadcells and potentiometer.

In certain cases 3m of cable were used to link the loadcells to the power supply and DAQ. Tests were conducted to ascertain what effect these long lengths of cable would have on the signal and corresponding noise levels. While an increase was noticed upon close inspection it was deemed to still be within satisfactory levels.

4.5 Flow Visualization

In order to aid in the explanation of possible phenomenon, flow visualization was required. This was achieved through the use of an SAI helium bubble generator. The device operates by creating and injecting helium filled soap bubbles into the airstream ahead of the test model. Careful adjustment of the ratio of helium to soap formula would allow the bubbles to be neutrally buoyant and more accurately represent the airflow. By blocking out all outside light and using a concentrated light source these bubbles would become illuminated and allow for a direct visualization of the flow field around the wing at test conditions.

These flow fields can then be photographed. By varying the shutter speed of the camera it becomes possible to view the individual bubbles passing over the wind tunnel model or, by increasing the exposure, create flow lines of varying lengths. This is valuable in the visualization of stall conditions, wingtip vortices and the interaction between separate bodies.

5 DATA PROCESSING

Data processing of the test results was primarily done through the use of Microsoft Excel and Visual Basic for Applications (VBA). The VBA code was used to pull the data from multiple sources, manipulate and process it. Further code would generate plots of the processed data, allowing for trends to be seen. These codes required the data files from the tests to be specifically named and placed in set folders. For the most part this was done during the testing however a quick run through the output files was done to ensure the files were where they needed to be and named correctly.

Gravitational Acceleration was taken as 9.79m/s^2 .

The following process was followed:

1. Data was pulled and collated from the separate test files into a single excel spreadsheet using a VBA code. This data would include: the angle of attack, the roll, yaw, and aileron hinge moment signal data along with the temperature. A separate column set pulled the standard deviation in each test set for each signal input, calculated for a 95% confidence interval. The value recorded from each signal input was averaged over the test time.
2. The rows of data read in would alternate between zero load values and test load values. Checks were made through the data based on the signal noise levels, indicated by the standard deviations, to identify areas of concern. For those points that were identified, the original output files were examined to see what caused the error. These data points would be subsequently removed from the data set were they found to contain an error or random occurrence.
3. A second VBA code was written to zero the signal values, subtracting the zero load signals from the test load values. The standard deviation values for the test load cases were kept, the values at zero load simply consulted in the previous step to ensure the data was satisfactory. Both the zero load and test load potentiometer voltage values were kept as this allowed for the tracking of aileron deflection change as the tunnel was turned on.
4. The aileron deflection calibration was then applied using the potentiometer voltage signal. The speed values at each of the tests were manually inputted, from the recordings made during testing. The aileron deflection calibration was applied to the total voltage signal and not a difference between the zero load and loaded cases, as done with the loadcells.

5. As mentioned previously the rolling and yawing moments would be calculated in a similar manner as to that done by Rogallo and Purser (1941). In this method the rolling moment was calculated from the difference in the measured load with the aileron at zero deflection and in the reaction loads with the aileron deflected. Due to the difficulty in attaining a precise deflection angle this was accounted for by having a polynomial fitted to the data plot of the loadcell load for a set angle of attack and the y intercept for each equation found. This value was then subtracted from the raw data, offsetting roll and yaw signals, for a set angle of attack, to obtain the change in rolling and yawing moment by deflection in the aileron. By using the change in signal data, rather than an absolute, it also meant that any drift in the zero load signal data due to temperature change should not need to be accounted for. The effect of temperature is discussed further in 6.2.4.

6. The data set for the negative angle of attacks was then combined with that of the positive angle of attack, this being possible due to the symmetrical nature of the wing. Along with inverting the direction of the angle of attack the following values were also inverted: aileron deflection, rolling moment and hinge moment. Drag was not inverted as illustrated in Figure 5.1.

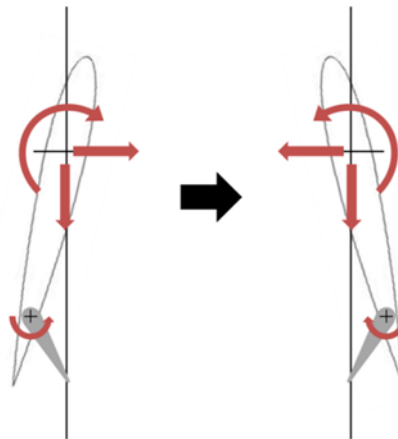


Figure 5.1: Property mapping due inversion of the wing about the x-y plane

7. The calibration equations and matrices were applied to the test data.

8. Finally the moment loads were reduced down to their respective aerodynamic coefficients using equations 2.2, 2.3 and 2.4.

6 ERROR PROPAGATION

This chapter deals with the data error propagation in the measurement system used. In order to accomplish this, a number of factors were investigated. Firstly the manner in which the uncertainty in the signals was calculated is presented. The signal resolution brought on by changes in load, ghosting effects and temperature variances were subsequently reviewed and examined. The nature of the data being recorded was then investigated which included the effects of the filters and averaging placed on the data.

6.1 Data Uncertainty

The procedure followed when calculating the uncertainty in the measured loads and signals is briefly discussed in this chapter. For the list of equations used refer to Appendix D. These equations were derived from Holman (2012).

The standard deviation of the signal data was calculated, using equation D.1, for the loadcell and potentiometer inputs. A confidence interval of 1.96, relating to a 95% confidence level was applied to the standard deviation to obtain the uncertainty in the signal data itself. The uncertainty in the measured strain values was then calculated using equation D.2. This took into account the uncertainties in the signal data, excitation voltages and the loadcell gain.

The uncertainties in the rolling, yawing and hinge moment loads were calculated using equations D.8, D.9 and D.10. These equations considered the calculated uncertainty in the loadcell signal and the uncertainties due to the calibration process. The calibration uncertainty took into account the orientation of the loads, moment arms and the accuracy to which the applied mass pieces could be measured. The uncertainty values and sources thereof for the load calibration are discussed in chapter 7.

Finally the uncertainties in the aerodynamic coefficients for roll, yaw and hinge moments were calculated using the previously mentioned uncertainties as well as the uncertainties in the velocity, pressure and dimensions of the wind tunnel model. These values are discussed in chapter 8.

6.2 Signal Resolution

The resolution of the measurement system to signal inputs and disturbances is discussed here.

6.2.1 Loadcells Signal Resolution

Each loadcell to be used in the external balance and hinge moment balance were setup in such a way as to have a load applied to them directly. In this way the responsiveness of the loadcells, external of the balance setups, could be seen and verified. This would aid in the explanation and understanding of the nature of the outputs from the two balances. The setup and procedure followed for each case can be found in Appendix E.

The variation of the measured strain in the yawing moment loadcell with an increase in direct loading is shown in Figure 6.1. A linear regression was fitted to the data, the fit having an R^2 value of 1.000. The same result was obtained when the rolling moment loadcell was loaded in the same manner. This was expected as the rolling and yawing moment loadcells were manufactured by the same company.

The data obtained from the check of the hinge moment balance loadcell is shown in Figure 6.2. As with the external balance loadcells, a linear regression could be fitted to the data. Again an R^2 value of 1.000 was attained for the linear regression.

From Figure 6.1 and Figure 6.2 it was seen that the signal from the loadcells increased linearly with an increase in load. The loadcells were also noted to respond equally for both positive and negative loading cases. Considering the quality of the fit and the signal resolution of the DAQ, discussed in chapter 4.4.1, the uncertainty in the measurements due to the quality of the loadcells themselves was considered negligible. Any uncertainties or deviations from expected trends for the balance systems would not be attributable to the loadcells themselves.

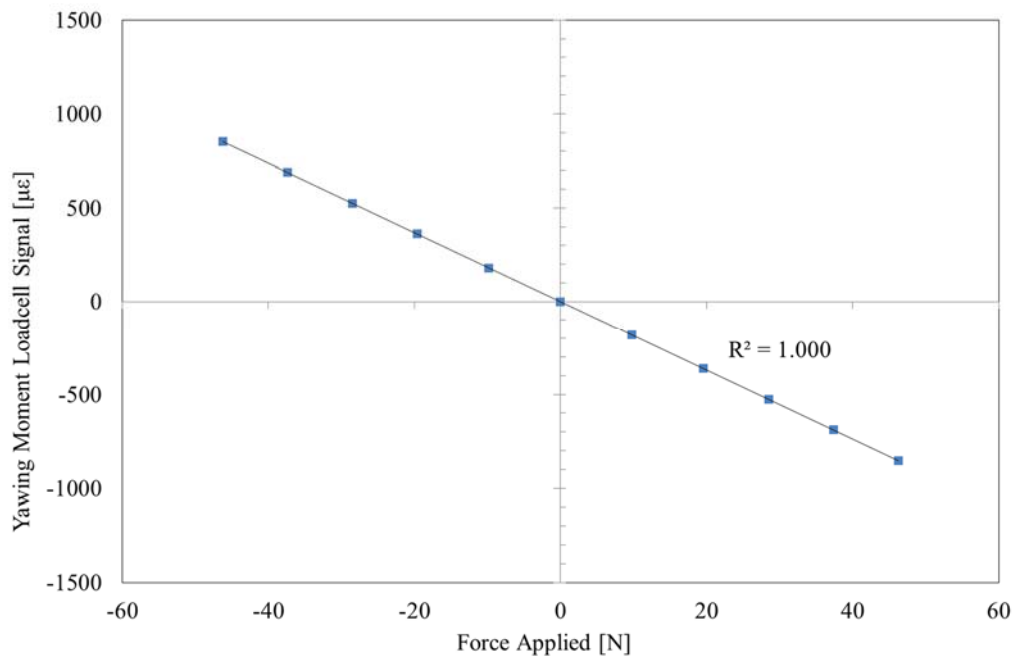


Figure 6.1: Variation in yawing moment loadcell signal, measured in $\mu\epsilon$, with an increase in mass directly applied to the loadcell.

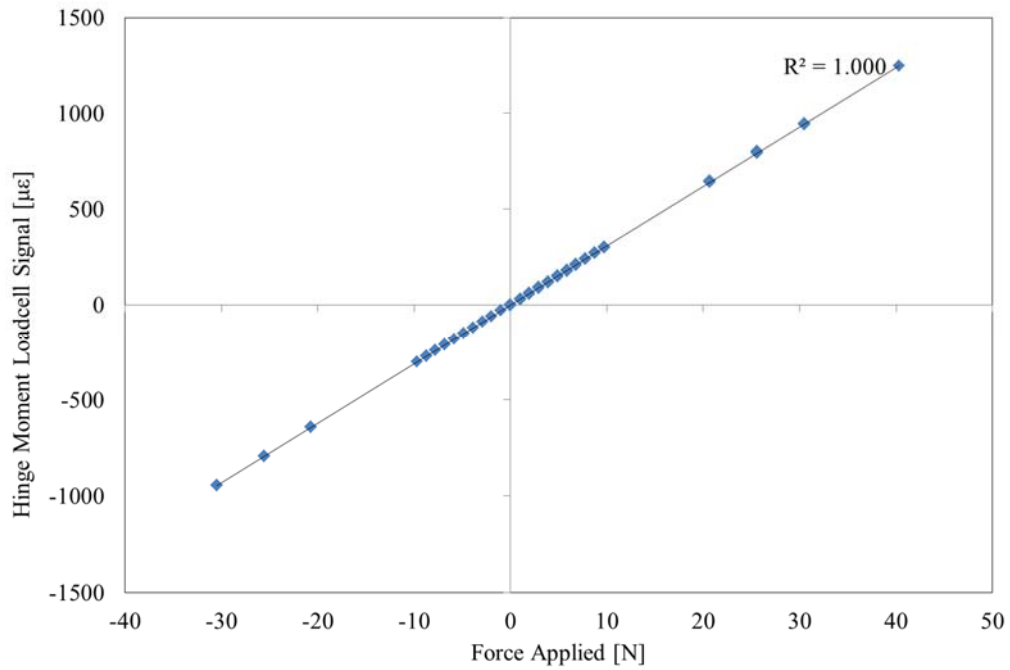


Figure 6.2: Variation in hinge moment loadcell signal, measured in $\mu\epsilon$, with an increase in mass directly applied to the loadcell

The above data also allowed for the responsiveness of the loadcells to be determined. Using the loads that the loadcells were expected to see, as stated in chapter 4.2 and 4.3.4 and repeated here, the maximum change in $\mu\epsilon$ that was expected from each of the loadcells could be calculated. Refer to Table 6.1.

Table 6.1: Approximate loads and change in signal values to be measured by each of the three loadcells during testing.

Loadcell	Load [N]	Max Signal Change [$\mu\epsilon$]	DAQ resolution [% max load]
Rolling Moment	20	~205	0.13
Yawing Moment	6	~110	0.24
Hinge Moment	15	~455	0.06

The DAQ resolution is expressed, in Table 6.1, relative to the max signal change expected. This is based on the signal resolution of the DAQ being $0.267\mu\epsilon$ for the loadcells as previously stated in chapter 4.4. The values quoted are approximate and were used simply as a reference point when considering the significance of signal uncertainties.

6.2.2 Potentiometer Signal Resolution

The potentiometer was used to measure the aileron deflection. Signals from the potentiometer circuit were measured into the DAQ as voltages. A voltage range of $\pm 10V$ was used for the signal. Using this range the DAQ had a resolution of $91.6\mu V$. As mentioned previously the

minimum measurable aileron deflection was required to be 5° based on the measurement system requirements, stipulated in chapter 3.2. A 5° deflection change would result in a measured voltage change of 0.1V across the potentiometer. The DAQ resolution was therefore seen as being more than suitable for the purpose.

6.2.3 Ghosting Effect

One of the effects that were checked for was that of ghosting between the loadcell signals. Specifically, the ghosting effects with regards to the change in signal for one loadcell when another loadcell was loaded. While the system had been designed and wired up in such a way as to prevent this occurring it was still seen as necessary to check nevertheless. This was checked by wiring up the three loadcells, measuring the rolling, yawing and hinge moments. Each loadcell was then individually loaded and the signals recorded for all three loadcells. Comparisons between the signal data would then allow for the detection of any ghosting effects that may have occurred. In this way the electrical system was checked for errors such as dry solder joints, grounding issues and failures in the system. The data in Figure 6.3 is typical of the data obtained in each of the load cases. Figure 6.3 is for a pure yawing moment load case.

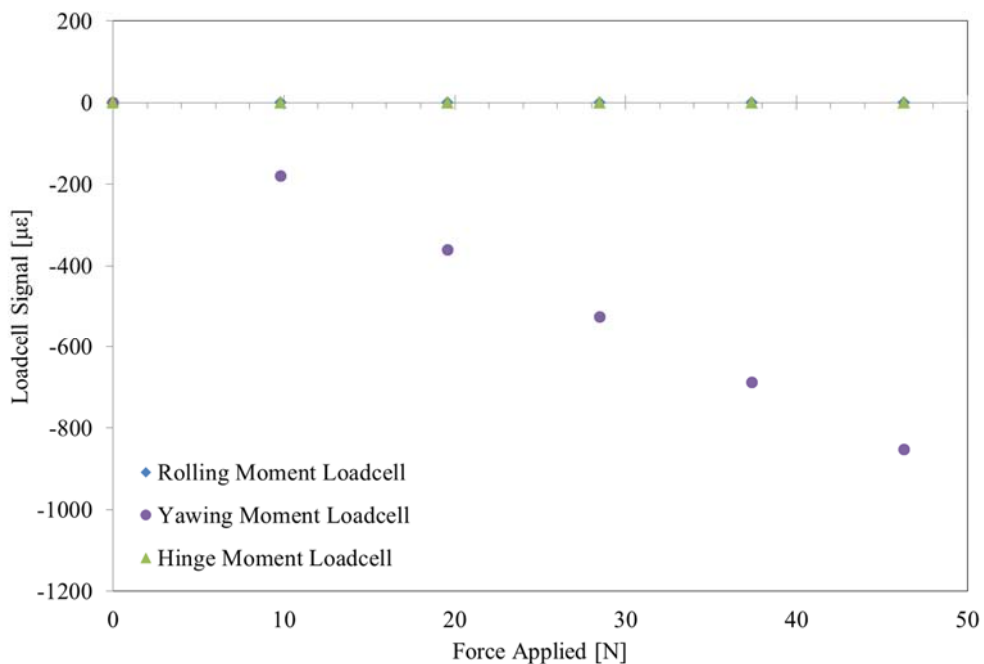


Figure 6.3: Change in loadcell signals, measured in $\mu\epsilon$, recorded for each loadcell when a yawing moment was applied.

From Figure 6.3 a clear distinction can be seen between the signal data recorded for the yawing moment loadcell and the other two loadcells. The signal inputs from the rolling, and hinge moment loadcells varied by less than $0.5\mu\epsilon$ over the range of loads applied. As the DAQ was only sensitive enough to pick up $0.267\mu\epsilon$ the variance of the signals for the rolling and hinge moment loadcells was seen as negligible.

No discernible trend of the signals against the increase in applied load was noticed either. If any ghosting effects were present in the system they were seen as negligible and no correction of the data was deemed necessary.

6.2.4 Signal Drift

In order to further characterise the system a test was run for over 20 hours to see what sort of drift could be expected from the system. A test of 24 hours was originally planned however at the 20 hour mark it was noted that the voltage supplied by the batteries in the power supply was getting too low for the regulators to continue working properly. Comparison of the loadcell data and temperature data recorded showed a correlation between the two data sets and was seen as the primary contribution to the drift in the signal data. The drift in the rolling moment loadcell signal data and comparison to the temperature is shown in Figure 6.4. The test window indicated on the graph indicates the times during which the primary tests were conducted. This window was chosen based on the temperature variance recorded over the time period, the test window occurring over a time for which the temperature was relatively stable.

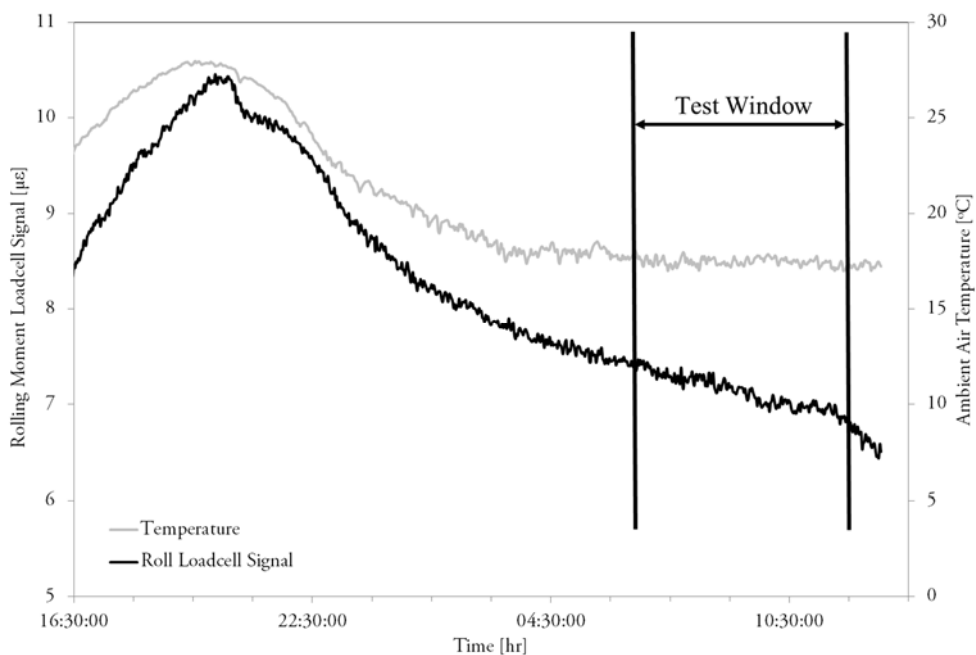


Figure 6.4: Variation of rolling moment loadcell signal over a 20 hour period plotted against the variation in ambient air temperature over the same time.

The plotted data showed a fairly distinct drift in the zero load signal value recorded. This drift is, however, only around $4\mu\epsilon$ over the entire time period. During the test window this drift was approximately $0.5\mu\epsilon$ or 0.25% of the full scale signal. The DAQ was only sensitive to changes of $0.267\mu\epsilon$. The tests time lengths were also expected to be relatively short, less than one minute each. Based on this, the effect of changing ambient air temperature and corresponding drift of the signal data was seen as negligible during testing. It was therefore seen as unnecessary to correct for signal drift during testing.

6.3 Data Distribution and Manipulation

The distribution of the raw rolling moment data is shown in Figure 6.5. This data was taken from a test conducted at 15° angle of attack with the aileron deflected approximately 10° . At that angle of attack the wing had stalled and was noted to experience relatively high oscillations due to the separating airflow. Despite this the distribution of the data was seen to approximate that of a Gaussian distribution, this being shown in Figure 6.5. For the sample size of nearly 40000, this was expected. The distributions of the raw yawing and hinge moment data were similar to those shown in Figure 6.5.

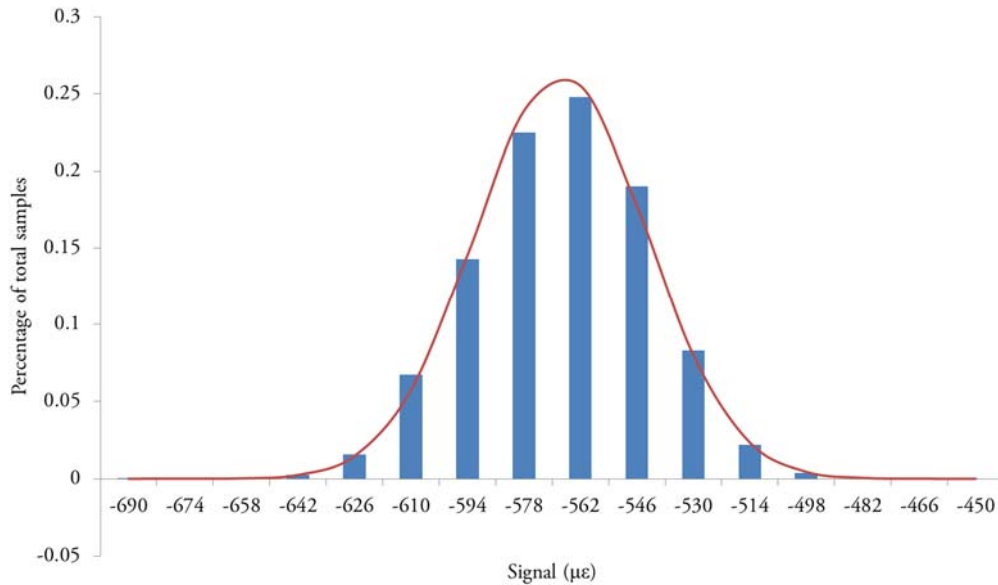


Figure 6.5: Distribution of rolling moment raw signal data, measured in $\mu\epsilon$, obtained from a single test plotted against a Gaussian distribution, 15° AoA, Thickness 2, $\delta=-10^\circ$, $V=14.7\text{m/s}$.

With a confidence level of 95.0%, the uncertainty of the above data was calculated at $47.8\mu\epsilon$. This is approximately 13.5% of the max signal change that was expect and as such was seen as too high. Evaluating the signal it was seen that there was a large amount of signal noise. In order to try and reduce this noise filters were applied to the data. The first filter was a lowpass filter. The cutoff frequency was chosen by performing a fourier transform on the data set and evaluating the frequencies picked up by the measurement system. Peaks in the data indicated signals were being introduced at high frequencies over 10 Hz. These signals were likely brought on by the vibration of the wind tunnel and external balance. After experimenting with various cutoff frequencies for the lowpass filter, 5Hz was chosen as the optimum value. In this way the noise levels in the signal data were reduced, however the signals being introduced due to the static aerodynamic loads not being altered or removed. This was interpreted based on the average signal of the filtered data being the same, within the resolution of the DAQ, as that of the raw data. The effect on the data of the lowpass filter is shown in Figure 6.6.

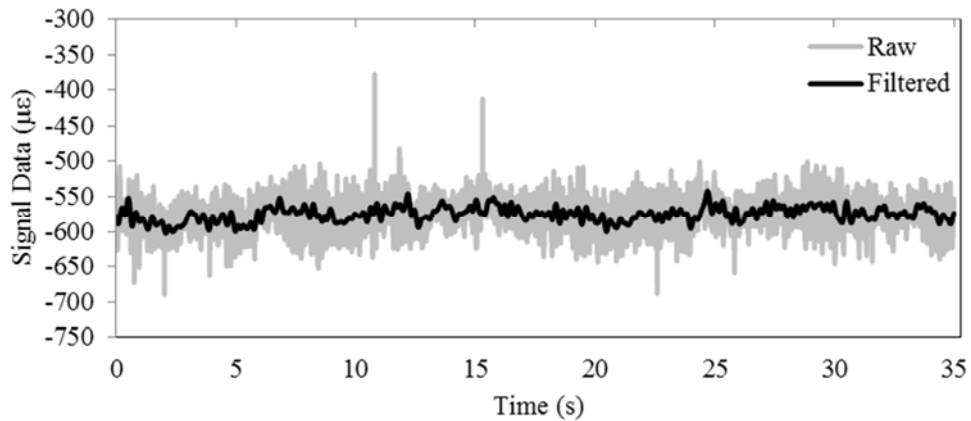


Figure 6.6: Comparison of raw and filtered rolling moment signal data from example test, 15° AoA, $\delta=10^\circ$, $V=14.5\text{m/s}$. Lowpass filter of 5Hz applied.

The second filter was a moving average filter. This filter further removed random noise being introduced into the system that was not removed by the lowpass filter. After having passed through both filters the data had an uncertainty of $12.3\mu\epsilon$ with a confidence level of 95%. This was only 2% of the maximum signal change expected.

The data acquisition computer, however, was incapable of logging and saving nearly 40000 samples for each of the 4 loadcells and the potentiometer. After a few moments the computer would run out of memory and the program would crash. In order to deal with this the data was averaged. This was done by averaging over every 100 samples once having passed through the filters. Checks were made to ensure that the average of the raw and averaged data sets was maintained. For the most part the averages of the two data sets were within the signal resolution of the DAQ. Occasionally the averages would deviate by as much as $1\mu\epsilon$ or $2\mu\epsilon$. Those particular tests were found to have irregular trends in the data that could be picked up in post processing and were subsequently excluded from the data set. The uncertainties in the final averaged data, compared to the filtered data, were of similar magnitudes at 2% of maximum signal change.

7 CALIBRATION

The setup and procedure followed for the calibration of the external balance and hinge moment balance is specified in Appendix F. These are briefly summarised in this chapter.

7.1 External Balance Calibration

Calibration of the external balance involved the attachment of an extension arm to the main balance arm. This extended the main balance arm into the wind tunnel cross section so that load could be more easily applied. Coupled loads were then applied to this extension in order to simulate the rolling and yawing moments being applied.

Figure 7.1 shows the rolling moment calibration results for the rolling moment loadcell. For all loadcells, used in the external balance, a linear regression was fitted to the data. The results of the data presented in chapter 6.2.1 showed that the loadcells responded linearly when a direct load was applied to them. Considering that the dimensions of the balance remained constant as load was applied, it was expected that the balance response to load would also be linear.

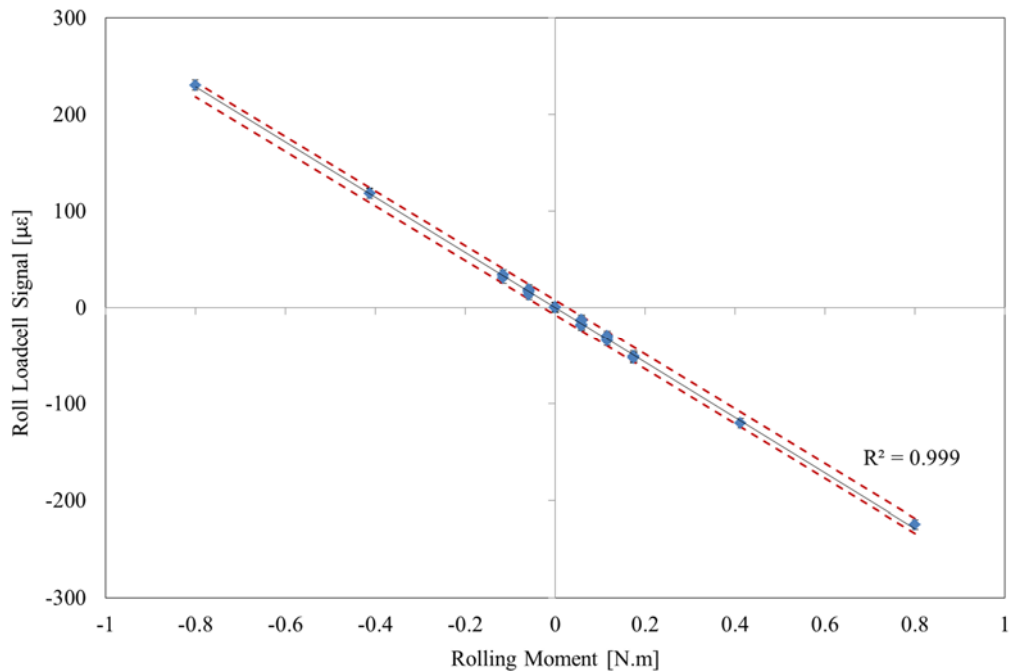


Figure 7.1: Rolling moment calibration results for the rolling moment loadcell

It was shown previously that the response of the loadcells for the application of a direct load was much better with no discernible hysteresis issues. The small deviations of the data, from the expected linear trend, were therefore attributed to the external balance system itself. The primary cause was likely due to inaccuracies in the calibration setup. These were taken into account in the calibration gradient uncertainty. Further hysteresis issues would have arisen due to the play in the rose joints used in the external balance assembly. As mentioned previously the joints allowed for a small movement in the system that could be minimized but not completely eliminated. Each time the system was loaded it would minutely change the external

balance configuration. A similar effect was encountered by the yawing moment loadcell during the yawing moment calibration. Despite this the R^2 values obtained from the linear regression fit to the data sets was considered to be close enough to unity for the data trend to be considered linear, especially for a 95% confidence level. The effects of the rose joints and misalignments in the calibration setup were thus considered to having been minimized to satisfactory levels. The data from the external balance calibration was therefore considered reliable in calculating the moment loads being applied to the external balance during testing.

The uncertainty in the rolling and yawing moment signal during calibration was taken as $2.5\mu\epsilon$. This was a conservative value based on the highest encountered uncertainty during the entire calibration process. The uncertainty in the applied moment was a function of the uncertainties of the applied mass, moment arm and load direction. The load direction was conservatively estimated at having a 1% accuracy as certain components were aligned by eye. Using this value and those for the mass and moment arm, an uncertainty of 1.4% was calculated for the applied moment. The uncertainty in the calibration gradient was then calculated to be 2.9% for the rolling moment loadcell during calibration of the rolling moment and 3.6% for the yawing moment loadcell during calibration of the yawing moment. Plotted as error bands on Figure 7.1 and Figure 7.2 these uncertainties can be seen to encompass all deviations in the data. It was thus reasoned that the calculated uncertainties in the calibration gradients encompassed not only the inaccuracies in the calibration setup but also the hysteresis issues due to play in the external balance system.

Every effort was made to minimise the cross coupling of loads as far as possible in the design of the external balance. Evaluations of the yawing moment loadcell signals recorded during the rolling moment calibration indicated that cross coupling had still occurred. This can be seen with reference to Figure 7.2. From the values given in Table 6.1 the maximum strain reading expected from the yawing moment loadcell, due to a yawing moment, was $110\mu\epsilon$. Figure 7.2 shows that the yawing moment loadcell experienced similar or higher values than $110\mu\epsilon$ during the rolling moment calibration. During the yawing moment calibration the rolling moment loadcell, on the other hand, only recorded strain values of $30\mu\epsilon$, or 15% of maximum strain, at the maximum expected yawing moment. The variance of the rolling moment loadcell signals during the yawing moment calibration were therefore significantly lower than for the yawing moment loadcell during the rolling moment calibration. The reason the yawing moment loadcell was more closely coupled to the applied rolling moment was attributed to the smaller expected yawing moments and higher resolution of the loadcell compared to that used for measuring the rolling moment. The use of a calibration matrix ensured that this cross coupling could still be accounted for nevertheless.

An unexpected result of the cross coupling that occurred between the rolling and yawing moment loadcells was the effect on the yawing moment loadcell during the rolling moment calibration. The effect, shown in Figure 7.2, indicates that the yawing moment loadcell would experience a load in the same direction regardless of the direction in which the rolling moment

was applied. Though unforeseen this effect can be understood by evaluating the external balance system and manner in which the system experiences loads. The result pointed to a flaw in the external balance configuration. A explanation of this effect, as it is understood, is given in Appendix G. Because of this effect it was necessary to apply separate calibration matrices dependant on whether the system experienced a positive or negative rolling moment. A similar effect would have been encountered by the rolling moment loadcell however aerodynamic yawing moments were only expected to occur in one direction. The effect was therefore not taken into account for the rolling moment loadcell.

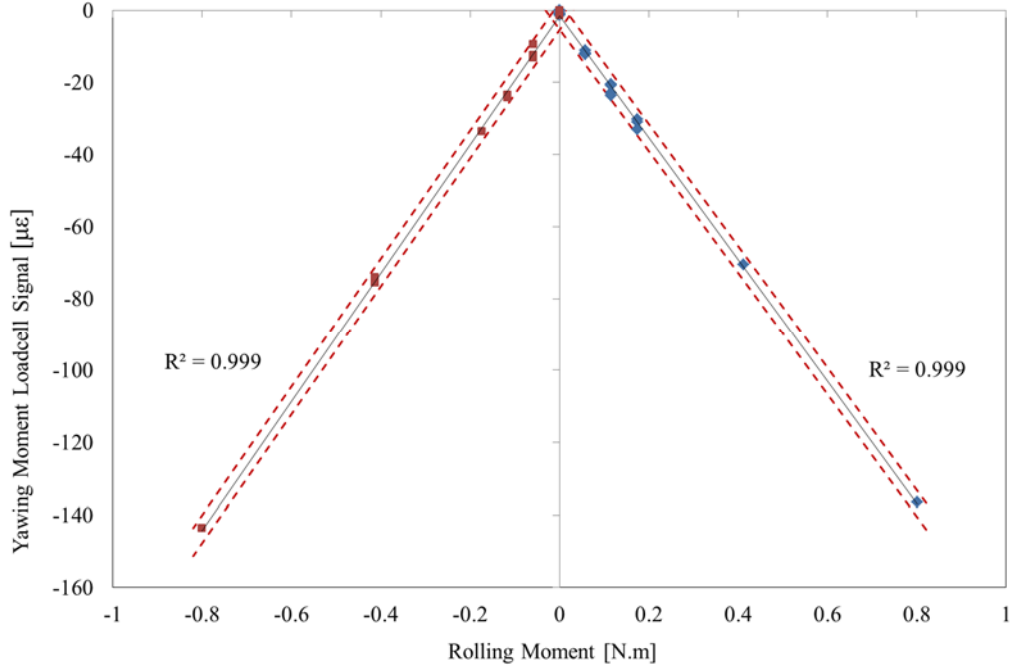


Figure 7.2: Rolling moment calibration results for the yawing moment loadcell

As before, the R^2 values were not exactly unity for the yawing moment loadcell during rolling moment calibration. The primary reason was attributed to the calibration setup and associated errors as well as the small play in the external balance system due to the rose joints used. The uncertainty in the calibration gradient was then calculated to be 2.9% for the yawing moment loadcell during calibration of the rolling moment and 3.6% for the rolling moment loadcell during calibration of the yawing moment.

The calibration equation for the positive and negative rolling moment cases are shown below. Refer to equation D.5 and D.6 for the explanation of the matrices below.

$$\begin{bmatrix} L' \\ N' \end{bmatrix} = \begin{bmatrix} -3609 & -1242 \\ 142 & 2081 \end{bmatrix} \begin{bmatrix} Sig_R (+ve) \\ Sig_Y \end{bmatrix} \quad 7.1$$

$$\begin{bmatrix} L' \\ N' \end{bmatrix} = \begin{bmatrix} -3439 & -1247 \\ 135 & 1983 \end{bmatrix} \begin{bmatrix} Sig_R (-ve) \\ Sig_Y \end{bmatrix} \quad 7.2$$

Where Sig_R Signal from rolling moment loadcell; Sig_Y Signal from yawing moment loadcell

All moments would be calculated in N.m

It should be noted that the rolling and yawing moment loadcell signals, used in the above two equations, were the processed signals after having performed step 5 in the chapter 5.

7.2 Hinge Moment Calibration

To calibration the hinge moment balance was done with the balance installed inside the wind tunnel model. With the wing secured on a level surface a modified aileron rib was secured to the aileron leading edge rod (refer to chapter 4.3.3). Loads were then applied onto this rib to simulate hinge loads being applied onto the aileron. Positive and negative aileron hinge moments were achieved by turning the wind tunnel model over onto its other side.

The result of the calibration of the hinge moment balance is shown in Figure 7.3.

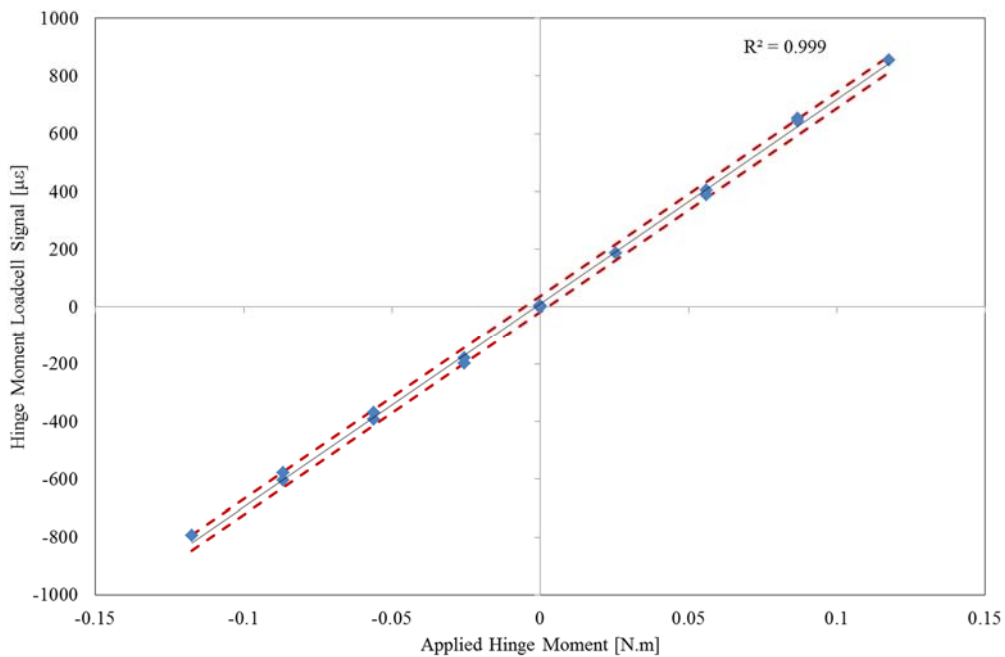


Figure 7.3: Hinge moment balance calibration plot

Unlike the external balance system where errors were attributed, in part, to the play in the rose joints, the hinge moment balance did not make use of rose joints. The setup used in the calibration of the hinge moment balance was seen as being less susceptible to errors, compared to the external balance calibration setup. The reasons for this are discussed in Appendix F. The linear regression fit and hysteresis issues that are evident in the calibration plot were therefore most likely due to other issues within the system itself. One of the contributors to the errors was the friction in the system that resulted in the hinge moment slipping as it was loaded and when the actuation motor deflected the aileron. Through the application of lubricant the friction issues could be minimized to a large degree but could not be eliminated. Secondly the actuation rod, labelled in Figure 4.9, had a small amount of flexibility that would see it bow out of plane under a high or oscillating load. Guide rails had been built into the design to prevent this; however, as with the friction in the system, the issue could not be completely eliminated. As

with the external balance calibration plots the R^2 value for the linear regression fitted to the above data was 0.999. The effects of the friction and flexibility of the hinge moment balance thus considered to having been minimized to satisfactory levels. The data from the hinge moment balance calibration was therefore considered reliable in calculating the moment loads being applied to the aileron during testing.

Further precautions were taken, during calibration and testing, whereby measurements were taken for an aileron sweep with the aileron moving in only one direction; a change in deflection direction of the aileron, by the actuation system, being found to alter the zero load reading. In this way the hinge moment balance was loaded, during calibration, in a similar manner to which the system would be loaded during the wind tunnel testing. It also meant that similar friction or flexibility issues that affected the data during wind tunnel testing would have occurred during the calibration. This allowed for a little more reliability in the calibration.

Checks were conducted to ascertain whether the calibration data would still be valid as the aileron was deflected. This was because, as the aileron was deflected, the effective moment arm between the aileron hinge axis and loadcell load axis would change. The hinge moment balance had been designed in such a way as for this to not be significant over the deflection range for which testing was required. Calibration plots were generated for the aileron at 3 distinct deflections, a high positive and negative deflection and a zero deflection. Comparisons between the three plots showed that the calibration gradient changed by less than 1% over the three cases. As such as the effect of the ailerons deflection was considered negligible when applying the hinge moment balance calibration.

The uncertainty in the hinge moment signal was calculated as $2.0\mu\epsilon$. This was a conservative value based on the highest average uncertainty during the entire calibration process for load cases. Due to the high level of accuracy to which the mass of the applied mass pieces were measured, their uncertainty was considered negligible in comparison to the uncertainty of the moment arms and applied load alignment. The uncertainty in the applied moment was thus calculated at being 2.2% of the applied moment. The uncertainty in the calibration gradient for the hinge moment balance was therefore calculated to be 2.5%, using equation D.3. This uncertainty is plotted as an error bands on Figure 7.3. As with the external balance calibration plots the uncertainty in the hinge calibration gradient can be seen to encompass all deviations in the data. It was thus reasoned that the calculated uncertainties in the calibration gradients encompassed not only the inaccuracies in the calibration setup but also the hysteresis issues due to friction and unwanted bowing in the hinge moment balance. This based on the similar nature in which the hinge moment balance was loaded during calibration and testing.

The equation used for calculating the hinge moments, based is given below

$$H_a = 138 \times Sig_H \quad 7.3$$

Where Sig_H Signal from hinge moment loadcell

7.3 Aileron Deflection

The results from the calibration of the aileron deflection are shown in Figure 7.4. The procedure followed to generate the calibration graph is detailed in Appendix F.

As mentioned previously the aileron was wired in series for the sake of simplicity and optimized to minimize the non-linearity in the data. By minimizing the non-linearity it ensured that there would not be any loss in resolution of the deflection measurements over the range of movement. Fitting a linear regression to the data resulted in an R^2 value of 0.996. As the pot calibration was independent of the rest of the measurement systems the use of a 2nd order polynomial fit for the data was not a problem. In this way the trend line would have an R^2 value of 1.000 and a higher accuracy for the aileron deflection measurement was possible. The application of the calibration data was therefore more accurate than if the equation from a linear fit had been used. The R^2 value of 0.996 for the linear fit was used as an indication that the resolution of the potentiometer in resolving the aileron deflections would be relatively constant throughout the deflection range being tested.

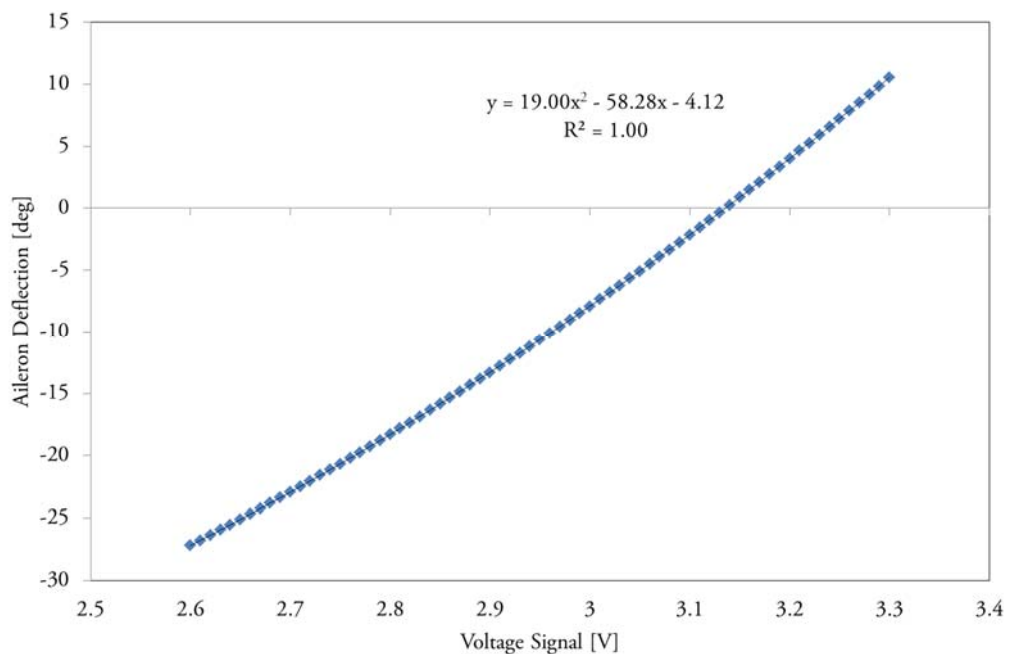


Figure 7.4: Aileron deflection calibration plot of deflection against voltage recorded

Uncertainty in the voltage signal recorded during calibration was 0.1mV. This is approximately the same value as the DAQ's resolution to the voltage input at the input range used (refer to chapter 6.2.2). It indicated that the potentiometer was well isolated from the rest of the measurement system, at least during calibration. Considering the uncertainty in the measured voltage, moments arms and measured deflections of the aileron, the aileron deflection measurement was taken as having an uncertainty of $\pm 0.1^\circ$. This was considered to be a conservative value based on an evaluation of the test results, with the actual precision of the instrument being lower.

From the calibration the following equation was derived.

$$\delta = 19.00V_{pot}^2 - 58.28V_{pot} - 4.12 \quad 7.4$$

Where δ aileron deflection, deg; V_{pot} measured voltage across the potentiometer, V

As mentioned in chapter 5, the measured voltage, applied to equation 7.4, was the total voltage. Unlike the measured loadcell signals, the voltage across the potentiometer was not zeroed during testing.

8 RESULTS AND DISCUSSION

The objectives of the current series of tests were: to design a rig capable of accurately measuring the rolling performance of an aileron during wind tunnel testing; validate the results obtained by comparison to previous research; and analyse the effect of thicker trailing edge thicknesses for ailerons. In order to achieve these objectives the current investigation focused on the measurement of the rolling, yawing and hinge moments that were generated during the wind tunnel tests. Other aerodynamic forces such as lift, drag and pitching moment were seen as less prevalent based on evaluations of the research performed into aileron performance in the past.

The aerodynamic moments were measured for a range of angles of attack and aileron deflections similar to those used in previous research by the likes of Rogallo (1941) and Wenzinger (1931).

Validation of the measurements was done based on the evaluation of a typical data set, analysis of the flow visualization and comparisons to previous work. Once the measurement system and the data obtained from it had been validated it allowed for the effect of thicker trailing edges to be commented on.

8.1 Typical Data Set

This chapter deals with the evaluation of a typical data set for the recorded signals. This works towards the verification of the measurement systems performance and discusses certain sources of uncertainty in the data.

Restrictions on the aileron actuation system meant that the maximum positive and negative aileron deflections were not the same. The range for which data could be obtained was therefore asymmetric about the zero deflection angles. Figure 8.1 illustrates this by showing the data obtained for two opposite angles of attack of $\pm 5^\circ$. The aerodynamic loads experienced by a symmetrical aerofoil, such as the NACA0012 used, will be equal and opposite for opposite angles of attack. It was reasoned, therefore, that by reversing the load directions and magnitudes of the measured moments a more symmetrical and larger range of aileron deflections could be tested. The way in which these loads were reversed was shown in Figure 5.1.

The test data for 5° angle of attack was chosen as this case was well below the angle at which stall occurred. Issues with the reversal of the loads and their implications on the data can therefore be more easily attributed to issues other than the separation of the airflow on the aerofoil surface brought on by stall. For obvious reasons this could not be shown for the 0° angle of attack case – the test case furthest from any stall condition - as there were no opposite data sets to reverse.

The result of the load reversal is shown in Figure 8.1 for the yawing moment signals. Similar results were observed for the rolling and hinge moment signals however the result was simply more clearly evident in the yawing moment signal.

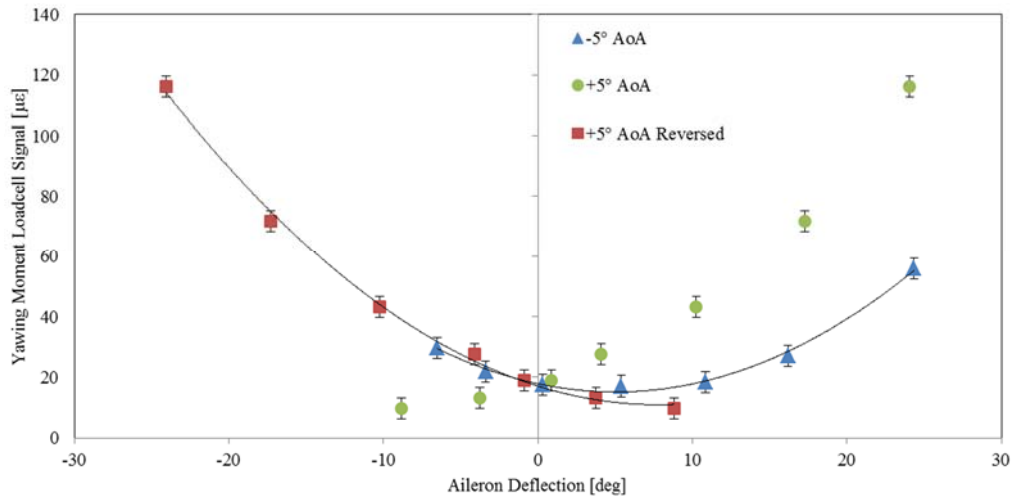


Figure 8.1: Zeroed yawing moment loadcell signals, including reversed signals, -5° and $+5^\circ$ AoA, plain sealed aileron, Thickness 2, $V=14.6\text{m/s}$.

The trend lines were fitted, in Figure 8.1, to give an approximate indication of the differences between the positive and negative angle of attack data sets over the common aileron deflections. It would be expected that if the loads were symmetrical for opposite angles of attack, the signals would correlate over the aileron deflection range that was common to both data sets. Depending on the test, this range was typically between $\pm 10^\circ$ aileron deflections.

There is a good correlation between the yawing moment signals for the negative aileron deflections. For the positive aileron deflections, however, there is a slight divergence noticed in the trends. This could be due to a few factors. If the wing was not completely symmetrical due to manufacturing flaws the reversal of the signals would not correlate as expected. The data trends between the positive and negative angle of attack cases would appear skewed and offset. This would be seen for all 3 moments, rolling, yawing and hinge, were it the case. Figure 8.3 shows the rolling moment signal trend that was obtained for the same test condition as the yawing moment signals, shown in Figure 8.1. Over the $\pm 10^\circ$ aileron deflection range the correlation is good for both the positive and negative deflections. Any deviation is well within the uncertainty for the data points. While the symmetry of the wing cannot be said to be perfect based on this, any asymmetry is considered negligible.

The apparent difference between the positive and negative angles of attack data sets for the yawing moment is likely due to a combination of the yawing moment resolution and uncertainty in the signals. The results of the calibration showed that the yawing moment loads were very

sensitive to changes in the rolling moment, leading to a significant cross coupling that occurred between the two measurements. This made the yawing moment loadcell more susceptible to disturbances in the system. The rolling moment loadcell, on the other hand, was less sensitive to such disturbances. This further explains why the correlation between the positive and negative deflections for the rolling moment signals in Figure 8.3 is much better than for the yawing moment signals in Figure 8.1.

The uncertainty values shown in Figure 8.1 are those of the strain values. At $\pm 5^\circ$ angle of attack these values were $\pm 2.5\mu\epsilon$ or approximately 2% of the maximum load. These values, expressed as error bars in Figure 8.1, can account, in part, for the noted divergence of the yawing moment signals. Combined then with the higher resolution of the yawing moment signals, compared to the rolling and even hinge moment signals, the divergence in the signals can be explained. It was understood to mean that the analysis method of reversing the signals of the opposite angle of attack was valid. The resolution of the external balance to yawing moments, however, is therefore lower than that shown by the uncertainty values. Further interpretation of the yawing moment data would then need to take this into account.

One further observations that can be made of the data shown in Figure 8.1 deals with the specific aileron deflections from which the moments were recorded. Evaluation of the data for the negative and unreversed positive angles of attack show a distinct difference in the increments of aileron deflections for which data was recorded. The uncertainty in the measured aileron deflection was on average $\pm 0.1^\circ$. This then does not account for the differences noted. It was intended to test at specific aileron deflections and be consistent with these throughout the tests. In this way it would have made comparisons between the results for the different aileron thicknesses, easier. Unfortunately the aileron and hinge moment balance was found to deflect in a slightly unpredictable manner as aerodynamic loads were applied to the aileron. This deflection was expected however the random variances were not. Actuation of the hinge moment balance under load was found to offset the zero load signal value, meaning that the change in load on the loadcell could not be calculated. The aileron could therefore not be precisely set to a specific deflection, once under load, during testing. This was not significant in the processing of the data as the aileron deflection was measured directly. It implied, however, that hinge moment balance and aileron system did not respond exactly the same way each time. The significance of this will be discussed later on.

The calibration matrix was applied to the rolling and yawing moments from each data set. The cross coupling in the external balance meant that the trends of the two moments were adjusted slightly after the application of the matrix. This can be seen in both Figure 8.2 and Figure 8.3 for the yawing and rolling moments respectively. The yawing moment loadcell was, as discussed, more sensitive to applied loads. The data points therefore experienced larger changes to the trend than the rolling moment loadcell data points. The implication of this is that the recorded signals from the loadcells cannot be evaluated on their own without the application of the calibration matrix beforehand.

With the application of the calibration matrix the uncertainty values in all three moments, roll, yaw and hinge, increased from those for the strain values. The uncertainty in the strain values accounted for the distribution of the recorded data samples and the uncertainty in the gain and excitation voltage. It did not account for any uncertainty due to the external balance itself, such as that due to play in the system. These were understood as being accounted for in the uncertainty in the calibration gradients. The uncertainties in the moments were therefore expected to increase.

Compared to the hinge moments and rolling moments, the latter shown in Figure 8.3, the uncertainty values of the yawing moments appear significantly higher. The uncertainty in the rolling and yawing moments, were 6.5% and 6.0% of the maximum moments for the 5° angle of attack tests. The uncertainty values are not necessarily higher for the yawing moments. Instead the differences are simply due to a difference in the scale of the y-axis.

The correlation of the yawing moment data over the $\pm 10^\circ$ aileron deflection range, shown in Figure 8.1, was previously attributed to the uncertainty in the data. The resolution of the external balance to yawing moments was seen as being lower than that indicated by the uncertainty values of the strain signals alone. Interpretation of results was then more difficult, especially for small changes in trends. With the inclusion of the uncertainties from the calibration, presented in Figure 8.2 the uncertainty can account for any apparent divergence between the yawing moment data points from opposite angles of attack. The resolution of the external balance to yawing moments was thus understood as being better reflected.

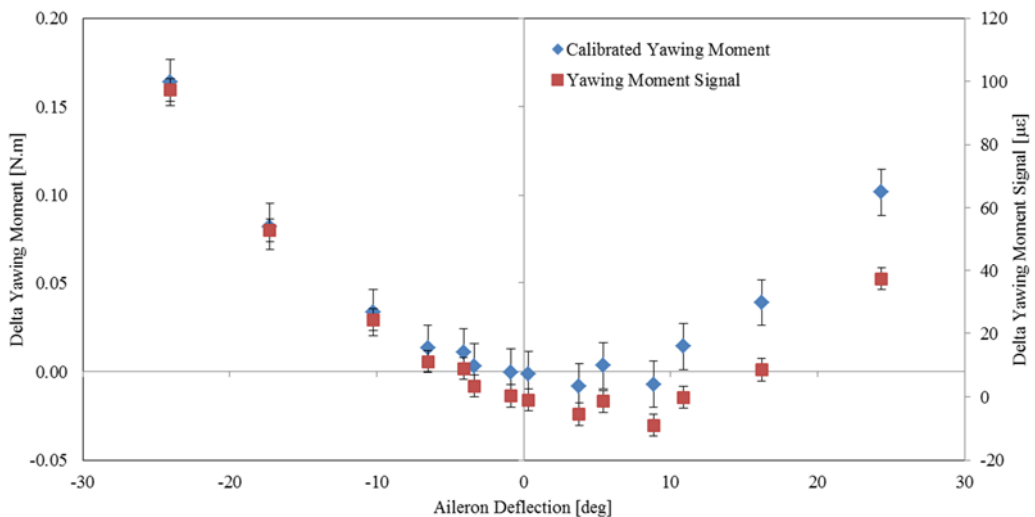


Figure 8.2: Comparison of data before and after application of calibration for yawing moment loads at 5° AoA, plain sealed aileron, Thickness 2, V=14.6m/s

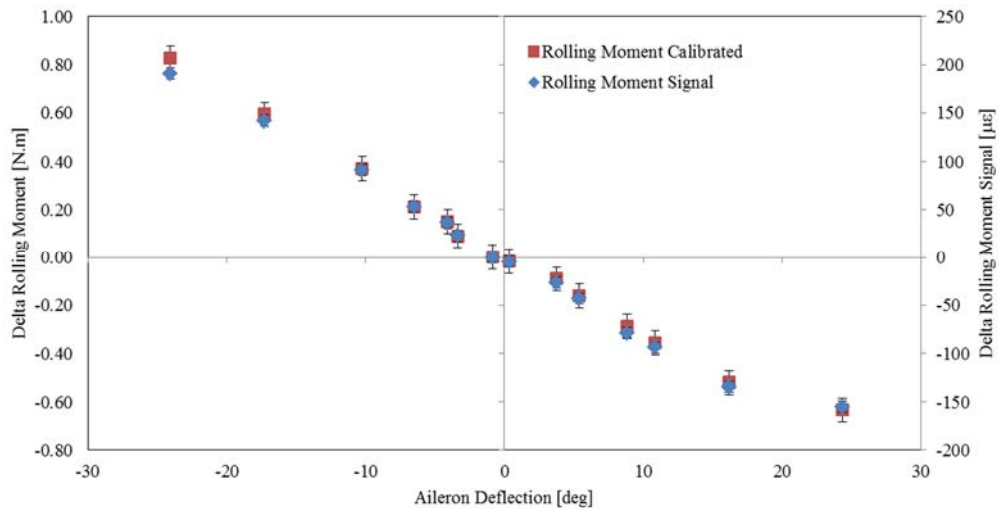


Figure 8.3: Comparison of data before and after application of calibration for rolling moment loads at 5° AoA, plain sealed aileron, Thickness 2, V=14.6m/s

An example of the processed data, in the form of the aerodynamic coefficients, is shown in Figure 8.4 for the yawing moment coefficient. Uncertainties in the velocity, air pressure, temperature and dimensions of the wind tunnel model increased the uncertainty of the yawing moment coefficient from 6.0% to 6.7%. The rolling and hinge moment coefficients saw similar increases. Comparisons between Figure 8.1, Figure 8.2 and Figure 8.4 show that the primary contribution to the uncertainty in the aerodynamic coefficients was thus due to the calibration gradient uncertainty and the associated factors that it was understood to encompass.

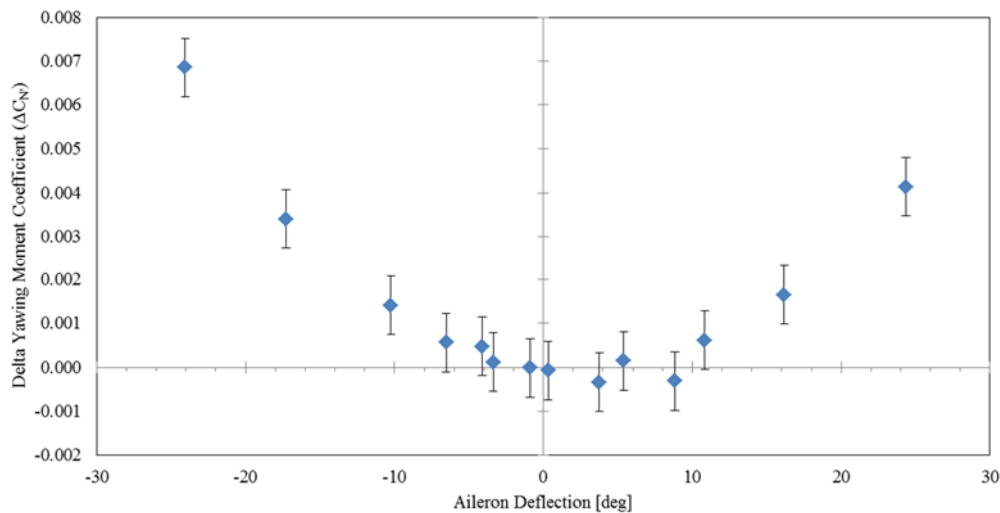


Figure 8.4: Yawing Moment Coefficients at 5° AoA, Thickness 2, V=14.6m/s

The rolling and yawing moment coefficients had an uncertainty of 7.2% and 6.7% respectively. This was more than double the required precision on 3% as specified in chapter 3.2. With the primary focus of the research being measurement of the hinge moments, the higher uncertainties in the rolling and yawing moment coefficients were seen as less consequential.

The hinge moment coefficients had an uncertainty of 4.2%. This too was above the required 3% precision, however it was not seen large as to warrant a redesign of the test rig. The performance of the test rig in terms of the requirements drawn up was then seen within satisfactory limits and suitable for the purposes of this research.

A final note on the uncertainty values for the aerodynamic coefficients, regarding the aileron deflection, should be made. It was found that the uncertainties for the three measured aerodynamics moments were relatively constant over the range of aileron deflections the tests were conducted for. An example of this is shown in Figure 8.5 for the hinge moment strain values. Of the three measured moments it would be expected that the hinge moments, and associated uncertainties, would be the most susceptible to effect of a change in aileron deflection. At high deflections the data shows an increased amount of scatter which reflects the effect of the separated airflow on the aileron. This was also the case for the rolling and yawing moment signals. These trends were found to occur for all angles of attack. To be conservative it was decided that when calculating the uncertainties, the maximum uncertainty value from the full aileron deflection range was used for each angle of attack test case. This meant that the uncertainties shown in the final data were conservatively overestimated.

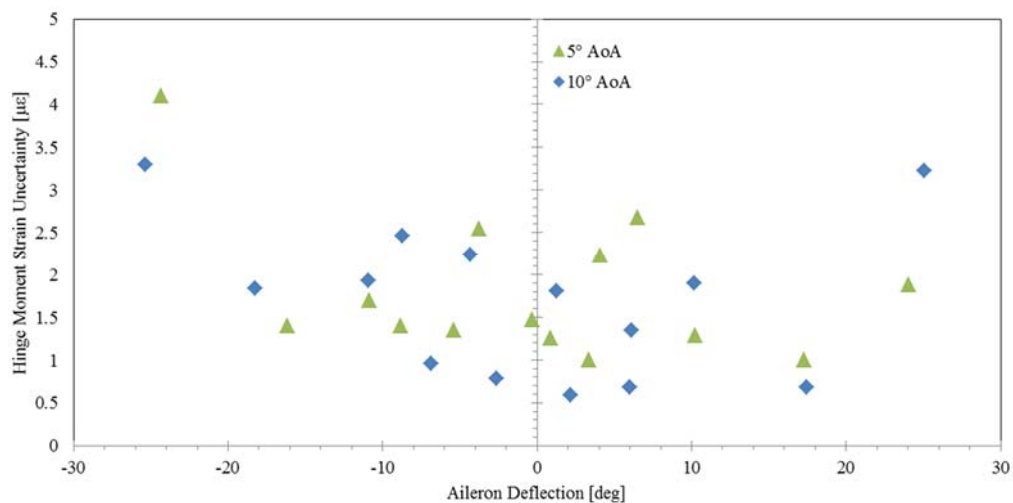


Figure 8.5: Variation of hinge moment strain uncertainty with aileron deflection for 5° and 10° AoA, Thickness 2, V=14.6m/s

8.2 Flow Visualization Results

As an accompaniment to the measured aerodynamic moments, flow visualization was performed on certain test conditions. These test conditions were selected based on a preliminary investigation of the test data. The investigation of the flow visualization images would be used to aid in the understanding and explanation of certain phenomenon.

The primary factor investigated with the flow visualization was the onset of stall and its effects on the aerodynamic moment coefficients. The results are presented in Figure 8.6, Figure 8.7, Figure 8.9, Figure 8.10 and Figure 8.11. Each image that was taken is shown alongside the

corresponding rolling moment coefficient data for that particular test. Stall affected the trend of all three aerodynamic moments. The hinge moment was more susceptible to the airflow stalling over the wing and aileron. The rolling moment coefficients better reflected the onset of stall.

For the flow visualization of the stall condition three angle of attacks were investigated, namely 12.5°, 15° and 20°. Based on the preliminary investigation of the data these three angles of attack were identified as representing the pre-stall, stall and deep stall cases respectively. The flow visualization image and corresponding data for the 0° deflection, 12.5° angle of attack case is shown in Figure 8.6. The rolling moment coefficients at this test condition showed little scatter in the data points over the aileron deflection range. It was noted that oscillations of the wing and aileron, brought on by the onset of stall, was found to increase the scatter in the data for all three aerodynamic moments. Up to and including the 12.5° angle of attack case the rolling moment coefficients all exhibited similarly low levels of scatter. It was therefore understood that above this angle of attack, from which scatter in the data increased, the wing had stalled. To confirm this, flow visualization of the wing was performed at this angle of attack. It showed that the streamlines remained attached to the wing over a large portion of the chord length. Only a small amount of separation was noted on the trailing edge of the wing. This was taken as an indication that the wing had just begun to stall. Due to the similarity of the scatter in the data obtained at 10° and 12.5° angle of attack, the 12.5° case, shown in Figure 8.6 (a) was therefore understood as still representing a pre-stall case for the purposes of this discussion.

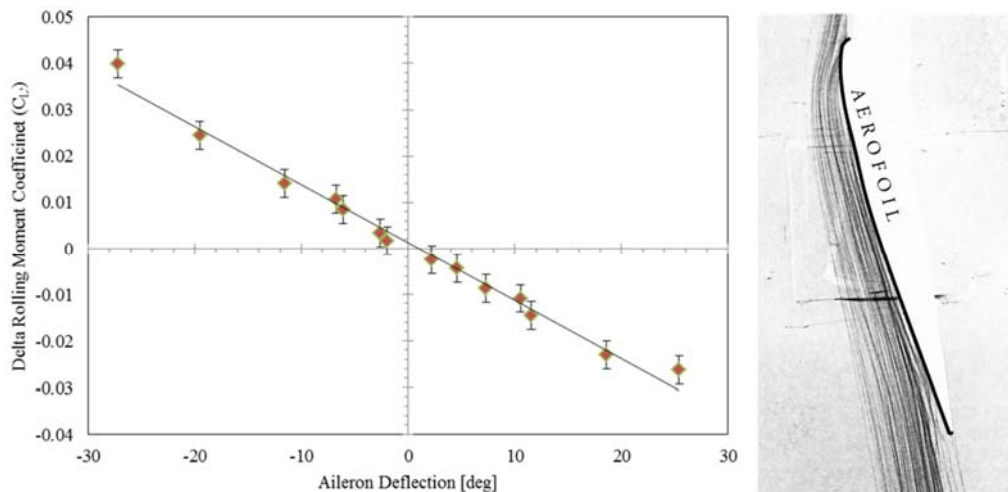


Figure 8.6: Rolling moment coefficient trend (a) and corresponding flow field (b) for 12.5° AoA, Thickness 2, V=14.6m/s

The flow visualization and rolling moment coefficients for the 15° angle of attack case is shown in Figure 8.7. As already noted the onset of stall was found to increase the scatter in the data. The relatively sudden increase in scatter was taken as a primary indicator that the wing was

almost fully stalled under the test condition being evaluated. Comparisons of the rolling moment coefficients for the 12.5° and 15° cases clearly show this increased level of scatter, as the degree of stall increased. Upon investigation of the flow visualization performed on the wing at 15° angle of attack showed an almost complete separation of the streamlines over approximately 80% of the surface of the wing.

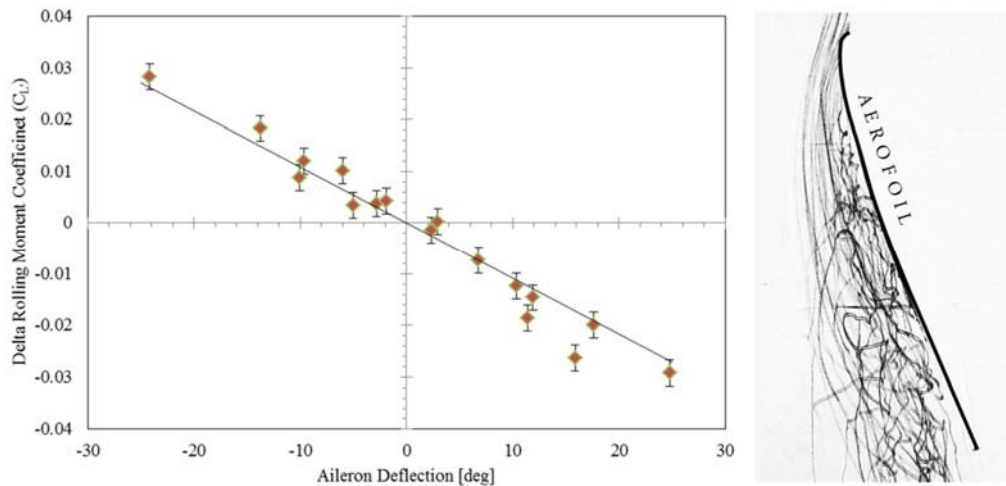


Figure 8.7: Rolling moment coefficient trend (a) and corresponding flow field (b) for 15° AoA, Thickness 2, $V=14.5\text{m/s}$

It was noted that as the wing was further and further stalled, the wing would experience large amounts of buffet. This was indicated in the data by the increased uncertainty in of the data points as well as the aforementioned scatter. Comparisons between the data shown in Figure 8.6 (a), Figure 8.7 (a) and Figure 8.9 (a) illustrate this. The uncertainties increased from 10% of the maximum value for the 15° case to 13% for the 20° angle of attack case. This buffet, due to the stalled airflow, was unavoidable. Due to the high uncertainty values at the higher angles of attack, it made interpretation of the trends more difficult. This was to be considered in further interpretations of the results.

The trend of the rolling moment coefficients for the wing, when it was not stalled, would be expected to be linear over an aileron deflection range of $\pm 10^\circ$. Evaluation of results from past research on ailerons such as that by Jones (1937) and Rogallo (1941) confirm this. A linear trend line was fitted to the 12.5° and 15° angle of attack cases over a $\pm 10^\circ$ deflection range. For both cases the rolling moment coefficients correlated nicely with these trend lines over the $\pm 10^\circ$ aileron deflection range as seen in Figure 8.6 (a) and Figure 8.7 (a). The two trend lines were also of approximately the same gradient.

At high positive aileron deflections, for the 12.5° and 15° angle of attack cases, in Figure 8.6 (a) and Figure 8.7 (a), the rolling moment coefficients diverged from the linear trend as was expected. For the 12.5° case this divergence occurred at approximately 25° deflection. For the 15° case the divergence occurred sooner at approximately 15° deflection. The flow

visualization for a high positive aileron deflection case is shown in Figure 8.8 (b). This was understood to be due to the separation of the airflow from the surface of the aileron, this separation visible in both images of Figure 8.8. Comparing the trend of the rolling moment coefficients at opposite deflections in Figure 8.7 (a), it can be seen that a clear divergence only occurs for positive aileron deflections. This is not as clear for the 12.5° angle of attack case in Figure 8.6 based on the uncertainty levels in the data. To understand why this occurred the two images in Figure 8.8 were investigated. It was seen that at high deflections the airflow would separate from the aileron surface on the downstream side, for both positive and negative deflections. For a positive deflection (Figure 8.8 (b)), however, the airflow also separated from the aileron surface upstream of the aileron. In this case the airflow was separated from both surfaces of the aileron. This would be expected to reduce the aileron effectiveness; a further increase in the aileron deflection resulting in little to no increase in the rolling moment of the wing. For the 15° angle of attack case, the divergence and levelling off of the rolling moment trends, resulted in the same rolling moment coefficient being achieved for an aileron deflection of 25° and 35° . Beyond 25° deflection the aileron is therefore ineffective.

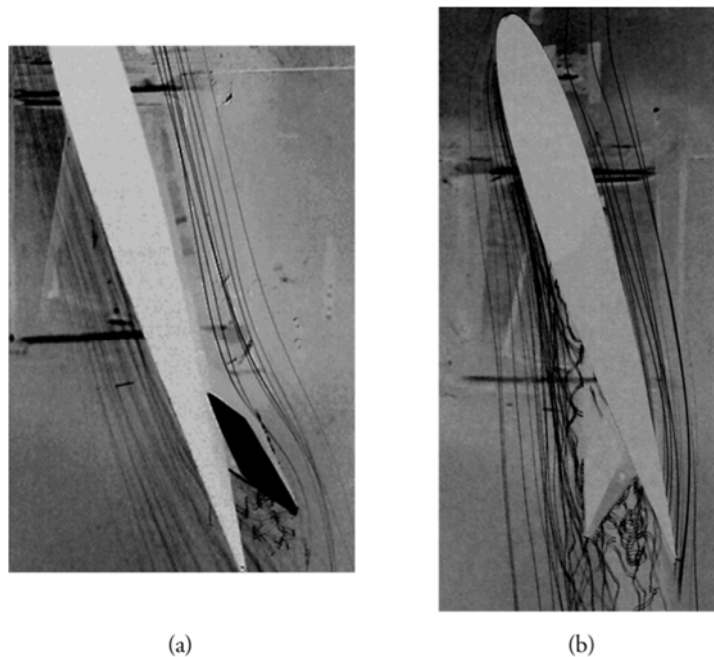


Figure 8.8: Flow visualization at 12.5° AoA, aileron deflection at -30° (a) and $+30^\circ$ (b),
Thickness 2, $V=14.7\text{m/s}$

It would be expected that the upstream separation of the airflow from the surface of the aileron, during a positive deflection, would occur sooner as the wing angle of attack increased; this explaining the increased divergence of the data for the 15° angle of attack case compared to the 12.5° angle of attack case.

For the 20° angle of attack case a trend line was once again fitted over the $\pm 10^\circ$ deflection range. As is seen in Figure 8.9, compared to Figure 8.6 and Figure 8.7, the gradient of this fitted trend

line is almost a third of the other two angle of attack cases. It was reasoned that the divergence of the rolling moment coefficients would occur for a lower positive aileron deflection the higher the angle of attack. The rolling moment coefficients between -10° and 0° deflection are consistent with those for the lower angles of attack and it is only for the positive deflections that large differences are noticed. To illustrate this, the trend line for the 15° angle of attack case was fitted to the rolling moment coefficients for the 20° case. This is shown in Figure 8.10. Based on this it was reasoned that instead of the gradient of the rolling moment coefficients over the $\pm 10^\circ$ deflection range being altered, as is indicated in Figure 8.9 (a), that the coefficients diverged from the trend line for positive aileron deflections within the $\pm 10^\circ$ deflection range. This is in line with the understanding of the divergence of the data seen in Figure 8.7 for the 15° angle of attack case; the upstream and downstream separation of the airflow from the surface of the aileron occurring at a lower deflection, in this case approximately 0° , as the angle of attack was increased to 20° .

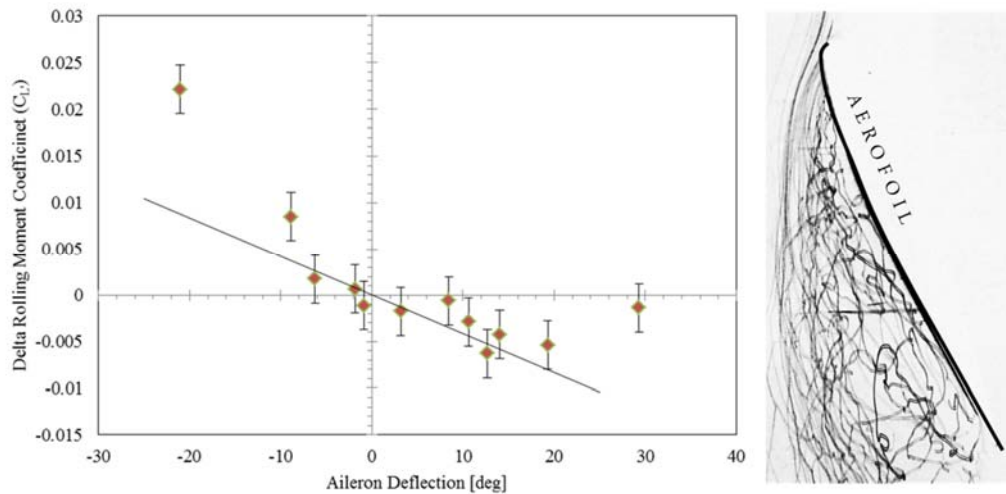


Figure 8.9: Rolling moment coefficient trend (a) and corresponding flow field (b) for 20° AoA, Thickness 2, $V=14.8\text{m/s}$

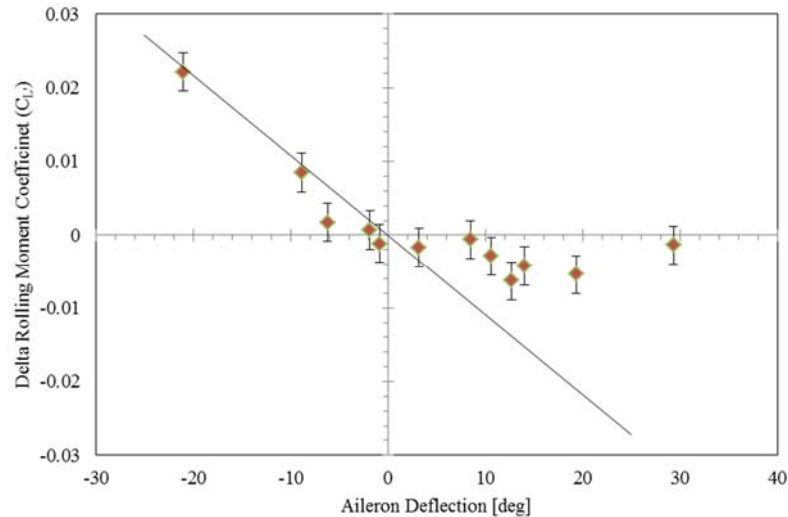


Figure 8.10: Rolling moment coefficients with modified trend line for 20° AoA, Thickness 2, $V=14.8\text{m/s}$

Comparisons were also made between the flow visualization in Figure 8.8 and the hinge moment coefficient trend, shown in Figure 8.11. The focus of these comparisons was the high aileron deflections. It was noted in Figure 8.11 that the hinge moment coefficients at the high aileron deflections, above 15°, were asymmetric about the zero deflection data point. The increase in hinge moment coefficient for a positive aileron deflection of 18° was 0.19 while for a negative deflection of 19.5° the hinge moment coefficient changed by 0.27. The uncertainty in the coefficients at an angle of attack of 12.5° was 0.02. For lower aileron deflections, such as the data points at $\pm 7^\circ$, the hinge moment coefficients are more symmetrical differing in magnitude by approximately 0.01.

The aileron was seen, as shown in Figure 8.8, to be experiencing different flow fields depending on whether it was at a high positive or high negative deflection. For the +30° deflection (Figure 8.8 (b)) the airflow is stalled on both sides of the aileron with the aileron being deflected into stalled airflow. For the -30° deflection, on the other hand, the airflow is only stalled on the upper surface of the aileron. It would therefore be expected that there would be a difference in the magnitude of aileron hinge moments for equal but opposite deflections; the aileron experiencing a lower hinge moment when deflected into the stalled airflow. Referring to Figure 8.11, at +30° deflection the hinge moment coefficient was approximately -0.3. While at -30° deflection, the hinge moment coefficient magnitude was double that, at approximately 0.6. The aileron was thus seen to experience a lower change in hinge moments when deflected into stalled airflow, as was expected.

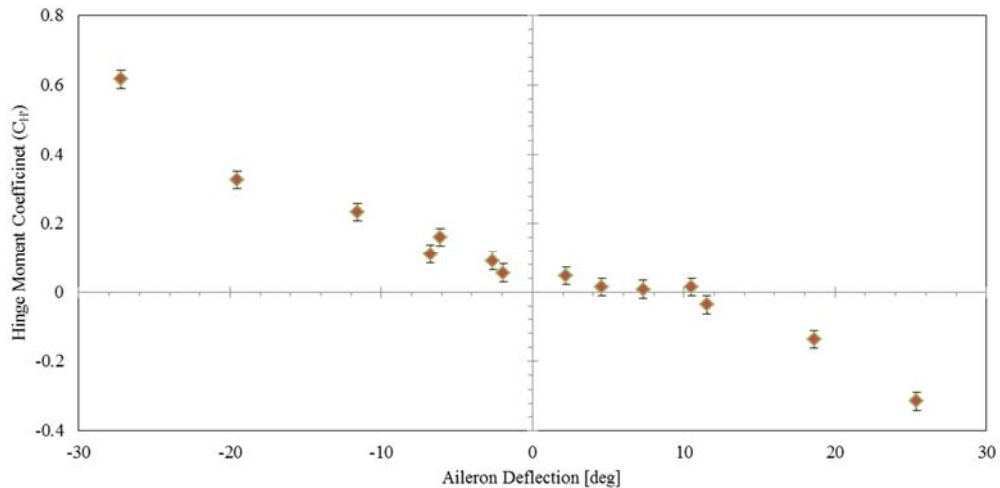


Figure 8.11: Hinge Moment Coefficients for a NACA 0012 at 12.5° AoA, plain sealed 0.206c 0.4b/2 aileron Thickness 2, V=14.6m/s

The trends in the rolling and hinge moment coefficients have been shown to correlate with the observed flow fields imaged during flow visualization. These observed flow fields and the corresponding trends in the data were predictable and consistent, indicating that the wing and aileron behaved correctly in the wind tunnel. The correlations of the flow visualization phenomenon to the trends of the moment coefficients were then taken as an indication that the measurement system had no significant flaws.

8.3 Comparisons to Previous Research

Further validation of the test results was done through the comparison of the test data to that obtained in previous research. The rolling, yawing and hinge moment coefficients would all be compared against those previously obtained by Rogallo (1941). His data was chosen primarily because the analysis technique used in the calculation of the rolling and yawing moment coefficient data was adopted from his work. Hinge moment coefficients were calculated in a manner more common to other research. However the use of the previous research, by Rogallo (1941), ensured that a more detailed validation could be made; the three aerodynamic moment coefficients all being from the same test data.

Data used in the comparisons to this research is that for aileron Thickness 2. This aileron was used as it most closely resembled the aileron used by Rogallo (1941). The data used in the comparison was taken from the tests conducted at 10° angle of attack and a wind tunnel speed of 14.5m/s. The coordinate system used in the previous research was reversed so that it reflected that used in the current research.

In order to ensure a greater similarity between the two data sets the dimension ratios of the ailerons being investigated were designed, from the outset, to be similar. Both ailerons had a 20% chord relative to the wing. The span used in the previous tests was 37% that of the wing semi-span while the current tests made use of an aileron with a 40% span relative to the wing.

40% was a more common span and this allowed for further comparisons were it to be necessary. The differences in the span between the two ailerons were seen as having a negligible effect on the performance of the aileron.

The Reynolds numbers at which the previous tests were conducted were higher than that which the wind tunnel was capable of producing. Rogallo (1941) operated at a Reynolds number of 1.2×10^6 , compared to current set of tests which were conducted at a Reynolds number of 0.33×10^6 . A further difference was that the previous research made use of a cambered NACA 23012 wing profile as opposed to the NACA 0012 wing used in the current set of tests. The effect of the differing Reynolds numbers and aerofoil profiles on the data is discussed further on in this chapter.

Rolling Moment Coefficients

The comparison of rolling moment coefficients is shown in Figure 8.12. As was discussed in the previous chapter the trend of the rolling moment data was seen to be linear over the $\pm 10^\circ$ aileron deflection range, with the data diverging from the linear trend at higher deflections. This linear trend for small aileron deflections would be expected, at least until the separation of the airflow from the surface of the wing and aileron. Evaluation of previous research, such as that of Rogallo's (1941) shown in Figure 8.12 and Figure A.1, typically has the trend of the rolling moment coefficients plotted as a 2nd or 3rd order polynomial. Fitting these sorts of trend lines was found to obscure the test results; especially at the higher angles of attack where the stalled airflow over the wing and aileron would increase the scatter in the data. Linear trend lines were thus used in all evaluations of the rolling moments coefficients as they were in Figure 8.12. These trend lines being fitted over the aileron deflection range of $\pm 10^\circ$.

The rolling moment coefficient from both data sets can be seen to be of relatively similar values. Considering the uncertainty in the data points, the differences between the rolling moment coefficients, of the two data sets, for low aileron deflections are relatively small. The general trend of the two data sets is also relatively similar to one another at both the high and low aileron deflections. This was taken as an indication that there were no major issues with the external balance's ability to measure rolling moments.

It can be seen, from Figure 8.12, that the linear trend line fitted to the current data has a lower gradient than that for Rogallo's work (1941). A lower gradient implies that the aileron in the current tests was less effective, producing a lower relative rolling moment coefficient for a given deflection. This difference was attributed to the different aerofoil profiles used between the two tests. The cambered NACA 23012, used in the previous research, has a higher lift curve gradient and, as it was understood, a corresponding higher rolling moment gradient. Taking this into account in the comparison of the two tests, it can be seen that the data sets both correlate nicely with the linear trend line over the $\pm 10^\circ$ deflection range. This was taken as a further indication of the validity of the rolling moment measured by the external balance; the wing behaving similarly over this range.

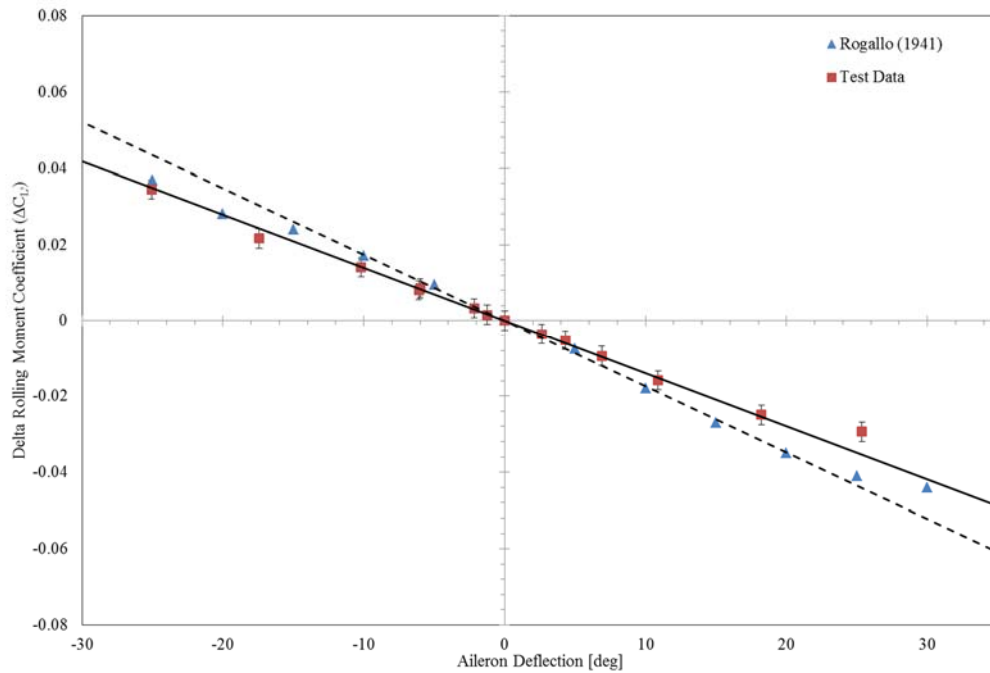


Figure 8.12: Comparison between delta rolling moment coefficients for primary test data, Thickness 2, 10° AoA, V=14.7m/s, and data obtained from Rogallo (1941).

Jacobs (1937) researched the effect of Reynolds number on the performance of NACA aerofoils. His results showed that different Reynolds numbers affected the maximum coefficient of lift and data trend of the lift coefficients at high angles of attack; this resulting in the wing stalling at lower angles of attack for lower Reynolds numbers. With reference to Figure 2.8, it was seen that the gradient of the linear portion of the lift coefficients is unaffected by increased or decreased Reynolds numbers, at least at the Reynolds numbers for which the previous research and the current tests were performed. It was thus understood that a similar effect would be noted for the rolling moment coefficients. In this way the differing Reynolds number would have no discernable effect on the rolling moment coefficients in the aileron deflection range of $\pm 10^\circ$. In this range the rolling moment coefficients have been seen to respond linearly. This holds provided the angle of attack was not so high as to have the airflow stalled over the surface of the wing. Considering the differing aerofoil profiles, the wings performed similarly over the linear deflection range.

As was discussed in the previous chapter, the airflow only began stalling over the surface of the wing at angles of attack around 12.5° . The tests being compared in Figure 8.12 were conducted at lower angles of attack and it was assumed that the airflow was still attached to the upper surface of the wing. Figure 8.8 showed that the airflow over the aileron would stall at high aileron deflections even if the wing is not yet stalled. Differences between the two data sets being compared would then be expected at the higher aileron deflections; the airflow stalling over the surface of the aileron for lower deflections at lower Reynolds numbers. Referring to

Figure 8.12, this difference is clear for the positive aileron deflections. The rolling moment coefficients of the current data begin to diverge above 10° deflection. The rolling moment coefficients of Rogallo's data (1941) only began to diverge above 20° . This is in line with the understanding of Jacob's research (1937).

For the negative aileron deflections the differences between the two data sets are not as distinct. Rogallo's data (1941) deviates far more from the linear trend, at the high negative deflections, than the current data set. This deviation was attributed, in the previous chapter, to the separation of the airflow over the surface of the aileron. A small deviation of the rolling moment coefficients, of the current data, is noted at approximately -17° deflection. This deviation is barely more than the uncertainty in the rolling moment coefficients at 10° angle of attack. The data point at the next, higher, negative deflection coincides once again coincident with the linear trend plotted. The deviation of previous data at -20° deflection, from the linear trend, was noted to have not changed from the previous data point. Despite this the rolling moment coefficients for previous data at the high negative aileron deflections are still greater than those from the current tests. This once again agrees with the research by Jacobs (1937). The exact reason as to why the rolling moment coefficients do not deviate as much from the linear trend as those from Rogallo's data (1941), at high negative aileron deflections, is not quite understood. It is assumed that the differences are due to the differing Reynolds numbers and associated turbulence intensities. As a precaution to be taken in the further analysis of the rolling moment coefficients, little emphasis will be placed for the data obtained at high negative aileron deflections.

Yawing Moment Coefficient

The comparison of the yawing moment coefficients between the current tests and the previous research data from Rogallo (1941) is shown in Figure 8.13. The general trends of both data sets can be seen to be relatively similar to one another. The main difference between the two data sets was the aileron deflection for which the minimum yawing moment would occur. For the current data set this occurs at approximately 9° deflection while in the previous data this occurs at 18° . This is due to the fact that aerofoil profile used in the current tests was symmetrical while the wing, used in the previous research, was cambered. The minimum drag coefficient for a symmetrical wing occurs at 0° angle of attack. For a cambered aerofoil the angle of attack is above 0° . In the same way it would be expected that the minimum yawing moment coefficient, due to an aileron deflection, for a cambered aerofoil would be higher than that for a symmetrical aerofoil. The differing aerofoil profiles were therefore seen as the primary reason for the different yawing moment coefficients between the two data sets.

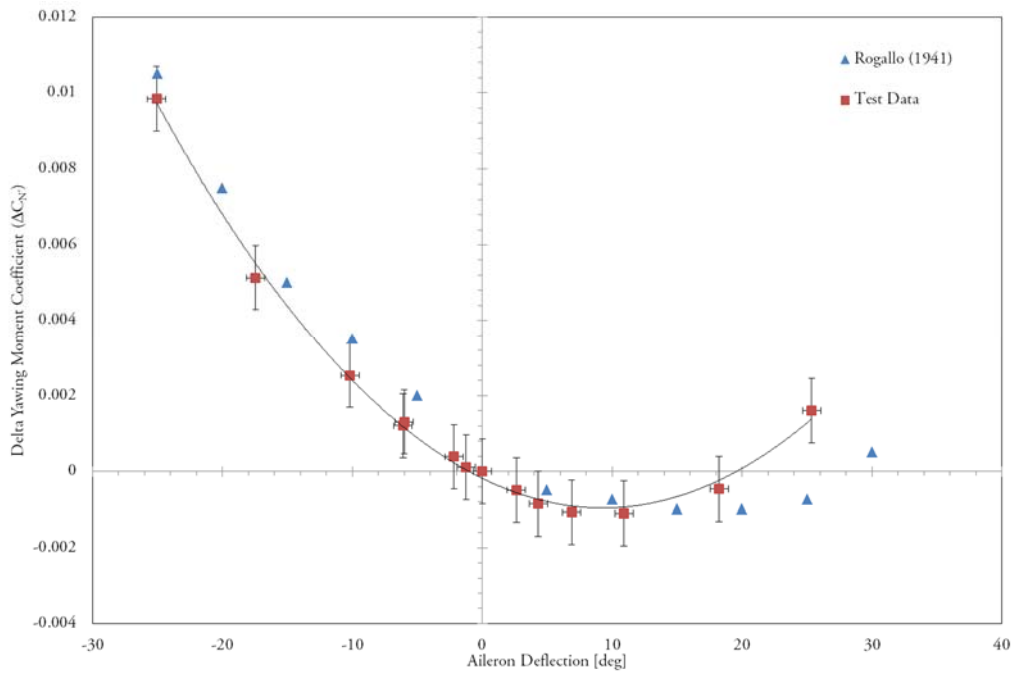


Figure 8.13: Comparison between delta yawing moment coefficients for primary test data, Thickness 2, and data obtained from Rogallo (1941), 10° AoA, $V=14.7\text{m/s}$.

Jacobs (1937) research into the effect of Reynolds number on the performance of NACA aerofoils also dealt with the effect of Reynolds number on drag coefficients. As with the rolling moment coefficients it was assumed that the effect that Reynolds number had on the yawing moment coefficients would be similar to that for drag coefficients. Jacobs research (1937) indicated that the difference in drag coefficients between tests conducted at Reynolds numbers of 0.3×10^6 and 1.4×10^6 were relatively small, the differences only being apparent with the onset of stall. As was discussed, at 10° angle of attack the wings in both tests were not stalled. It would therefore be expected that little discernable difference in magnitudes would be noted. This is confirmed through comparison to the data in Figure 8.13. Once again this was taken as indications as to the validity of the measurement of the yawing moments by the external balance.

Hinge Moment Coefficient

The comparison of the hinge moment coefficients between the current test data and that obtained by Rogallo (1941), is shown in Figure 8.14. As with the rolling moment coefficients, the hinge moment coefficients were seen to behave linearly over the $\pm 10^\circ$ aileron deflection range. These observations were based off previous research such as that by Rogallo (1941), shown in Figure A.1, as well as preliminary observations of the current test data. This linear trend for small aileron deflections would be expected, at least until the separation of the airflow from the surface of the wing and aileron. Evaluation of the data in Figure A.1 has the coefficients plotted as a 3rd order polynomial. A similar convention is followed in other previous research papers such as that by Wenzinger (1931) and Noyes (1932). As with the rolling moment coefficients, fitting these sorts of trend lines to the hinge moment coefficients

was found to obscure the test results; this being especially pertinent at the higher angles of attack where the stalled airflow over the wing and aileron would increase the scatter in the data. Linear trend lines were thus used in all evaluations of the hinge moments coefficients as they were in Figure 8.14. These trend lines were fitted over the aileron deflection range of $\pm 10^\circ$.

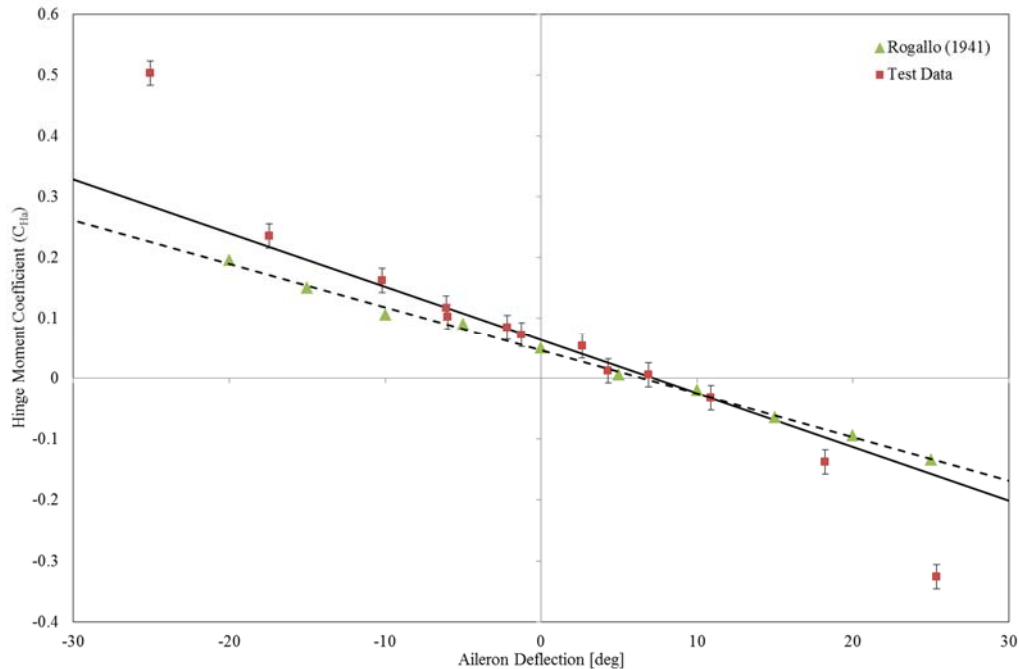


Figure 8.14: Comparison between hinge moment coefficients for primary test data, Thickness 2, and data obtained from Rogallo (1941), 10° AoA, $V=14.7\text{m/s}$.

Comparison of the two data sets in Figure 8.14 shows that over the $\pm 10^\circ$ deflection range the hinge moment coefficients are of similar values. Considering the uncertainty in the current data set and differences in Reynolds number and aerofoil profiles, the differences to previous data are quite small. This was taken as an indication that the hinge moment balance was, at least over the linear operating range of the aileron, capable of measuring the hinge moments with a satisfactory level of accuracy.

The gradients of the trend lines fitted to the two data sets are different with gradient of the previous data being lower than the current test data. This is the opposite of the compared gradients for the rolling moment coefficients, shown in Figure 8.12. Once again considering the uncertainty in the test data, 0.021 at 10° angle of attack, the differences in the gradients could be negligible. Over the deflection range of $\pm 10^\circ$ and at an angle of attack of 10° it would be expected that the airflow would not be stalled over the wing or the aileron. The effects of the differing Reynolds number, between the two data sets, on the lift and drag coefficients has been understood to be negligible over the linear operating range of the wing and aileron. Differences then between the current test data and that of Rogallo's (1941) would then be small as would the gradients of the fitted trend lines. A small difference would be expected because of the different aerofoil profiles used as these would alter the way the airflow acts on the ailerons.

Based on the calculated uncertainties, however, this difference cannot be commented on accurately.

Due to the differing magnitudes in the two data sets, the overall trend of the hinge moment coefficients from the previous research, by Rogallo (1941), is not that clear. Compared to the overall trend in the current data, seen in Figure 8.12, and the typical hinge moment trend in Figure A.2, the overall trend of the hinge moment coefficients from the previous research, seen in Figure A.1, is relatively similar. It was thus understood that the apparent differences in the trends between the two data sets, presented in Figure 8.12, were not because of a fault in the hinge moment balance but rather aerodynamic differences that are most likely attributable to the different Reynolds numbers.

Above the $\pm 10^\circ$ deflection range the two data sets diverge quickly with large differences in the data noted at the higher aileron deflections. It has already been discussed that at the high aileron deflections the airflow is stalled over the surface of the aileron. The separation of the airflow from the surface of the aileron would be expected to non-linearly increase the drag acting on the aileron. This in turn would result in a non-linear increase in the hinge moment acting on the aileron. The larger the aileron deflection, the higher the degree of stall, the higher the drag acting on the aileron and subsequently the higher the aileron hinge moment. The data published by Jacobs (1937) showed that for stall conditions the drag force acting on a surface at a lower Reynolds numbers would be higher than on a surface at a higher Reynolds number. Based on the large difference in Reynolds number that the current tests and Rogallo's data (1941) was obtained at, it would be expected that larger differences in drag forces would be noted. This would explain the high differences noted in Figure 8.12 at high aileron deflections.

Further interpretation of the hinge moment data would need to consider the effect of the lower Reynolds numbers. The trend of the hinge moment coefficients at high aileron deflections is exaggerated compared to existing published data. It would be expected that small differences in hinge moment coefficients, brought on by the different aileron trailing edge thicknesses, may appear larger than they would be for a test conducted at higher Reynolds numbers.

Based on the comparisons made above, the measurement system is considered to be reliable. Conclusions as to the effects of different aileron trailing edge thicknesses, within the mentioned limitations, can then be confidently made.

8.4 Variation of Aileron Trailing Edge Thickness

This chapter evaluates the effect of varying the aileron trailing edge thickness. Due to similarities in the data for various angles of attack only selected data sets are presented here. The full list of results can be found in Appendix I.

So as to avoid clutter in the Figures of this chapter, the uncertainty values for only one of the four aileron data sets is plotted for each of the Figures. This is also the case for the Figures in Appendix I. The differences between the uncertainty values for the four ailerons tested were

noted as being, on average, the same within the resolution of the DAQ. In order to be conservative, if there was a larger difference, the highest uncertainty values between the four data sets were used. The uncertainty values shown for Aileron Thickness 2 can therefore be assumed to be the same for the other three ailerons tested

Previous research has been done into the effects of thicker trailing edges by the likes of Hoerner (1950) and Baker (2008). The effects, discussed, were with reference to wing aerodynamic characteristics rather than aileron performance. It was, however, noted by Hoerner (1985) that the noted effects would possibly apply to ailerons as well. The effects of an increased trailing edge thickness included an increase in the lift curve slope and maximum lift coefficient. Applied to aileron performance, it would be expected that this would result in a similar increase in the rolling moment slope, over the linear range, and a delayed divergence of the moment data from the linear trend.

Coinciding with the increase in lift coefficients was the increase in drag coefficients for wings with thicker trailing edges (Hoerner & Borst, 1985). As with the rolling moment coefficients, it was understood that an increase in the drag coefficients would imply an increase in the yawing moment coefficients measured as well. The increase in the trailing edge thickness of the aileron would therefore be expected to result in an increase of the yawing moments coefficients.

Typically the C_L/C_D values remained constant for blunt trailing edges with little advantage noted compared to sharp trailing edges. A small increase was seen to occur when the trailing edge thickness to chord ratio was increased to approximately 0.5% (Hoener, 1950). The aileron trailing edge thickness to wing-chord ratios that were tested were 0.39%, 0.71%, 0.96% and 1.22%. It would therefore be expected that in a comparison between the rolling and yawing moment coefficients an optimal thickness could be identified.

Rolling Moment Coefficient

Figure 8.15 shows the rolling moment coefficients for each aileron tested at 5° angle of attack. The trend line, seen in the plot, is fitted to aileron Thickness 2 data in order to aid in the comparison of the four data sets. Considering the uncertainty in the data, the differing trailing edge thicknesses can be seen to result in no discernable effect on the rolling moment coefficients. All four data sets behave in a similar manner, being linear over the $\pm 10^\circ$ aileron deflection range and diverging from the linear trend at a high positive aileron deflection. The expected change in the rolling moment coefficients, being the change in the slope over the linear range and delayed divergence of the data from the linear trend is not evidently clear. A small difference between the data of Thickness 4 and Thickness 2 can be seen at 25° deflection. This difference could indicate a small delay in the onset of the data divergence for the thicker trailing edged aileron, Thickness 4. The difference is, however, just within the uncertainty error bars of the two data sets and as such the difference could in fact be negligible. The noted increase in the scatter of the data, at this deflection, due to the airflow over the aileron being stalled, would also account for the noted differences.

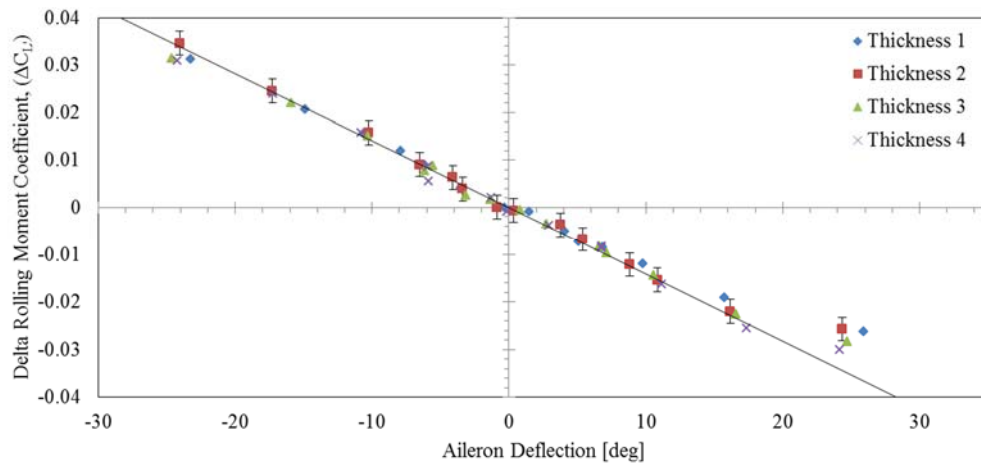


Figure 8.15: Comparison of delta rolling moment coefficients for 4 aileron trailing edge thicknesses, 5° AoA, V=14.6m/s

Evaluation of the other angles of attack tested showed that a similar results as to that for the 5° angle of attack case. To illustrate this, the data sets for the four ailerons, over three angles of attack were plotted on the same axis, as shown in Figure 8.16. The three angles of attack, 5°, 12.5° and 15°, represented the expected linear operating range of the wing, the pre-stall and finally stalled condition of the wing. The linear trend line was fitted to data of Thickness 2 at 5°, over the ±10° deflection range, to aid in the comparison of the data. As was shown previously, in chapter 8.2, the trend of the data over this range would change slightly as the angle of attack increased. This accounts, in part, for the increased scatter in the data. The airflow being stalled at 15° angle of attack further accounts for the increase in scatter, seen in Figure 8.16; the occurrence of stalling having already been shown previously to increase the scatter of the data.

The main purpose of data presented in Figure 8.16 is to illustrate that for angles of attack from 0° to 15° the differences due to differing trailing edge thicknesses of the ailerons were, within the uncertainty of the data points, negligible. Over this angle of attack range there were no discernable differences in the gradients over the linear operating range and the divergence of the data from the linear trend, at high deflections, was not offset as expected; these differences being expected when increasing the trailing edge thickness.

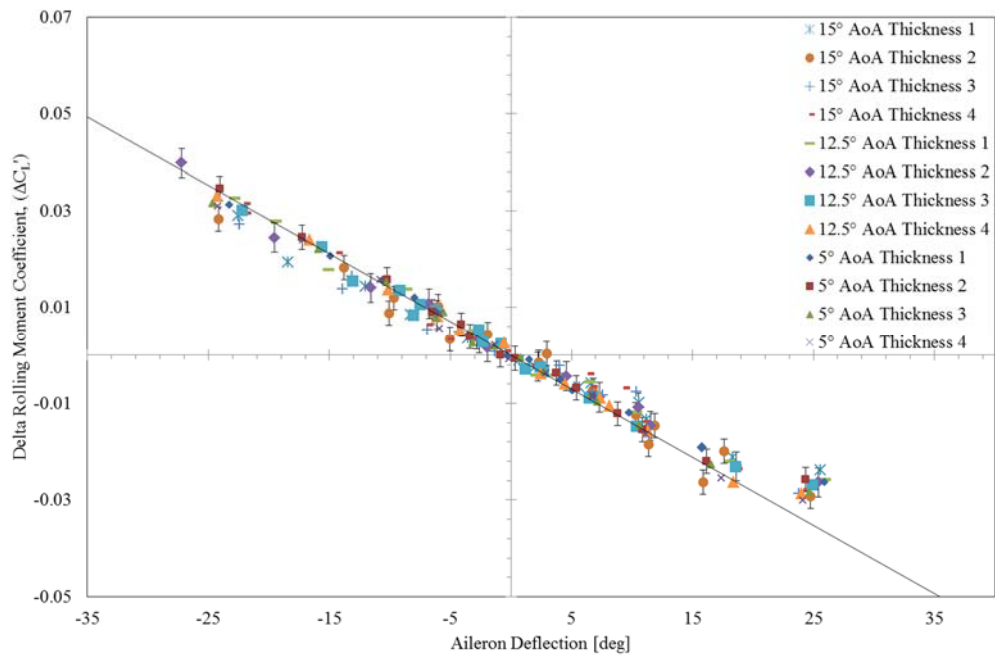


Figure 8.16: Comparison of delta rolling moment coefficients for 4 aileron trailing edge thicknesses, 5°, 12.5° and 15° AoA, $V=14.6\text{m/s}$

This was seen as important as this angle of attack range is generally not exceeded by general aviation aircraft. For the typical flight envelope of these aircraft, the increase in the trailing edge thickness of the aileron does not have a noticeable effect on the rolling moment, according to the test data.

The rolling moment coefficient trends, for each aileron, with the wing at 20° angle of attack is shown in Figure 8.17. At this angle of attack the wing is in deep stall condition, as discussed in chapter 8.2. Although general aviation aircraft do not intentionally operate at such high angles of attack it was investigated so as to ascertain if any differences did exist and their implication on the aircraft performance. One factor considered was the possible effect of differing trailing edge thicknesses on the wing tip stalling characteristics. If a drastic change in the rolling moment coefficients was noted it could potentially speak to either a favourable or unfavourable effect on the wing tip stall characteristics. During testing, with the wing in a deep stall, the scatter and uncertainty in the data points was noted to increase. Considering these increased values, there is no discernible difference seen in Figure 8.17 between the ailerons of different trailing edge thicknesses; the trend of the data points all being similar. Any effects, positive or negative, brought on by the thickening of the aileron trailing edge with the wing in a deep stall cannot then be detected. This was not an unexpected result, especially considering the negligible effect of differing trailing edge thicknesses at lower angles of attack.

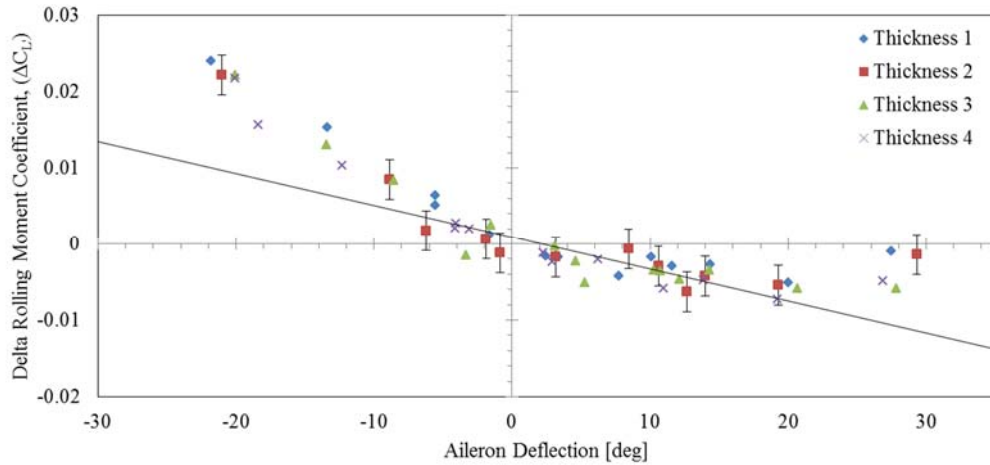


Figure 8.17: Comparison of delta rolling moment coefficients for 4 aileron trailing edge thicknesses, 20° AoA, $V=14.8\text{m/s}$

Yawing Moment Coefficient

The effect of thickened aileron trailing edge thicknesses was found to have little effect on yawing moment coefficients for angles of attack from 0° to 15° ; as was the case for the rolling moment coefficients. The yawing moment coefficients changed as the angle of attack was increased, as shown in Figure 8.18. This was an expected result however it meant that the noted similarity in the yawing moment coefficients, for the four aileron sets over this angle of attack range, could not be as clearly shown as was done for the rolling moment coefficients in Figure 8.16. The data for 5° and 15° is presented instead. These two angle of attacks representing the linear range and stalled cases for the wing as discussed in chapter 8.2. The yawing moment coefficients for 0° angle of attack were not chosen as they did not represent as large a deflection range as the 5° angle of attack case.

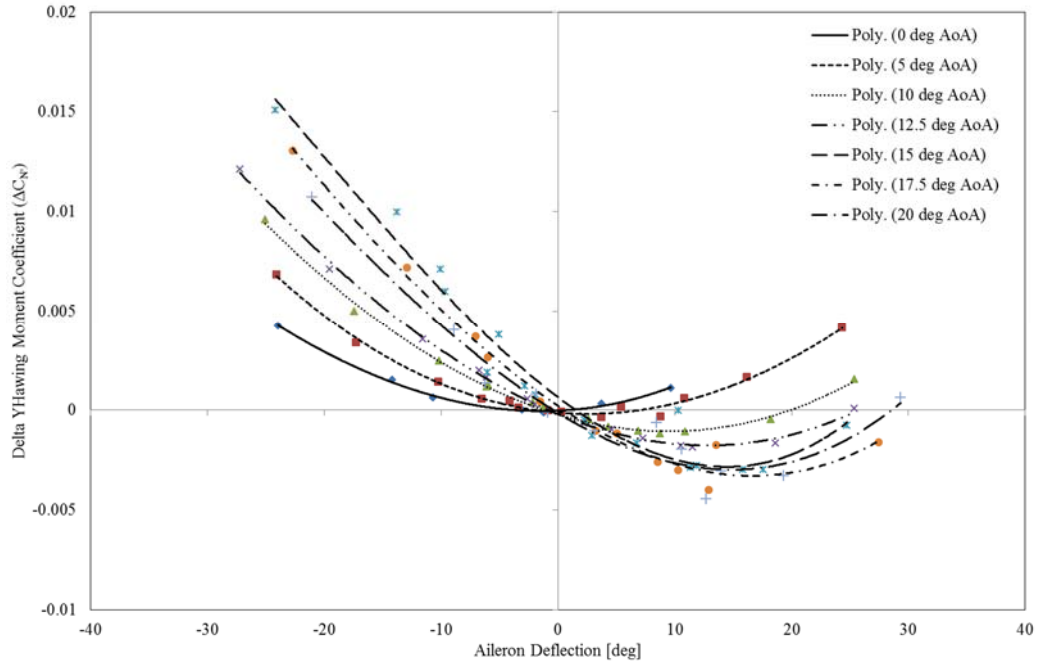


Figure 8.18: Delta yawing moment coefficient trends for each AoA, aileron Thickness 2, $V=14.8\text{m/s}$

For the 5° angle of attack case, the differences in the data points for the four ailerons tested are all within the measured uncertainty. As such there is no discernible effect on the yawing moments as a result of thicker aileron trailing edges. The trends of the four data sets are all similar and there was no change in the position at which the minimum yawing moment occurs. The expected increases in the yawing moments, due to thicker trailing edges, are also not clear, even at high aileron deflections. A similar result can be seen, in Figure 8.20, for the deflection range of $\pm 10^\circ$, for the wing at 15° angle of attack.

The increased scatter in the data points is attributed, as discussed in chapter 8.2, to the airflow over the wing being stalled at this angle of attack. There is a slight difference between the yawing moment coefficients for Thickness 2 and the other three ailerons that was noted for high negative deflections of the aileron; the largest difference being between Thickness 2 and Thickness 3. These differences are small enough to be considered negligible in comparison to the uncertainty in the data. Hoerner (1985), however, noted an effect on the aerodynamic coefficients to occur for a trailing edge thickness to wing chord ratio of 0.5%. This pertained to the variance in the C_L/C_D ratio, which was understood as similarly affecting the C_L/C_N ratio. The apparent lack of change in rolling moment coefficients due to changing trailing edge thicknesses, however, lead to the assumption that a change in the yawing moment coefficients would be measured. The thickness ratio of 0.5% is in between those for aileron Thickness 1 and Thickness 2 and a difference between the data points, as see in Figure 8.20, could then be possible.

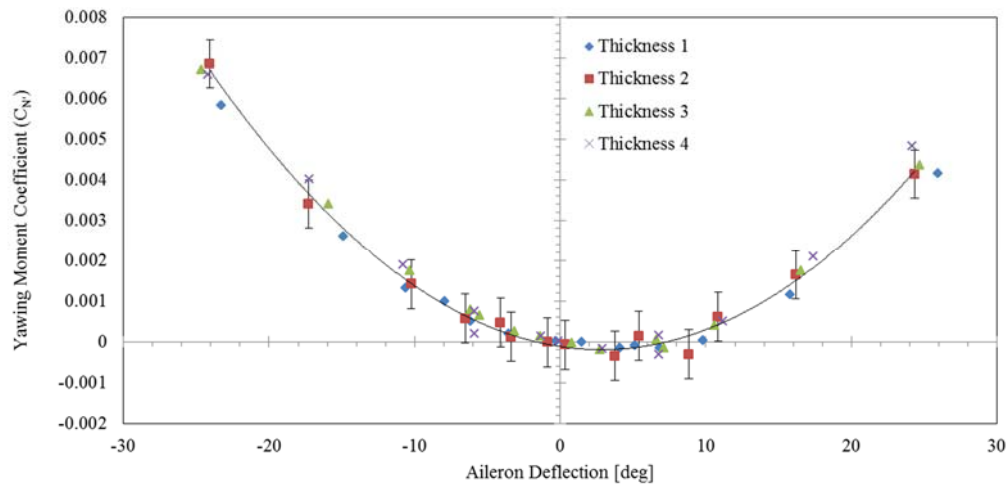


Figure 8.19: Comparison of delta yawing moment coefficients for 4 aileron trailing edge thicknesses, 5° AoA, V=14.6m/s

Upon evaluating the data trends at an angle of attack of 20°, shown in Figure 8.21, there is once again a difference in the data sets. This time, however the differences occur over the positive aileron deflection range. Over the negative deflection range there are once again no discernible differences between the data from the four ailerons, even at high deflections. Data obtained from Thickness 1 and 4 are no longer discernibly different from the yawing moment coefficients of Thickness 2. There is still a difference between aileron Thickness 2 and 3 at a high positive deflection of the aileron. Furthermore the deflection at which the minimum yawing moment coefficient occurs appears to be skewed for Thickness 3 when compared to the other ailerons.

The differences between the yawing moment coefficients of the aileron sets were expected and appear to occur at both 15° and 20° angle of attack. These differences are, however, distinctly different. If Thickness 2 resulted in a higher yawing moment coefficient at a high negative deflection, compared to the other ailerons, it would also be expected that a similar result would be seen when testing at 20° angle of attack. Similarly the shift if the deflection at which the minimum yawing coefficient occurs for Thickness 3, at 20° angle of attack, should be detectable at 15° angle of attack. The wing is, in both angle of attack cases, fully stalled. The wing simply being in a deeper stall condition at 20° than at 15° angle of attack. The nature of the airflow over the aileron at these angles of attack should not be discernibly different enough to result in the changes observed between 15° and 20°. This is even further confirmed by referring to Figure I. 20 where differences between the aileron data sets mirror neither those in Figure 8.20 or Figure 8.21. It was thus concluded that the differences noted in the data points were not an indication of the trailing edge thickness of the aileron affecting the yawing moment coefficients but rather a result of the scatter in the data due to the wing being stalled and the resolution of the yawing moment loadcell.

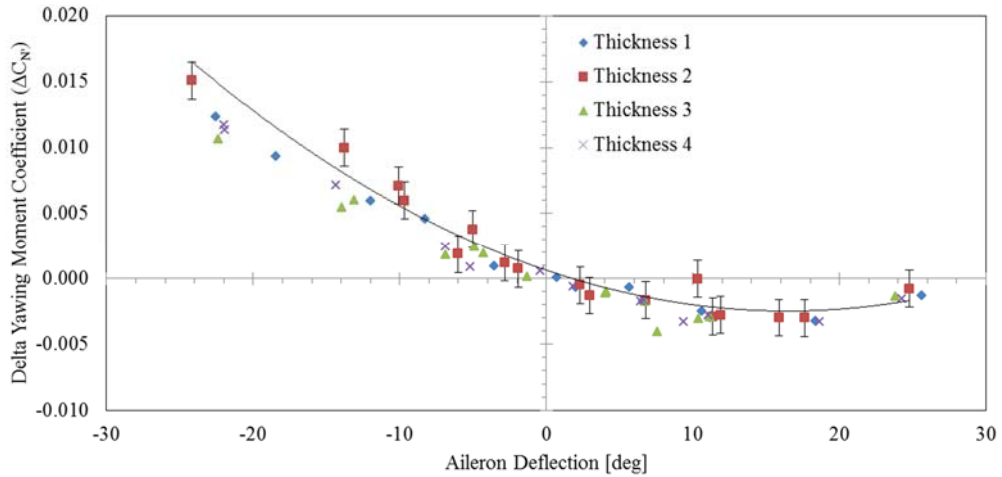


Figure 8.20: Comparison of delta yawing moment coefficients for 4 aileron trailing edge thicknesses, 15° AoA, V=14.5m/s

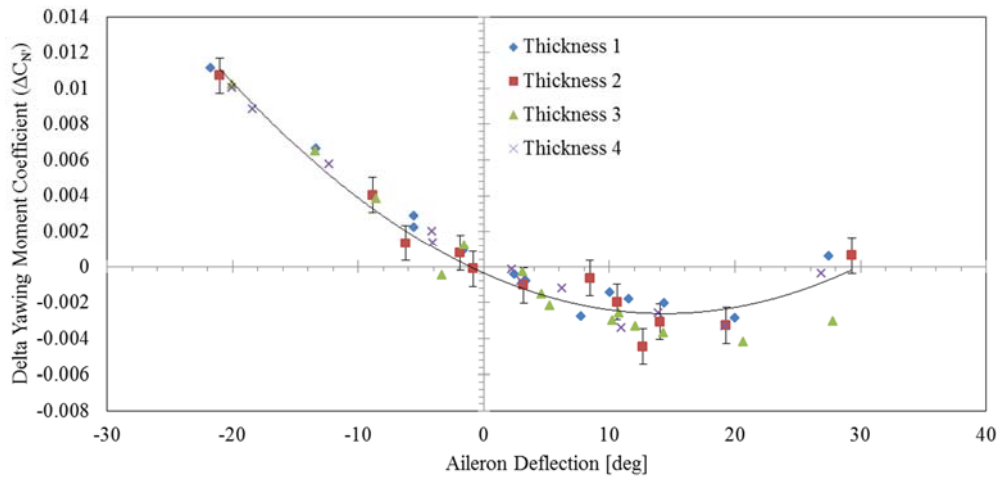


Figure 8.21: Comparison of delta yawing moment coefficients for 4 aileron trailing edge thicknesses, 20° AoA, V=14.8m/s

With no discernible differences in the yawing and rolling moment coefficients, due to the change in aileron trailing edge thicknesses, the direct comparison of the two coefficients was investigated. This was done so as to ascertain as to whether the critical 0.5% thickness ratio, as noted by Hoerner (1950), had any effect on the two moment coefficients that was not noticed previously. This was done for both the 5° and 20° angle of attack cases, shown in Figure 8.22 and Figure 8.23 respectively. It was seen that for all four ailerons tested, the differences to the trends and magnitudes of the data points, due to the differing trailing edge thicknesses, are indiscernible. Based on the fact that thicker trailing edges had no discernible effect on either the rolling or yawing moment coefficients this result is not unexpected. It was thus concluded that the small differences noted by Hoerner (1985) due to thicker trailing edges, are not applicable to the rolling and yawing moment coefficients as was originally expected.

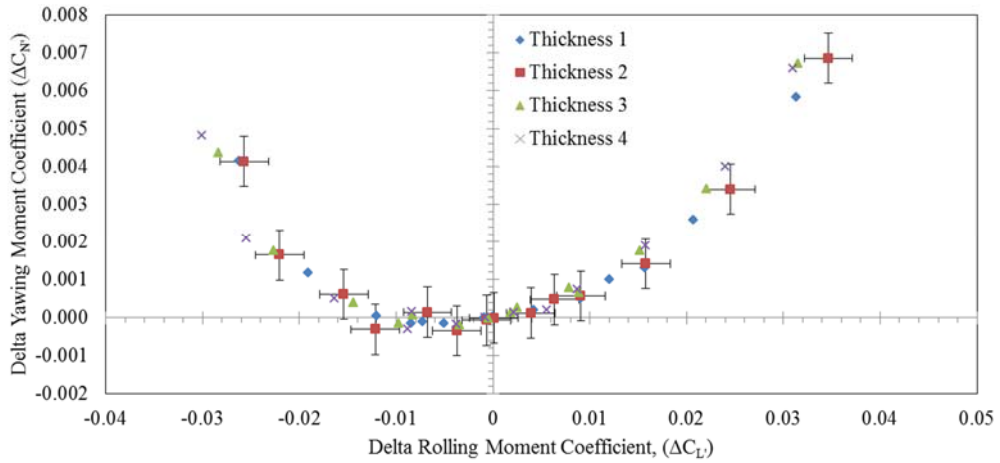


Figure 8.22: Comparison of delta yawing moment coefficient variation with delta rolling moment coefficient, for 4 aileron trailing edge thicknesses, 5° AoA, V=14.6m/s

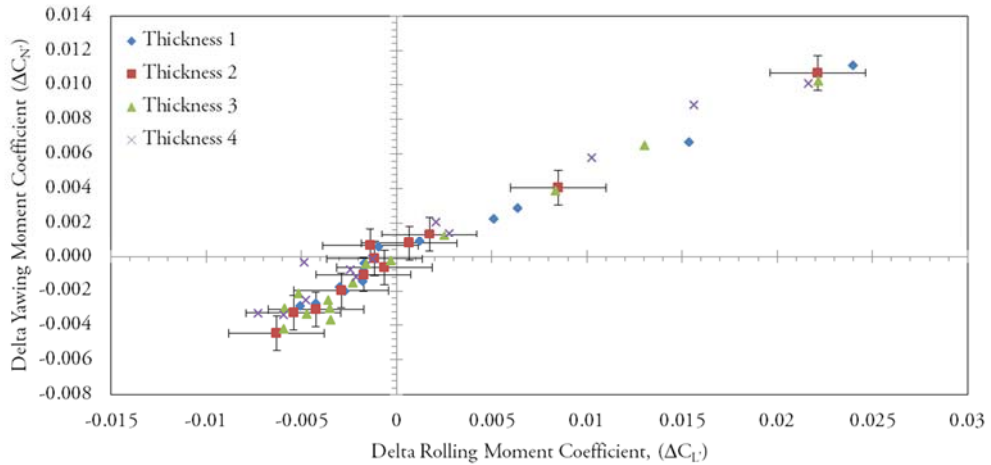


Figure 8.23: Comparison of delta yawing moment coefficient variation with delta rolling moment coefficient, for 4 aileron trailing edge thicknesses, 20° AoA, V=14.8m/s

Hinge Moment Coefficient

The hinge moment coefficients for the four ailerons with the wing at 5° angle of attack is shown in Figure 8.24. For the most part all four data sets have similar values and trends; the coefficients behaving linearly over the $\pm 10^\circ$ range, with divergence from the linear trend occurring at similar aileron deflections. Considering the uncertainty in the coefficients, being 0.02 at 5° angle of attack, there were not any significant differences that the hinge moment balance could measure.

Similar results were noted for 0°, 10° and 12.5° angles of attack. This coincides with the similarity in the rolling and yawing moment coefficients for the four ailerons for the same angles of attack.

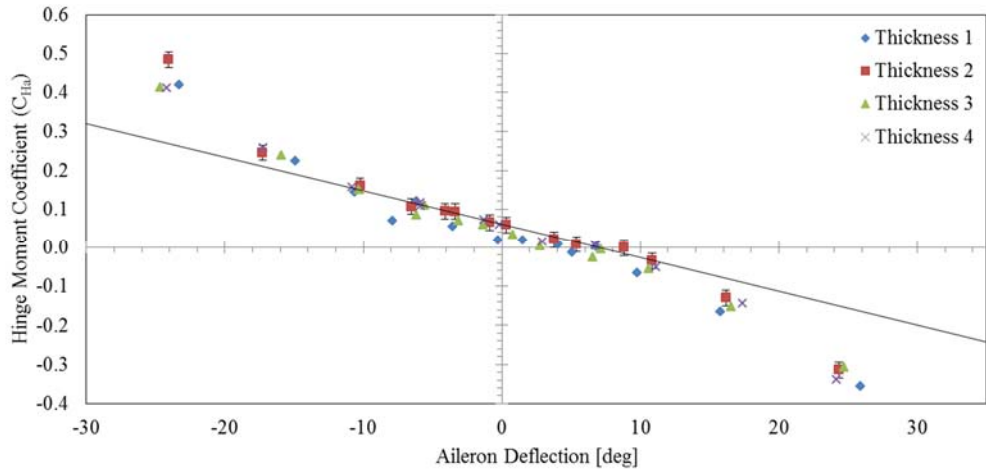


Figure 8.24: Comparison of hinge moment coefficients for 4 aileron trailing edge thicknesses, 5° AoA, V=14.6m/s

Evaluation of the hinge moment coefficients for the four ailerons at 15° and 20° angle of attack, shown in Figure 8.25 and Figure 8.26, indicated that the thicker trailing edges were having some effect on the hinge moment coefficients. Specifically the differences were between Thickness 1 and Thickness 4. Unlike previously noted differences for the rolling and yawing moment coefficients, the differences between aileron Thickness 1 and 4 are consistent over the two angles of attack in question. These differences are also larger than the calculated uncertainty of the respective data points. While the known increase in scatter, due to the stalled airflow, could account for the noted differences, the consistencies in the differences for the two angles of attack indicate another factor is at work.

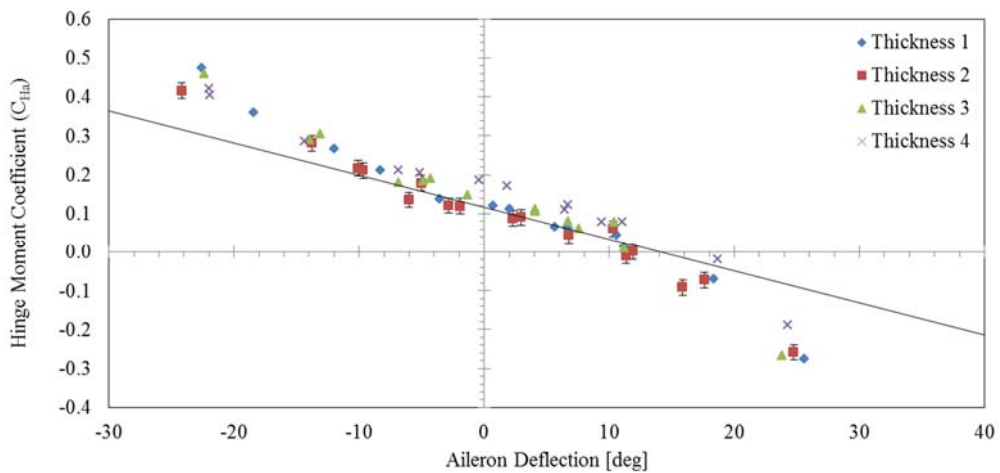


Figure 8.25: Comparison of hinge moment coefficients for 4 aileron trailing edge thicknesses, 15° AoA, V=14.5m/s

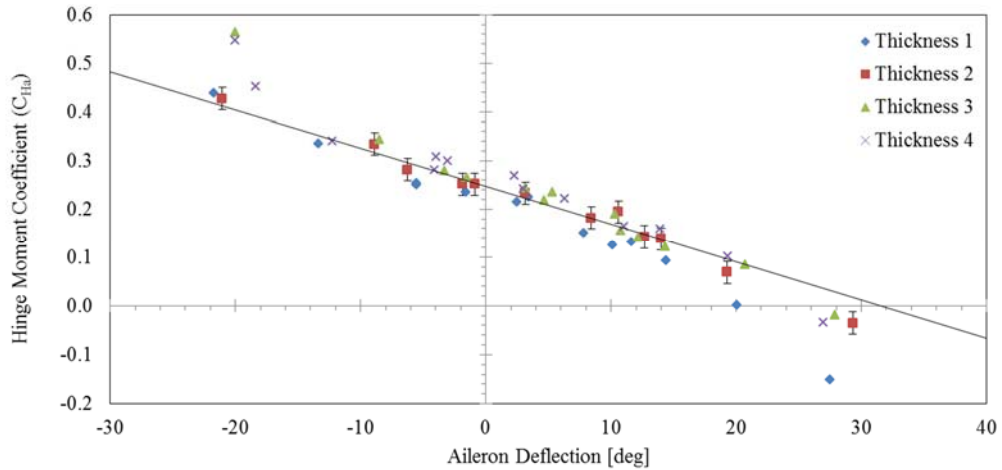


Figure 8.26: Comparison of hinge moment coefficients for 4 aileron trailing edge thicknesses, 20° AoA, V=14.8m/s

At 15° angle of attack the differences between aileron Thickness 1 and 4 occur primarily for the aileron deflection range of $\pm 10^\circ$. As the deflection then increases, the differences between the two data sets decrease until becoming indiscernible. At 20° angle of attack, the differences once again occur over the $\pm 10^\circ$ deflection range; however they do not decrease as the aileron is deflected further. The gradients of the two data sets are very similar. The differences are because of a shift in the hinge moment magnitude for the aileron at a zero deflection. This is unlike the rolling and yawing moment coefficients which all crossed the y-axis at approximately the same point. The hinge moments for Thickness 4 were then, despite having a similar gradient, higher than the hinge moments of Thickness 1.

These effects were attributed to the airflow leaving the trailing edge of the aileron. For an aileron at 0° angle of attack and 0° deflection, the change in the trailing edge thickness would change the angle at which the airflow departs the aileron trailing edge. This small change would become important at high angles of attack where the airflow on opposite sides of the wing, and hence aileron, would be different due to the onset of stall. These different airflow types are observed in Figure 8.8, where the effect of stalled airflow on the one side of the aileron and attached airflow on the other results in a different shape of the airstreams around the aileron. The change in trailing edge thickness and hence the change in angle at which the airflow leaves the aileron would then be expected to adjust the shape of the airstreams around the aileron trailing edge. This effect could not be clearly observed with the current flow visualization technique and as such can currently only be assumed to be correct.

The change in the shape of the airstreams would in theory adjust the aerodynamic loads applied to the aileron. It is thus assumed that this is the cause of the differences observed in Figure 8.25 and Figure 8.26.

This difference was attributed to the resulting bending of the streamlines flowing from the underside of the wing over the edge of the aileron. Due to the separated airflow over the upper surface of the wing, due to the angle of attack, the streamlines would be expected to bend upwards after leaving the trailing edge of the aileron. As the aileron trailing edge thickness was increased it would be expected that these streamlines would have to bend more in order to establish the same flow region in the trailing wake of the wing. This change would be indiscernible in the flow visualization. It would mean, however, that a higher hinge moment would be measured for a thicker trailing edge; the increased bending in the streamlines leaving the aileron trailing edge resulting in an increased force acting on the aileron.

The differences in the data, noted in Figure 8.25 and Figure 8.26, occur between the ailerons with the smallest and largest trailing edge thickness. The differences between the hinge moments as discussed above would be expected to have a critical trailing edge thickness for which they would occur. It was noted that for the 15° angle of attack case the hinge moments for Thickness 2 and 3 correlated better with those of Thickness 1 indicating that the critical thickness would be somewhere between Thickness 3 and 4. At 20°, however, the hinge moments for Thickness 2 and 3 appear to correlate better with those of Thickness 4, indicating now that the critical thickness would appear to be between Thickness 1 and 2.

These differences only become apparent at the high aileron deflections and high angles of attack. Considering the known increase in the scatter of the data at such deflections and angles of attack, the differences may ultimately be negligible. It should also be noted then that ailerons are not typically operated in this range and wings are not flown at these angles of attack. While the differences in the hinge moments brought on by the differing trailing edge thicknesses were notable they occur outside of the aircraft's typical flight envelope. It is therefore not necessary to consider these noted differences in the design of ailerons in the future.

Considering then the range of angles of attack for which general aviation aircraft typically operate, between 0° to 15°, there were no discernible effects to the rolling, yawing and hinge moments brought on by the changing of the trailing edge thickness. The usual philosophy of manufacturing sharp trailing edges for ailerons may therefore be unnecessary; the manufacture and implementation of ailerons with thicker trailing edges having no discernible effect on the rolling performance of the aileron, while potentially lowering the complexity and manufacture costs.

9 CONCLUSIONS

A compact hinge moment balance was designed, capable of measuring the hinge moment produced by an aileron. Unlike previous designs this balance could be housed inside the internal structure of the wind tunnel test model eliminating any intrusions into the airflow by tensioned cables. The test model was mounted to a basic external balance that allowed for the measurement of the rolling and yawing moments due to a deflection of the aileron.

Validation of the measurement system was done through an evaluation of a typical data set, flow visualization and comparison to previous results. The typical data set and flow visualization indicated that the wing and aileron performed in a manner that was expected. The Comparisons between the rolling, yawing and hinge moments coefficients calculated from current tests and those conducted previously showed a good correlation in the general trend of the data for the full aileron deflection range. Differences were, however, noted between the two data sets; these occurring at high aileron deflections. These differences were primarily attributed to the current tests being conducted with different aerofoil profiles and at lower Reynolds numbers.

The data obtained from the hinge moment balance and external balance was still seen as satisfactory, allowing for use in measuring the effects of aileron trailing edge manipulations.

Four aileron test pieces with increasing trailing edge thicknesses were tested. The effects of this change in thickness was investigated at four different angle of attack cases, namely low angles of attack, just before stall, at stall and above stall. For the pre-stall cases it was seen that the increase in the trailing edge thickness of the aileron produced negligible effects on the the rolling, yawing or hinge moment coefficients in either the trend of the data or magnitude of the coefficients. Small changes were noted for the hinge moment coefficients at high angles of attack; however these were seen as inconsequential. This was largely due to the conditions under which differences occurred, being outside the typical flight envelope of general aviation aircraft.

It was concluded, from the test results, that the trailing edge thickness of an aileron need not be manufactured to the conventional thickness that is commonly desired. The allowance for a thicker aileron trailing edge thickness in the design of future aircraft will have minimal effect on the aileron performance while allowing for less restrictions in their manufacture.

10 RECOMMENDATIONS

The results from the investigation into the effect of thicker aileron trailing edges showed that there was little effect on the aerodynamic coefficients of the aerofoil and aileron itself. Based on this the following list are recommendations for future work in the investigation of aileron trailing edge manipulations:

- The measurement of and effect that thicker aileron trailing edge thicknesses has on the lift and drag and pitching moment coefficients should be investigated. This will allow for a more thorough description of the effect of having thicker trailing edges. The addition of lift coefficient data will also allow for better comparisons to previous research and hence further validation of the results.
- Investigations into the use of thicker ailerons would also be recommended to ascertain if there is a turning point at which the use of a thicker aileron begins to show noticeable deteriorations in the aileron performance or if there exists an aileron trailing edge thickness for which an improvement in the aileron performance can be seen.
- The effect that thicker trailing edges has on other aileron shapes and configurations such as Frise ailerons could also be insightful. This could show whether the effects seen from the investigation of plain flap type ailerons also pertains to these other aileron types.
- A method for locking the aileron at a particular deflection would also be of use. This would prevent the oscillation of the aileron at higher angles of attack, allowing for cleaner data to be obtained for the aerofoil aerodynamic coefficients such as roll and yaw. The aileron could then be unlocked and the hinge data could be obtained without spoiling the data for other coefficients. The use of an internal or external balance for the aileron could also assist in the reduction of the oscillations.

11 REFERENCES

- Abzug, M. J. & Larrabee, E. E., 2002. *Airplane Stability and Control*. s.l.:Cambridge University Press.
- Anon., n.d.
- Bacon, D. L., 1924. *N.A.C.A. Report 161: The Distribution of Lift Over Wing Tips and Ailerons*, Langley Field: Langley Memorial Aeronautical Laboratory.
- Baker, J. P., van Dam, C. P. & Gilbert, B. L., 2008. *Flatback Airfoil Wind Tunnel Experiment*. New Mexico: Sandia National Laboratories.
- Cavanaugh, M. A., Robertson, P. & Mason, W. H., 2007. *Wind Tunnel Test of Gurney Flaps and T-Strips on an NACA 23012 Wing*, Virginia: American Institute of Aeronautics and Astronautics.
- Cooperman, A. M. et al., 2010. *Aerodynamic Performance of Thick Blunt Trailing Edge*. Chicago, AIAA.
- Drela, M., 1989. *Integral Boundary Layer Formulation for Blunt Trailing Edges*, Massachusetts: Massachusetts Institute of Technology.
- El-Gammal, M., Naughton, J. W. & Hangan, H., 2010. Drag Force Balance of a Blunt and Divergent Trailing-Edge Airfoil. *Journal of Aircraft*, Volume 47.
- Gammal, M., Naughton, J. & Hangan, H., 2010. Drag Force Balance of a Blunt and Divergent Trailing-Edge Airfoil. *Journal of Aircraft*, Volume 47.
- Gilrith, R. R. & Turner, W. N., 1941. *Lateral Control Required for Satisfactory Flying Qualities Based on Flight Tests of Numerous Airplanes*, Langely Field: National Advisory Committee for Aeronautics.
- Goranson, R. F., 1946. *N.A.C.A. Technical Note 1085: Flight Tests of Experimental Beveled-Trailing-Edge Frise Ailerons on a Fighter Airplane*, Langely Field: Langley Memorial Aeronautical Laboratory.
- Gurbacki, H. & Bragg, M., 2001. Sensing Aircraft Icing Effects by Unsteady Flap Hinge-Moment Measurement. *Journal of Aircraft*, Volume 38.
- Harris, T. A. & Weick, F. E., 1932. *N.A.C.A. Report 424: Wind-Tunnel Research Comparing Lateral Control Devices, Particularly at High Angles of Attack IV - Floating Tip Ailerons on Rectangular Wings*, Langely Field: Langely Memorial Aeronautical Laboratory.
- Heald, R. H., 1933. *N.A.C.A. Technical Note 441: Rolling, Yawing, and Hinge Moments Produced by Rectangular Ailerons*, Washington: Bureau of Standards.

- Heald, R. H., 1933. *N.A.C.A. Technical Note 448: Effect of Aileron Displacement on Wing Characteristics*, Washington: Bureau of Standards.
- Hoener, 1950. *Base Drag and Thick Trailing Edges*, s.l.: Journal Aeronautical Sciences.
- Hoerner, S. F., 1965. *Fluid-Dynamic Drag*. Bakersfield: S. F. Hoerner.
- Hoerner, S. F. & Borst, H. V., 1985. *Fluid Dynamic Lift*, New York: L A Hoerner.
- Holman, J. P., 2012. *Experimental Methods for Engineers*. New York: McGraw-Hill.
- Jacobs, E. N. & Sherman, A., 1937. *Airfoil Section Characteristics as Affected by Variations of the Reynolds Number*, Langely Virginia: National Advisory Committee of Aeronautics.
- Jacobs, E. N. & Sherman, A., 1937. *N.A.C.A. Report 586: Airfoil Section Characteristics as Affected by Variations of the Reynolds Number*, Langely Virginia: National Advisory Committee of Aeronautics.
- Jones, R. T. & Weick, F. E., 1937. *N.A.C.A. Report 605: Resume and Analysis of N.A.C.A. Lateral Control Research*, Langely Field: Langely Memorial Aeronautical Laboratory.
- Katzoff, S., Silverstein, A. & Bullivant, W. K., 1938. *N.A.C.A. Report 651: Downwash and Wake Behind Plain and Flapped Airfoils*, Langely Field: Langely Memorial Aeronautical Laboratory.
- Kempel, R. W., 1971. *N.A.S.A. TN D-6496 Analysis of a Coupled Roll-Spiral-Mode, Pilot-Induced Oscillation Experienced With The M2-F2 Lifting Body*, Edwards: NASA Flight Research Center.
- Khorrami, M., Berkman, M. & Choudhari, M., 2000. Unsteady Flow Computations of a Slat with a Blunt Trailing Edge. *AIAA*, Volume 38.
- Kroo, I., 2004. *Future Technology and Aircraft Types*. [Online] Available at: <http://adg.stanford.edu/aa241/intro/futureac.html> [Accessed 27 May 2014].
- Lemes, R. & Catalano, F., 2004. *Experimental Analysis of the confluent boundary layer between flpa and a main element with saw-toothed trailing edge*. Japan, ICAS.
- Lotz, R. D. & Thompson, B. E., 1996. *Divergent-Trailing-Edge Airfoil Flow*, New York: Journal of Aircraft.
- Monish, B. H., 1930. *N.A.C.A. Report 370: Effect of Variation of Chord and Span of Ailerons on Hinge Moments at Several Angles of Pitch*, Washington: Bureau of Standards.
- Nagaraja, K., Lakin, G. & Bartley, J., 1982. Flutter and Oscillatory Pressure Tests on a 727 Aileron in a Wind Tunnel. *Journal of Aircraft*, Volume 19, pp. 781-786.

Noyes, R. W. & Weick, F. E., 1932. *N.A.C.A. Report 422: Wind-Tunnel Research Comparing Lateral Control Devices, Particularly at High Angles of Attack II - Slotted Ailerons and Frise Ailerons*, Langley Field: Langley Memorial Aeronautical Laboratory.

Pezzella, G. et al., 2014. *Aerodynamic characterization of HEXAFly scramjet propelled hypersonic vehicle*. Atlanta, AIAA.

Rogallo, F. M. & Lowry, J. G., 1942. *N.A.C.A. Wartime Report 481 - Wind-tunnel Investigation of a Plain Aileron and a Balanced Aileron on a Tapered Wing with Full-Span Duplex Flaps*, Langley Field: Langley Memorial Aeronautical Laboratory.

Rogallo, F. M. & Purser, P. E., 1941. *N.A.C.A. Wartime Report 374: Wind-Tunnel Investigation of 20 percent chord plain and frise ailerons on an NACA 23012 Airfoil*, Langley Virginia: National Advisory Committee for Aeronautics.

Sears, R. I., 1942. *N.A.C.A. Wartime Report 346 - Application of Balancing Tabs to Ailerons*, Langley Field: Langley Memorial Aeronautical Laboratory.

Sears, R. I. & Liddell, R. B., 1942. *N.A.C.A. Wartime Report 454: Wind-Tunnel Investigation of Control-Surface Characteristics VI - A 30-Percent-Chord Plain Flap on the NACA 0015 Airfoil*, Langley Field: National Advisory Committee for Aeronautics.

Shortal, J. A. & Weick, F. E., 1932. *N.A.C.A. Report 439: Wind-Tunnel Research Comparing Lateral Control Devices, Particularly at High Angles of Attack V - Spoilers and Ailerons on Rectangular Wings*, Langley Field: Langley Memorial Aeronautical Laboratory.

Shortal, J. A. & Weick, F. E., 1933. *N.A.C.A. Technical Note 445: Wind-Tunnel Research Comparing Lateral Control Devices, Particularly at High Angles of Attack VIII - Straight and Skewed Ailerons on Wings with Rounded Tips*, Langley Field: Langley Memorial Aeronautical Laboratory.

Shortal, J. A. & Weick, F. E., 1935. *N.A.C.A. Report 547: Development of the N.A.C.A. Slot-Lip Aileron*, Langley Field: Langley Memorial Aeronautical Laboratory.

Shrouder, S., 2010. *Showcase UAV Demonstrates Flapless Flight*. [Online] Available at: <http://www.baesystems.com/AboutUs/ShowcaseUAVDemonstratesFlaplessFlight/index.htm> [Accessed 31 03 2011].

Smith, H. A. & Schaefer, R. F., 1950. *N.A.C.A. Technical Note 2074: Aerodynamic Characteristics at Reynolds Numbers of 3.0×10^6 and 6.0×10^6 of Three Airfoil Sections Formed by Cutting Off Various Amounts from the Rear Portion of the NACA 0012 Airfoil Section*, New York: National Advisory Committee for Aeronautics.

- Soinne, E., 2000. *Aerodynamic and Flight Dynamic Simulations of Aileron Characteristics*, Stockholm: Department of Aeronautics Royal Institute of Technology.
- Standish, K. J. & van Dam, C. P., 2003. *Aerodynamic Analysis of Blunt Trailing Edge Airfoils*, Davis: University of California.
- Strauss, H. & Fields, M., 1950. *Flight Investigation of the Effect of Thickening the Aileron Trailing Edge on Control Effectiveness for Sweptback Tapered Wings having sharp and round nose sections*, Washington: NACA.
- Tamayama, M., Kheirandish, H. & Nakamichi, J., 2003. Study of the Transonic Flows around a Thin Wing with an Aileron. *Transactions of the Japan Society for Aeronautical and Space Sciences*, Volume 46, pp. 186-194.
- Thompson, B. E. & Whitelaw, J. H., 1989. Trailing Edge Region of Airfoils. *Journal of Aircraft*, Volume 26.
- Toll, T. A., 1946. *N.A.C.A. Report 868: Summary of Lateral-Control Research*, Langley Field: Langley Memorial Aeronautical Laboratory.
- Torenbeek, E., 1976. *Synthesis of Subsonic Airplane Design*. Rotterdam: Delft University Press.
- van Dam, C. P. & Kahn, D. L., 2008. *Trailing Edge Modifications for Flatback Airfoils*, New Mexico: Sandia National Laboratories.
- van Dyke, M., 2005. *An Album of Fluid Motion*. California: Stanford University.
- Wenzinger, C. J., 1937. *N.A.C.A. Report 611 - Wind-Tunnel Investigation of Tapered Wings with Ordinary Ailerons and Partial-Span Split Flaps*, Langley Field: Langley Memorial Aeronautical Laboratory.
- Wenzinger, C. J. & Weick, F. E., 1931. *N.A.C.A. Report 419: Wind-Tunnel Research Comparing Lateral Control Devices, Particularly at High Angles of Attack I - Ordinary Ailerons on Rectangular Wings*, Langley Field: Langley Memorial Aeronautical Laboratory.
- Wenzinger, C. J. & Weick, F. E., 1932. *N.A.C.A. Report 423: Wind-Tunnel Research Comparing Lateral Control Devices, Particularly at High Angles of Attack III - Ordinary Ailerons Rigged Up 10 Degrees When Neutral*, Langley Field: Langley Memorial Aeronautical Laboratory.
- Wenzinger, C. J. & Weick, F. E., 1932. *N.A.C.A. Report 443: Wind-Tunnel Research Comparing Lateral Control Devices, Particularly at High Angles of Attack VII - Handley Page Tip and Full Span Slots With Ailerons and Spoilers*, Langley Field: Langley Memorial Aeronautical Laboratory.

Wenzinger, C. J. & Weick, F. E., 1934. *N.A.C.A. Report 499: Wind-Tunnel Research Comparing Lateral Control Devices, Particularly at High Angles of Attack XII - Upper-Surface Ailerons on Wings with Split Flaps*, Langely Field: Langley Memorial Aeronautical Laboratory.

Xu, M., Liu, L., Tang, G. & Chen, K., 2011. Design of dive trajectory of hypersonic near-space vehicle with minimum hinge moment. *Journal of Ballisitics* , Volume 23, pp. 1-6.

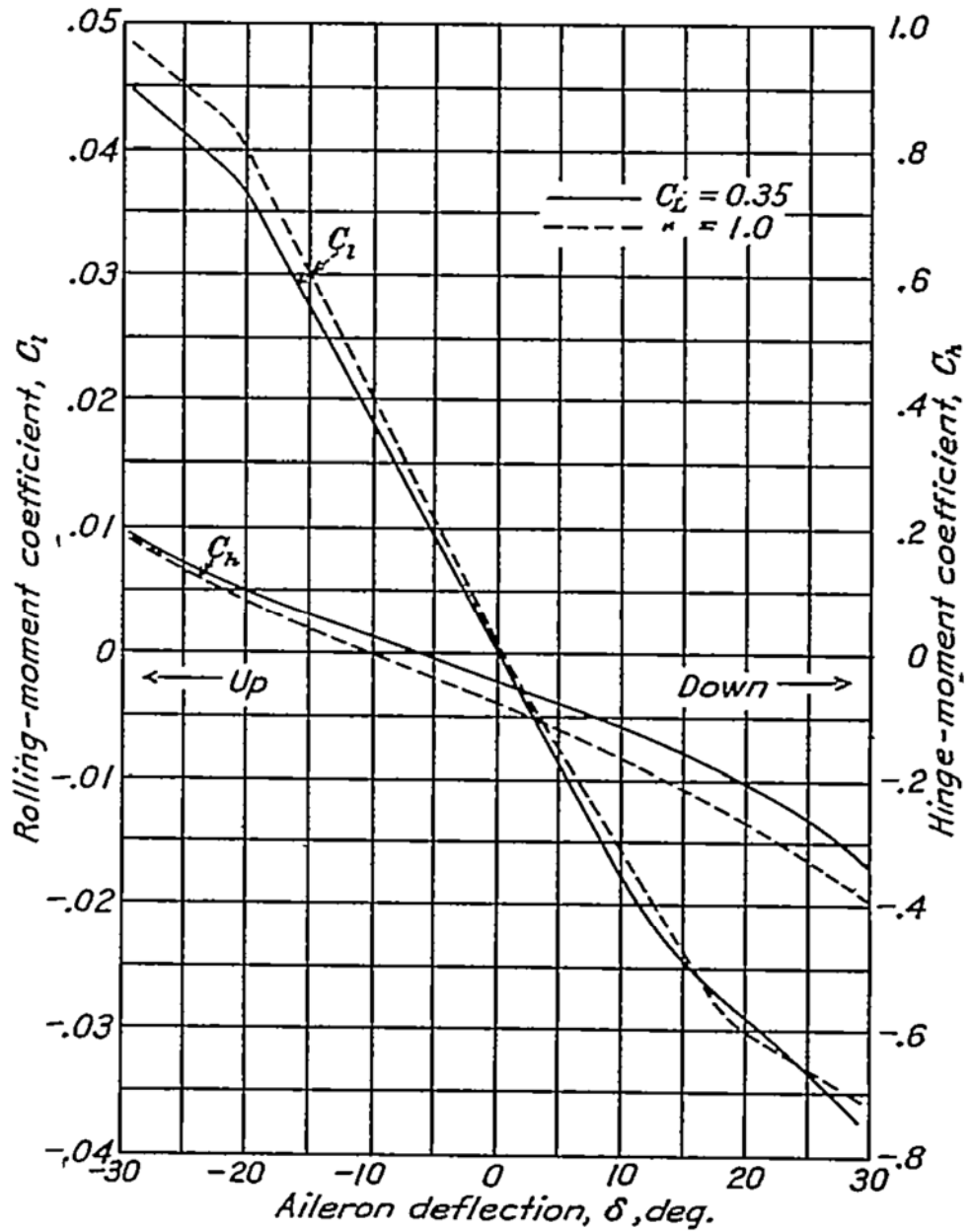


Figure A.2: Typical rolling and hinge moment coefficient curves for plain ailerons (Jones & Weick, 1937).

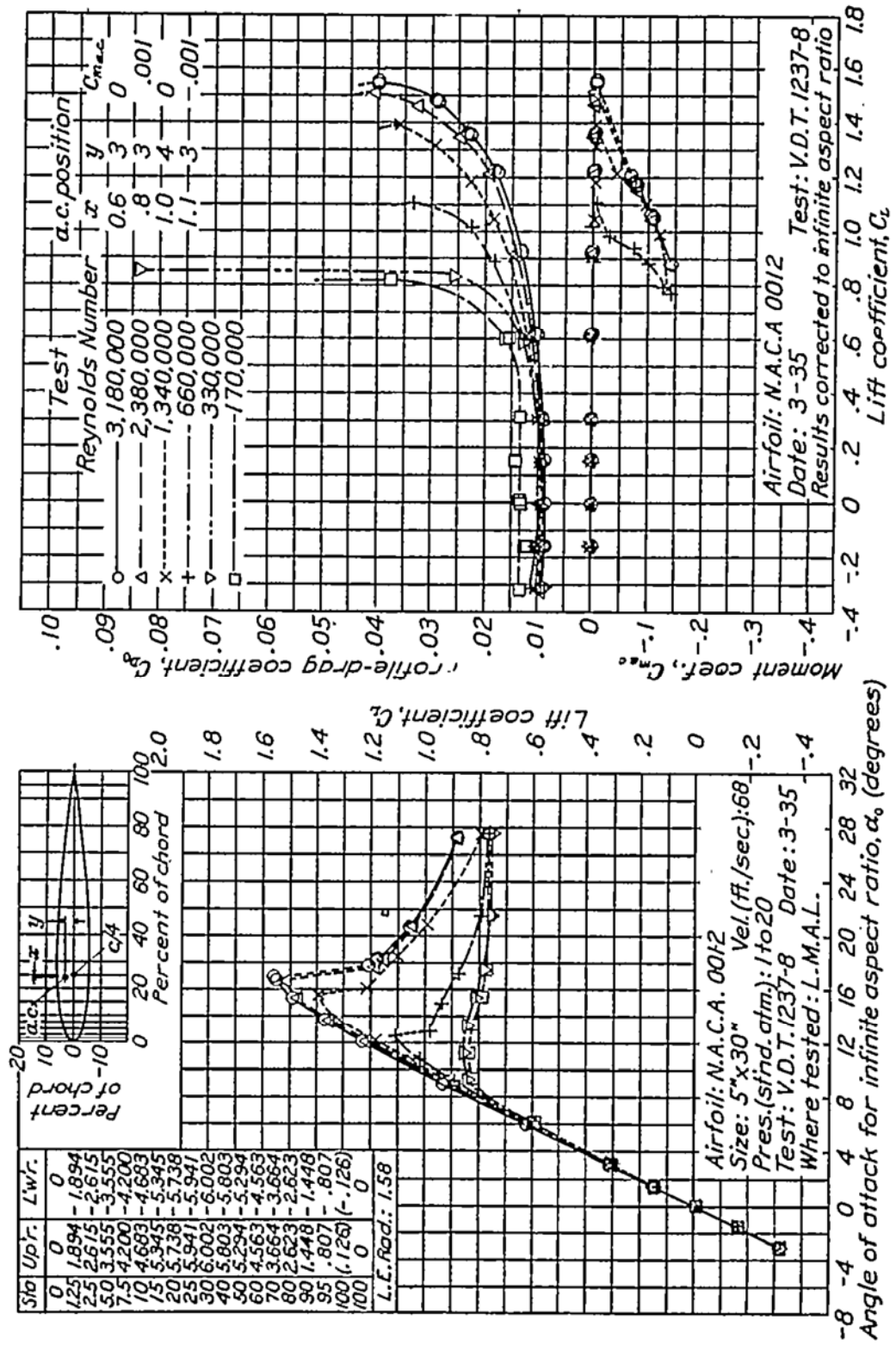


Figure A.3: Aerofoil section characteristics of a NACA0012 as affected by variations of the Reynolds number (Jacobs & Sherman, 1937).

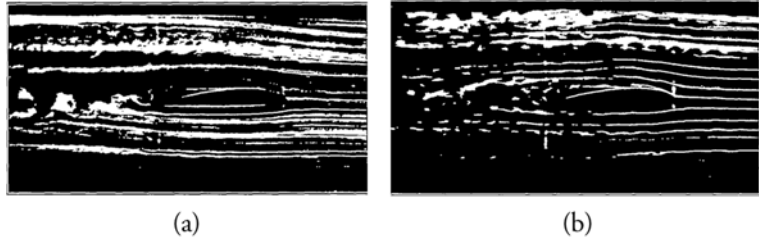
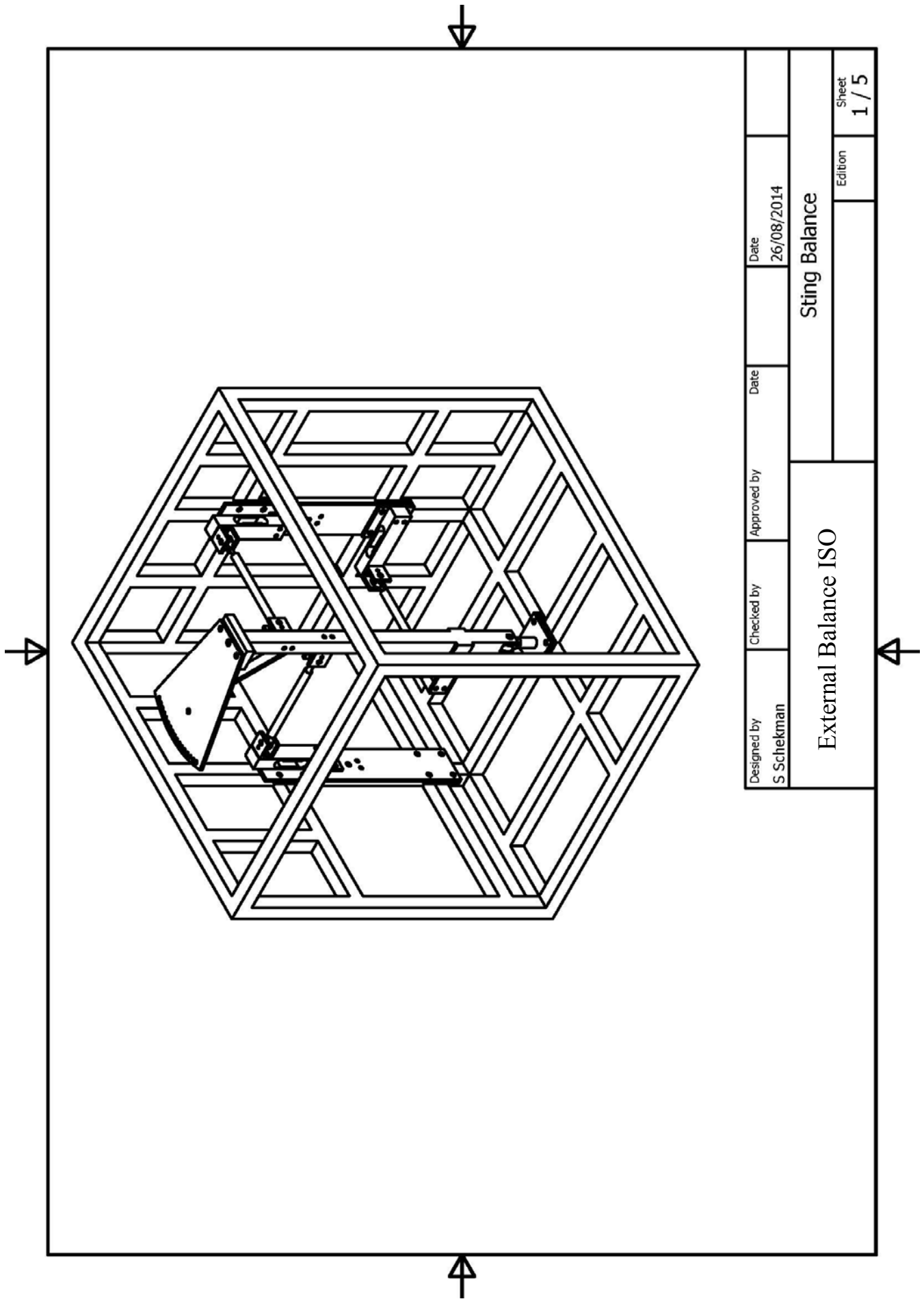


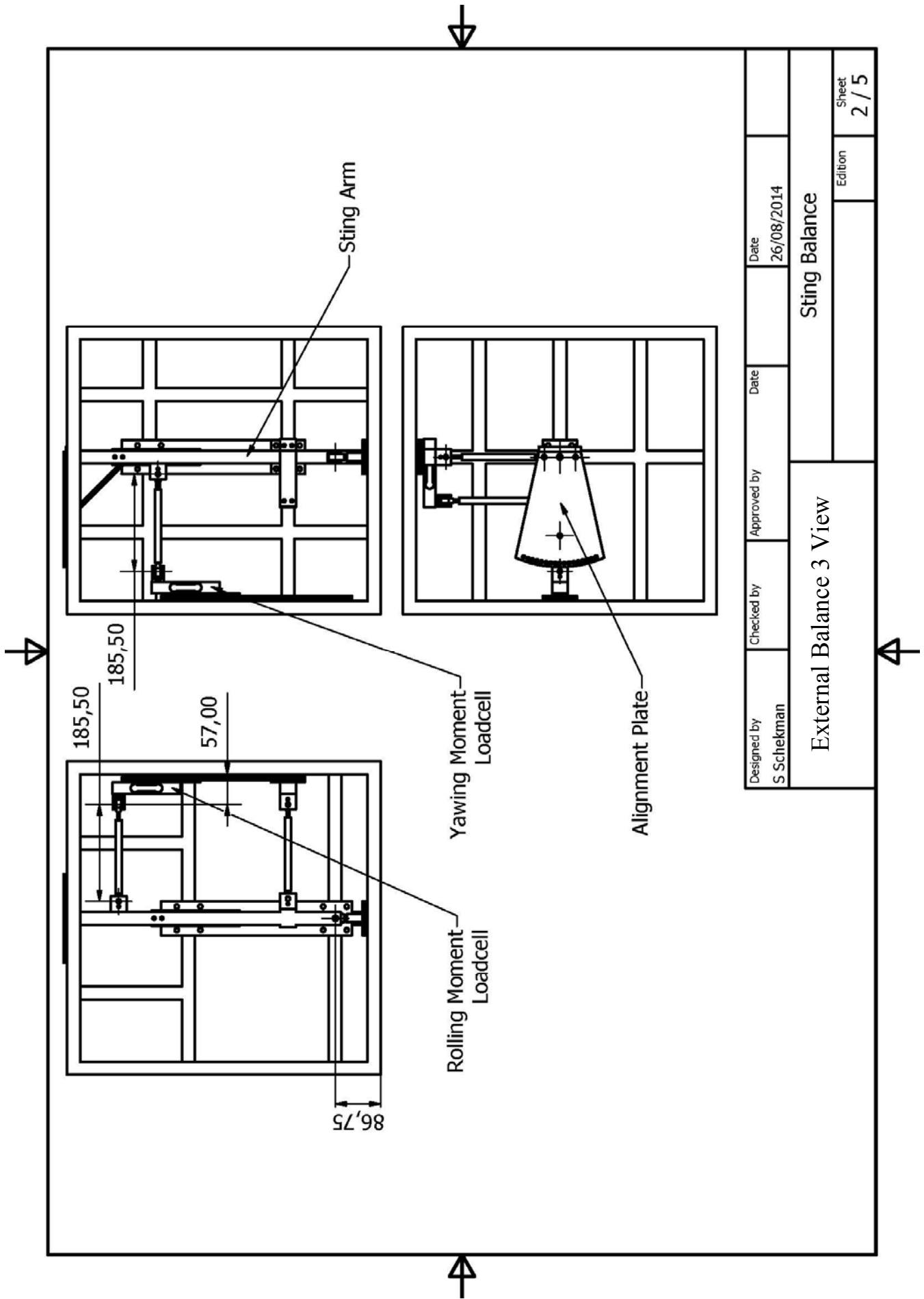
Figure A.4: Separation occurring on an airfoil at a low angle of attack, at low a Reynolds number (a) and an increased Reynolds number (b) (Jacobs & Sherman, 1937)

Appendix B: ENGINEERING DRAWINGS



Designed by S Schekman	Checked by	Approved by	Date 26/08/2014	Date 26/08/2014	Sheet 1 / 5
External Balance ISO			Sting Balance		
			Edition		

Figure B.1: External Balance ISO View



Designed by S Schekman	Checked by	Approved by	Date 26/08/2014
External Balance 3 View			Sting Balance
			Edition 2 / 5

Figure B.2: External Balance 3 View

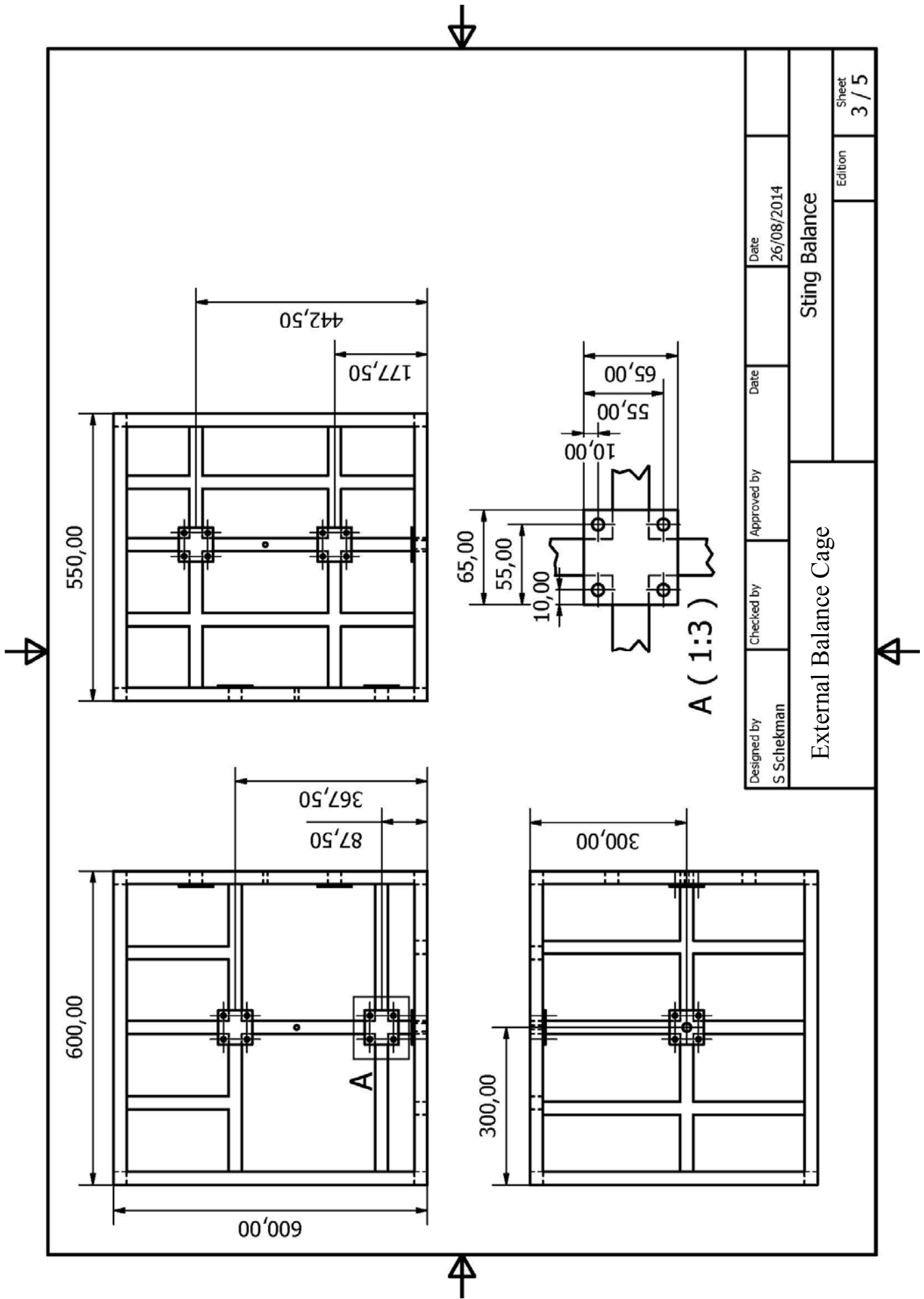


Figure B.3: External Balance Cage

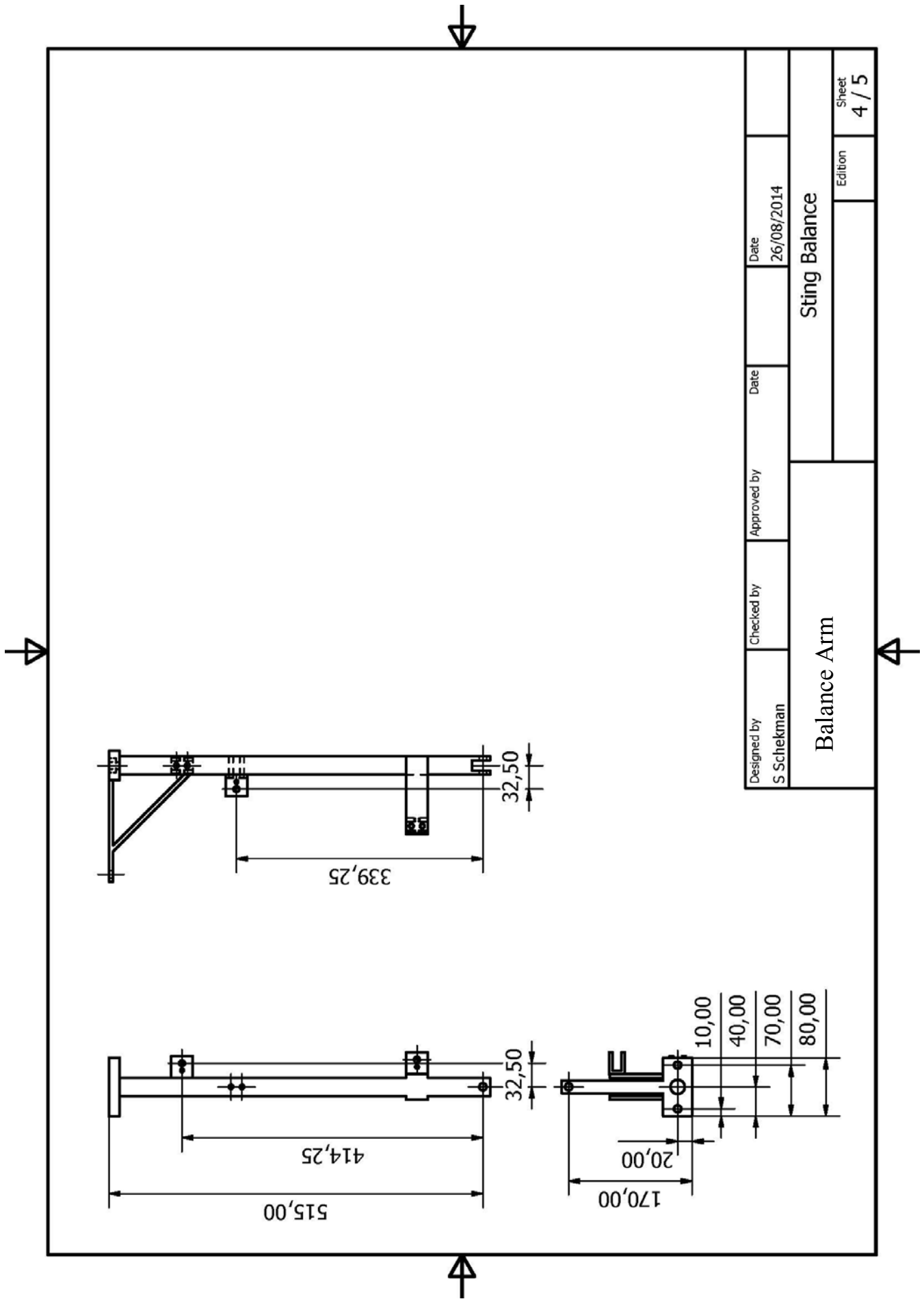


Figure B.4: Balance Arm

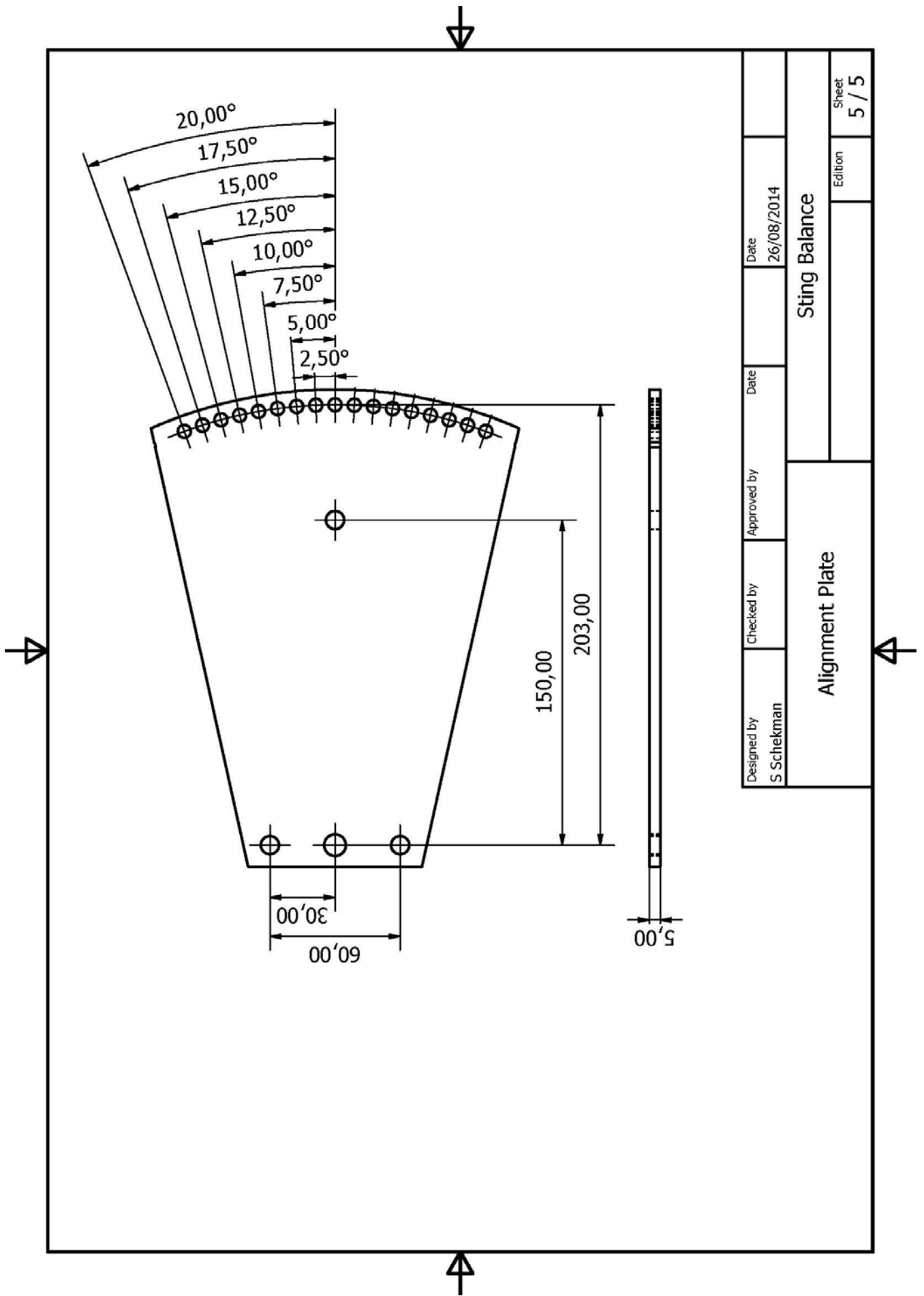
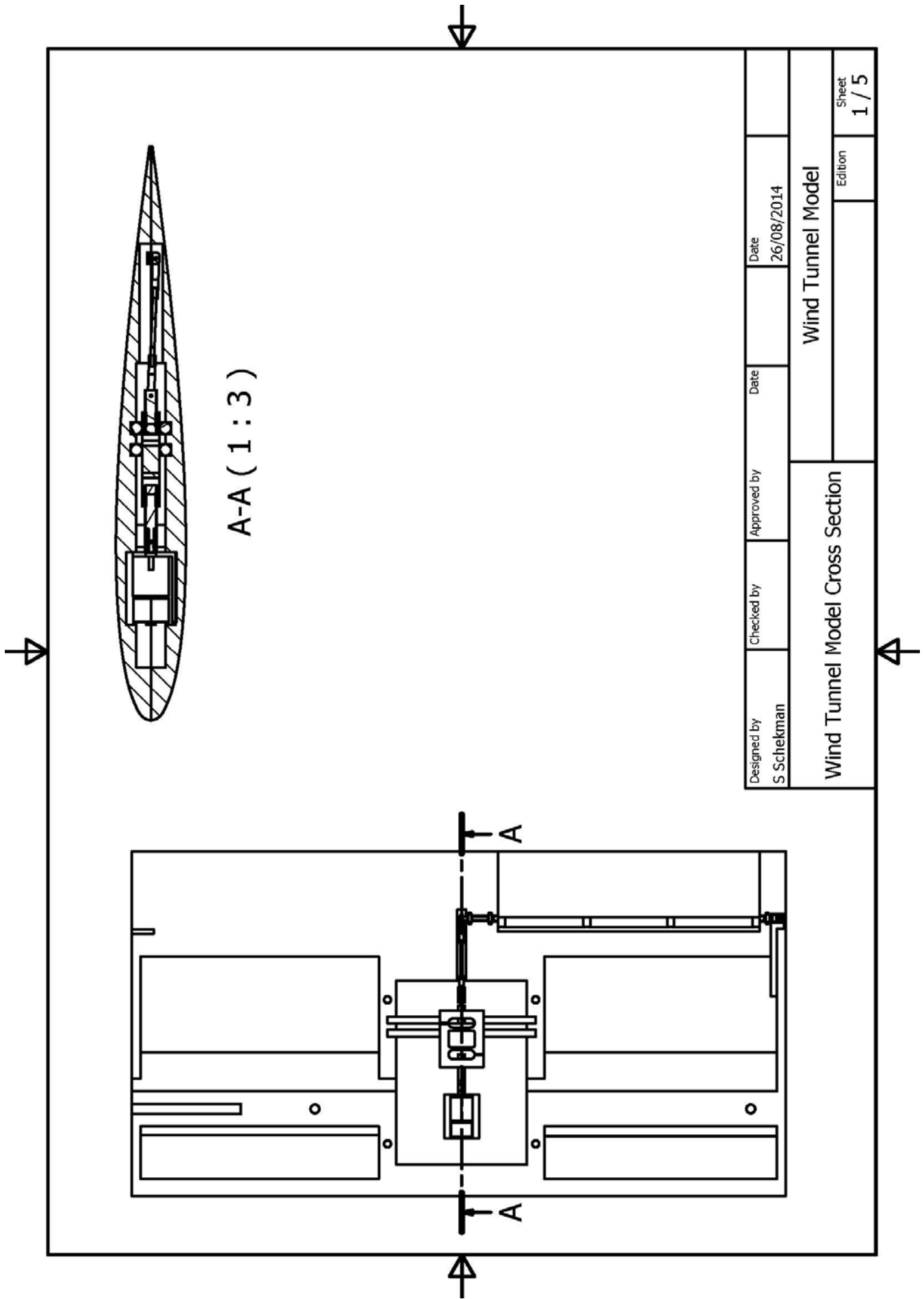


Figure B.5: Wing Alignment Plate



Designed by S Schekman	Checked by	Approved by	Date 26/08/2014
Wind Tunnel Model Cross Section			Date 26/08/2014
Wind Tunnel Model			Edition
			Sheet 1 / 5

Figure B.6: Wing Assembly

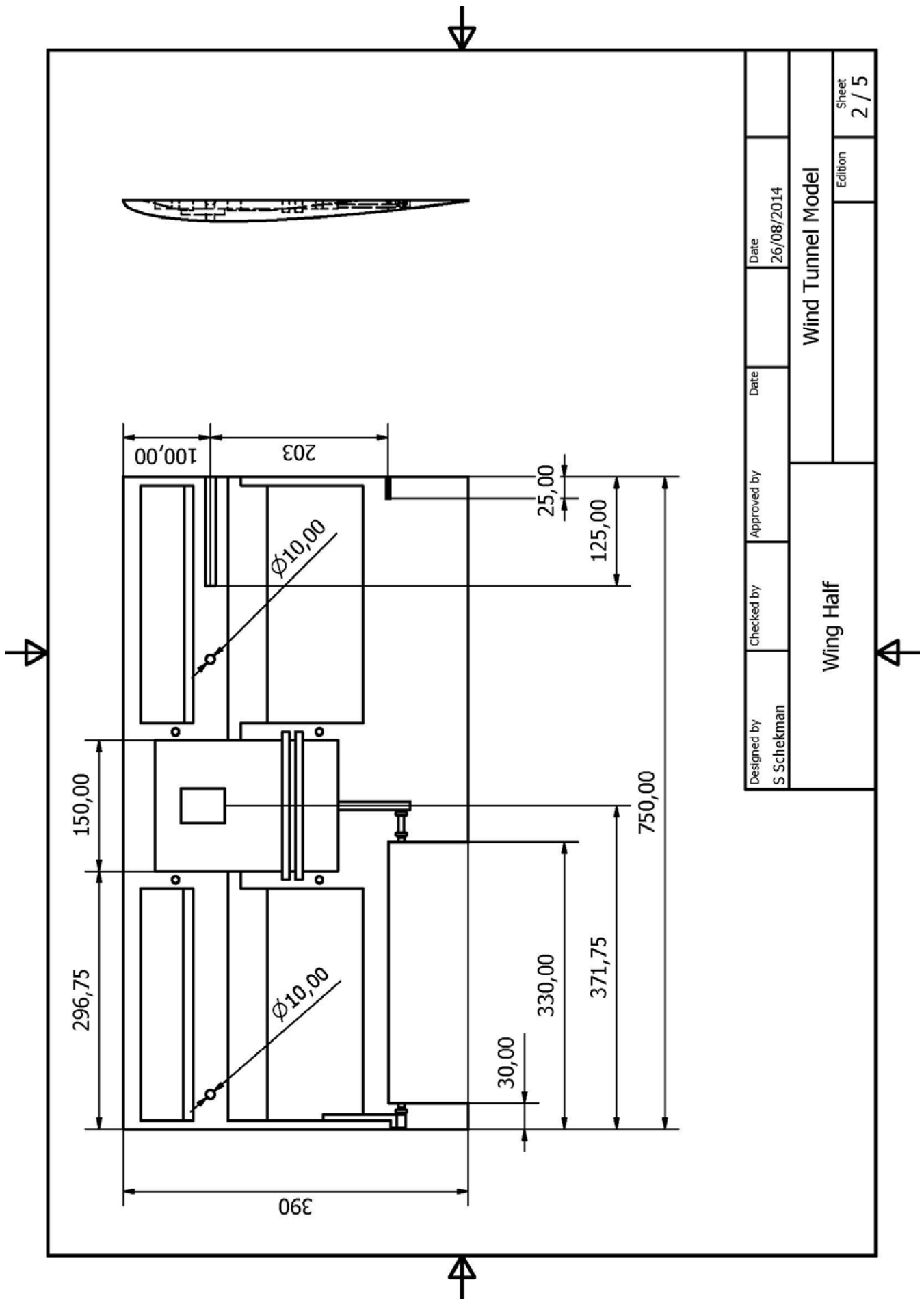


Figure B.7: Wing Half

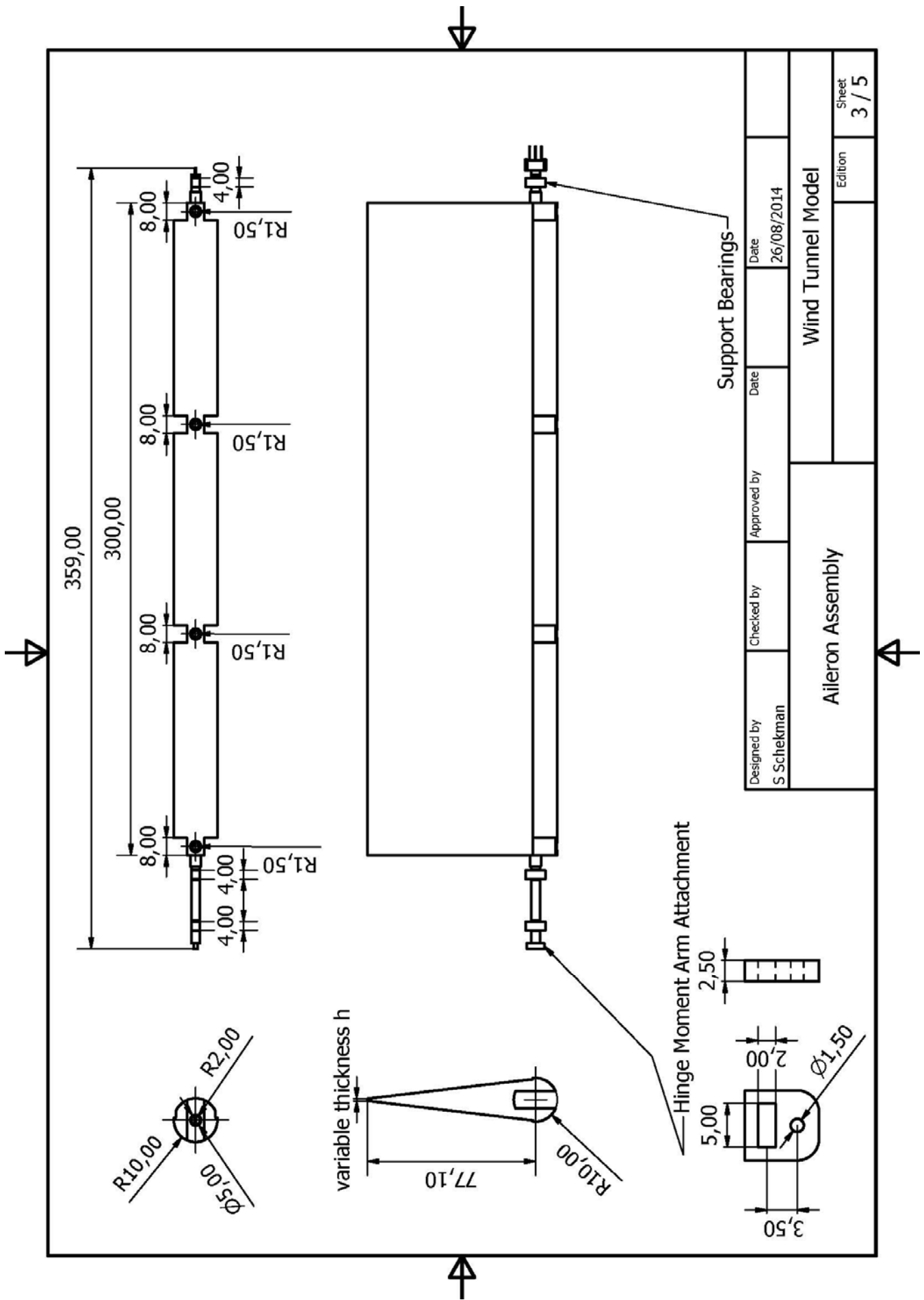
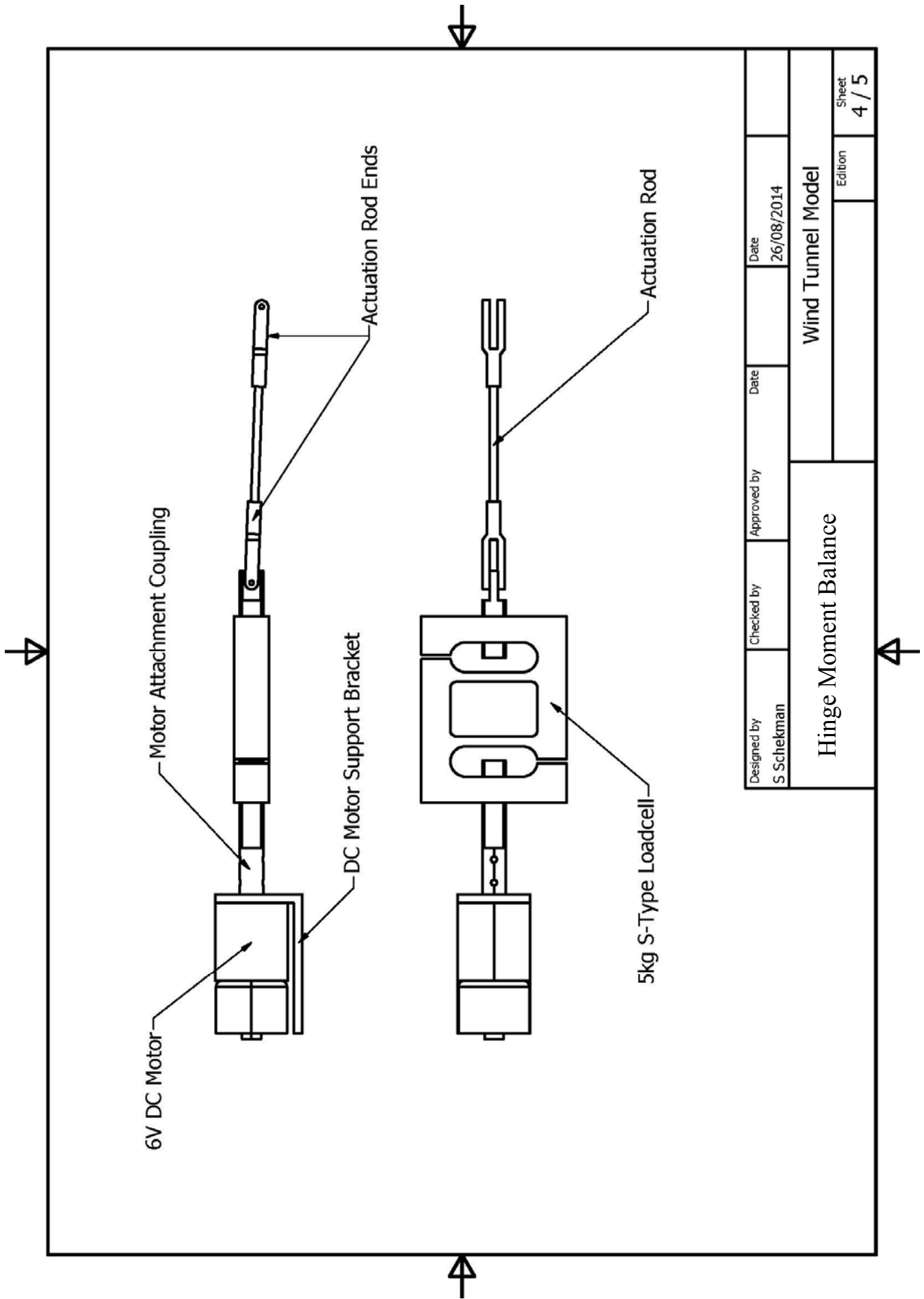
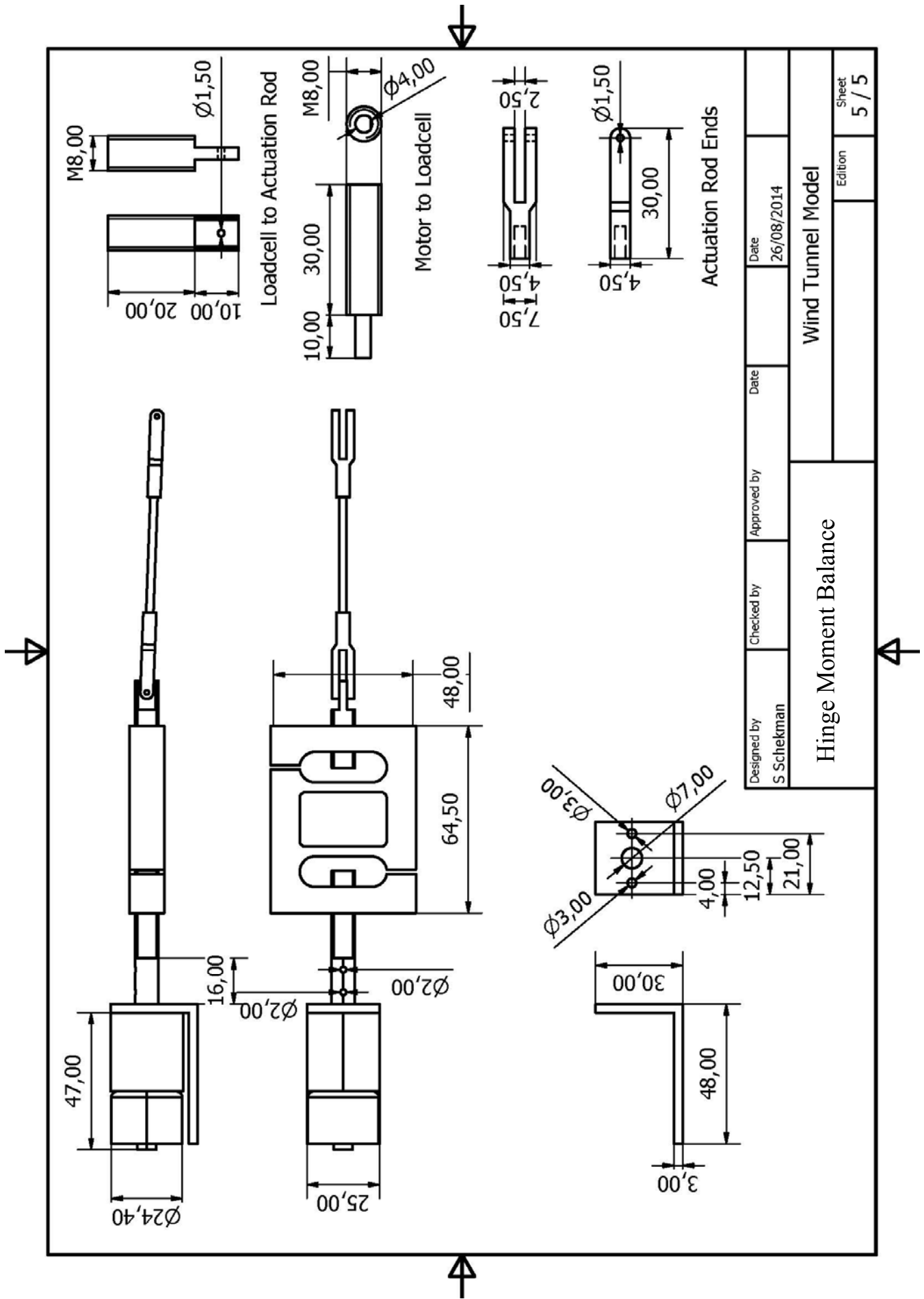


Figure B.8: Aileron Assembly



Designed by S Schekman	Checked by	Approved by	Date 26/08/2014	Date
Hinge Moment Balance			Wind Tunnel Model	
			Edition	Sheet 4 / 5

Figure B.9: Hinge Moment Balance Overview



Designed by S Schekman	Checked by	Approved by	Date 26/08/2014
Hinge Moment Balance		Wind Tunnel Model	
		Edition	Sheet 5 / 5

Figure B.10: Hinge Moment Balance

NI USB-621x Specifications

Specifications listed below are typical at 25 °C unless otherwise noted. Refer to the *NI USB-621x User Manual* for more information about USB-621x devices.



Caution The input/output ports of this device are not protected for electromagnetic interference due to functional reasons. As a result, this device may experience reduced measurement accuracy or other temporary performance degradation when connected cables are routed in an environment with radiated or conducted radio frequency electromagnetic interference.

To ensure that this device functions within specifications in its operational electromagnetic environment and to limit radiated emissions, care should be taken in the selection, design, and installation of measurement probes and cables.

Français Deutsch 日本語 한국어 简体中文 ni.com/manuals

Analog Input

<p>Number of channels</p> <p>USB-6210/6211/6212/ 6215/6216 8 differential or 16 single ended</p> <p>USB-6218 16 differential or 32 single ended</p> <p>ADC resolution 16 bits</p> <p>DNL No missing codes guaranteed</p> <p>INL Refer to the <i>AI Absolute Accuracy Tables</i></p> <p>Sampling rate</p> <p>Maximum</p> <p>USB-6210/6211/6215/6218 ... 250 kS/s single channel, 250 kS/s multichannel (aggregate)</p> <p>USB-6212/6216 400 kS/s single channel, 400 kS/s multichannel (aggregate)</p> <p>Minimum 0 S/s</p> <p>Timing accuracy 50 ppm of sample rate</p> <p>Timing resolution 50 ns</p> <p>Input coupling DC</p>	<p>Input range ±10 V, ±5 V, ±1 V, ±0.2 V</p> <p>Maximum working voltage for analog inputs (signal + common mode) ±10.4 V of AI GND</p> <p>CMRR (DC to 60 Hz) 100 dB</p> <p>Input impedance</p> <p>Device on</p> <p>AI+ to AI GND >10 GΩ in parallel with 100 pF</p> <p>AI- to AI GND >10 GΩ in parallel with 100 pF</p> <p>Device off</p> <p>AI+ to AI GND 1200 Ω</p> <p>AI- to AI GND 1200 Ω</p> <p>Input bias current ±100 pA</p> <p>Crosstalk (at 100 kHz)</p> <p>Adjacent channels -75 dB</p> <p>Non-adjacent channels -90 dB</p> <p>Small signal bandwidth (-3 dB)</p> <p>USB-6210/6211/6215/6218 450 kHz</p> <p>USB-6212/6216 1.5 MHz</p>
---	---



Input FIFO size.....4,095 samples
 Scan list memory4,095 entries
 Data transfers.....USB Signal Stream,
 programmed I/O
 Overvoltage protection (AI <0..31>, AI SENSE)
 Device on±30 V for up to
 two AI pins
 Device off±20 V for up to
 two AI pins
 Input current during
 overvoltage condition±20 mA max/AI pin

Settling Time for Multichannel Measurements

Accuracy, full scale step, all ranges

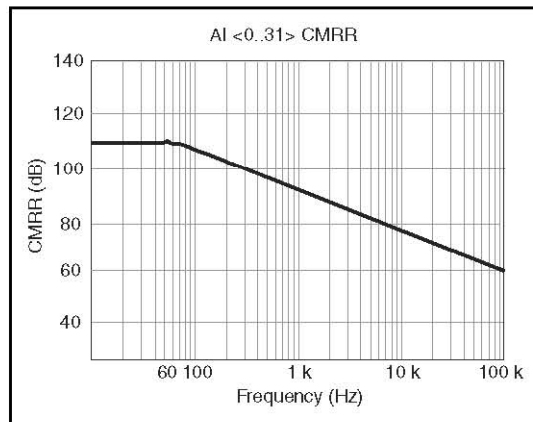
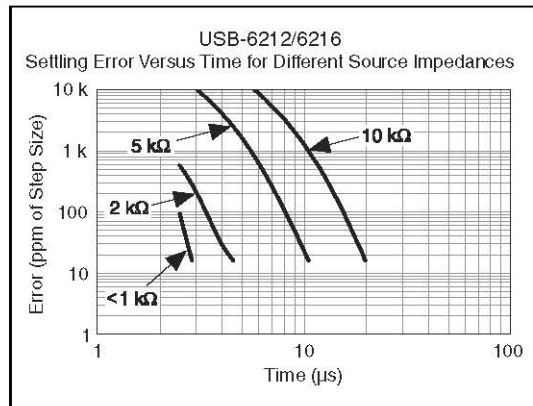
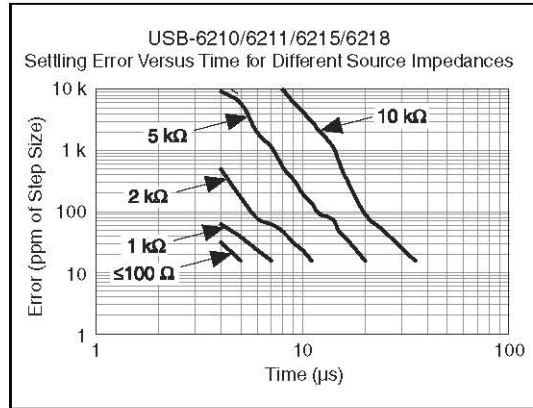
USB-6210/6211/6215/6218

- ±90 ppm of step (±6 LSB).....4 µs convert interval
- ±30 ppm of step (±2 LSB).....5 µs convert interval
- ±15 ppm of step (±1 LSB).....7 µs convert interval

USB-6212/6216

- ±90 ppm of step (±6 LSB).....2.5 µs convert interval
- ±30 ppm of step (±2 LSB).....3.5 µs convert interval
- ±15 ppm of step (±1 LSB).....5.5 µs convert interval

Typical Performance Graphs



Analog Output

Number of channels	
USB-6210	0
USB-6211/6212/6215/ 6216/6218	2
DAC resolution	16 bits
DNL	±1 LSB
Monotonicity	16 bit guaranteed
Maximum update rate	
1 channel	250 kS/s
2 channels	250 kS/s per channel
Timing accuracy	50 ppm of sample rate
Timing resolution	50 ns
Output range	±10 V
Output coupling	DC
Output impedance	0.2 Ω
Output current drive	±2 mA
Overdrive protection	±30 V
Overdrive current	2.4 mA
Power-on state	±20 mV
Power-on glitch	±1 V for 200 ms
Output FIFO size	8,191 samples shared among channels used
Data transfers	USB Signal Stream, programmed I/O
AO waveform modes:	
• Non-periodic waveform	
• Periodic waveform regeneration mode from onboard FIFO	
• Periodic waveform regeneration from host buffer including dynamic update	
Settling time, full scale step	
15 ppm (1 LSB)	32 μs
Slew rate	5 V/μs
Glitch energy	
Magnitude	100 mV
Duration	2.6 μs

Calibration (AI and AO)

Recommended warm-up time	15 minutes
Calibration interval	1 year

AI Absolute Accuracy Table (USB-6210/6211/6215/6218)

Nominal Range		Residual Gain Error (ppm of Reading)	Gain Tempco (ppm/°C)	Reference Tempco	Residual Offset Error (ppm of Range)	Offset Tempco (ppm of Range/°C)	INL Error (ppm of Range)	Random Noise, σ (μ Vrms)	Absolute Accuracy at Full Scale ¹ (μ V)	Sensitivity ² (μ V)
Positive Full Scale	Negative Full Scale									
10	-10	75	7.3	5	20	34	76	229	2,690	91.6
5	-5	85	7.3	5	20	36	76	118	1,410	47.2
1	-1	95	7.3	5	25	49	76	26	310	10.4
0.2	-0.2	135	7.3	5	40	116	76	12	88	4.8

AbsoluteAccuracy = Reading · (GainError) + Range · (OffsetError) + NoiseUncertainty

GainError = ResidualGainError + GainTempco · (TempChangeFromLastInternalCal) + ReferenceTempco · (TempChangeFromLastExternalCal)

OffsetError = ResidualOffsetError + OffsetTempco · (TempChangeFromLastInternalCal) + INL_Error

NoiseUncertainty = $\frac{\text{RandomNoise} \cdot 3}{\sqrt{100}}$ For a coverage factor of 3 σ and averaging 100 points.

¹ Absolute accuracy at full scale on the analog input channels is determined using the following assumptions:

TempChangeFromLastExternalCal = 10 °C

TempChangeFromLastInternalCal = 1 °C

number_of_readings = 100

CoverageFactor = 3 σ

For example, on the 10 V range, the absolute accuracy at full scale is as follows:

GainError = 75 ppm + 7.3 ppm · 1 + 5 ppm · 10

OffsetError = 20 ppm + 34 ppm · 1 + 76 ppm

NoiseUncertainty = $\frac{229 \mu\text{V} \cdot 3}{\sqrt{100}}$ NoiseUncertainty = 68.7 μ V

AbsoluteAccuracy = 10 V · (GainError) + 10 V · (OffsetError) + NoiseUncertainty

AbsoluteAccuracy = 2,690 μ V

² Sensitivity is the smallest voltage change that can be detected. It is a function of noise.

Accuracies listed are valid for up to one year from the device external calibration.

AI Absolute Accuracy Table (USB-6212/6216)

Nominal Range		Residual Gain Error (ppm of Reading)	Gain Tempco (ppm/°C)	Reference Tempco	Residual Offset Error (ppm of Range)	Offset Tempco (ppm of Range/°C)	INL Error (ppm of Range)	Random Noise, σ (μ Vrms)	Absolute Accuracy at Full Scale ¹ (μ V)	Sensitivity ² (μ V)
Positive Full Scale	Negative Full Scale									
10	-10	75	7.3	5	20	34	76	295	2,710	118.0
5	-5	85	7.3	5	20	36	76	149	1,420	59.6
1	-1	95	7.3	5	25	49	76	32	310	12.8
0.2	-0.2	135	7.3	5	40	116	76	13	89	5.2

AbsoluteAccuracy = Reading · (GainError) + Range · (OffsetError) + NoiseUncertainty

GainError = ResidualAGainError + GainTempco · (TempChangeFromLastInternalCal) + ReferenceTempco · (TempChangeFromLastExternalCal)

OffsetError = ResidualAOffsetError + OffsetTempco · (TempChangeFromLastInternalCal) + INL_Error

NoiseUncertainty = $\frac{\text{RandomNoise} \cdot 3}{\sqrt{100}}$ For a coverage factor of 3 σ and averaging 100 points.

¹ Absolute accuracy at full scale on the analog input channels is determined using the following assumptions:

TempChangeFromLastExternalCal = 10 °C

TempChangeFromLastInternalCal = 1 °C

number_of_readings = 100

CoverageFactor = 3 σ

For example, on the 10 V range, the absolute accuracy at full scale is as follows:

GainError = 75 ppm + 7.3 ppm · 1 + 5 ppm · 10 GainError = 132 ppm

OffsetError = 20 ppm + 34 ppm · 1 + 76 ppm OffsetError = 130 ppm

NoiseUncertainty = $\frac{295 \mu\text{V} \cdot 3}{\sqrt{100}}$ NoiseUncertainty = 88.5 μ V

AbsoluteAccuracy = 10 V · (GainError) + 10 V · (OffsetError) + NoiseUncertainty AbsoluteAccuracy = 2,710 μ V

² Sensitivity is the smallest voltage change that can be detected. It is a function of noise.

Accuracies listed are valid for up to one year from the device external calibration.

A0 Absolute Accuracy Table

Nominal Range		Residual Gain Error (ppm of Reading)	Gain Tempco (ppm/°C)	Reference Tempco	Residual Offset Error (ppm of Range)	Offset Tempco (ppm of Range/°C)	INL Error (ppm of Range)	Absolute Accuracy at Full Scale ¹ (µV)
Positive Full Scale	Negative Full Scale							
10	-10	90	11	5	60	12	128	3,512

¹ Absolute Accuracy at full scale numbers is valid immediately following internal calibration and assumes the device is operating within 10 °C of the last external calibration. Accuracies listed are valid for up to one year from the device external calibration.

AbsoluteAccuracy = OutputValue · (GainError) + Range · (OffsetError)
GainError = ResidualGainError + GainTempco · (TempChangeFromLastInternalCal) + ReferenceTempco · (TempChangeFromLastExternalCal)
OffsetError = ResidualOffsetError + AOffsetTempco · (TempChangeFromLastInternalCal) + INL_Error

Digital I/O/PFI

Static Characteristics

Number of channels

Digital input

USB-6210/6211/6215	4 (PFI <0..3>/P0.<0..3>)
USB-6218	8 (PFI <0..3>/P0.<0..3>, PFI <8..11>/P0.<4..7>)

Digital output

USB-6210/6211/6215	4 (PFI <4..7>/P1.<0..3>)
USB-6218	8 (PFI <4..7>/P1.<0..3>, PFI <12..15>/P1.<4..7>)

Digital input or output

USB-6212/6216	
Screw Terminal	32 total, 16 (P0.<0..15>), 16 (PFI <0..7>/P1.<0..7>, PFI <8..15>/P2.<0..7>)
USB-6212/6216	
Mass Termination/BNC	24 total, 8 (P0.<0..7>), 16 (PFI <0..7>/P1.<0..7>, PFI <8..15>/P2.<0..7>)

Ground reference D GND

Pull-down resistor

USB-6210/6211/6215/6218	47 kΩ ±1%
USB-6212/6216	50 kΩ typical, 20 kΩ minimum

Input voltage protection¹ ±20 V on up to 8 pins

PFI Functionality

USB-6210/6211/6215/6218

PFI <0..3>, PFI <8..11>/Port 0

Functionality Static digital input, timing input

Debounce filter settings 125 ns, 6.425 μs, 2.56 ms, disable; high and low transitions; selectable per input

PFI <4..7>, PFI <12..15>/Port 1

Functionality Static digital output, timing output

Timing output sources Many AI, AO, counter timing signals

USB-6212/6216 PFI <0..15>

Functionality Static digital input, static digital output, timing input, timing output

Timing output sources Many AI, AO, counter timing signals

Debounce filter settings 125 ns, 6.425 μs, 2.56 ms, disable; high and low transitions; selectable per input

Maximum Operation Conditions

Level	Min	Max
I _{OL} output low current	—	16 mA
I _{OH} output high current	—	-16 mA

Digital Input Characteristics (USB-6210/6211/6215/6218)

Level	Min	Max
V _{IL} input low voltage	0 V	0.8 V
V _{IH} input high voltage	2 V	5.25 V
I _{IL} input low current (V _{in} = 0 V)	—	-10 μA
I _{IH} input high current (V _{in} = 5 V)	—	120 μA

Digital Input Characteristics (USB-6212/6216)

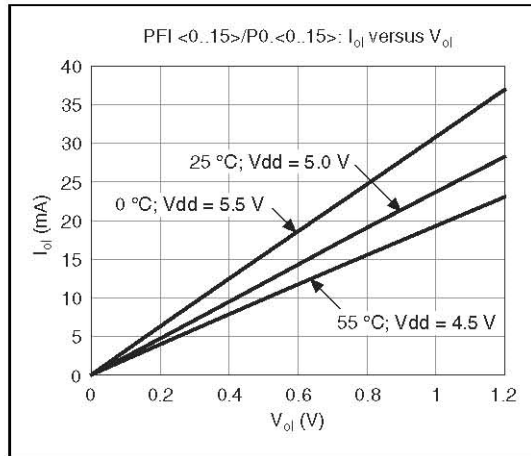
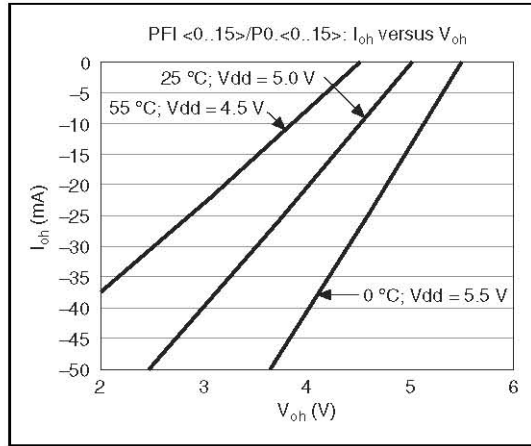
Level	Min	Max
V _{IL} input low voltage	0 V	0.8 V
V _{IH} input high voltage	2.2 V	5.25 V
I _{IL} input low current (V _{in} = 0 V)	—	-10 μA
I _{IH} input high current (V _{in} = 5 V)	—	250 μA
Positive-going threshold (VT+)	—	2.2 V
Negative-going threshold (VT-)	0.8 V	—
Delta VT hysteresis (VT+ - VT-)	0.2 V	—

Digital Output Characteristics (USB-6210/6211/6215/6218)

Parameter	Voltage Level	Current Level
V _{OL}	0.6 V	6 mA
V _{OH}	2.7 V	-16 mA
	3.8 V	-6 mA

¹ Stresses beyond those listed under *Input voltage protection* may cause permanent damage to the device.

Digital Output Characteristics (USB-6212/6216)



General-Purpose Counter/Timers

Number of counter/timers	2
Resolution	32 bits
Counter measurements	Edge counting, pulse, semi-period, period, two-edge separation
Position measurements	X1, X2, X4 quadrature encoding with Channel Z reloading; two-pulse encoding
Output applications	Pulse, pulse train with dynamic updates, frequency division, equivalent time sampling
Internal base clocks	80 MHz, 20 MHz, 0.1 MHz
External base clock frequency	0 MHz to 20 MHz
Base clock accuracy	50 ppm
Inputs	Gate, Source, HW_Arm, Aux, A, B, Z, Up_Down
Routing options for inputs	
USB-6210/6211/6215/6218	PFI <0..3>, PFI <8..11>, many internal signals
USB-6212/6216	PFI <0..15>, many internal signals
FIFO	1,023 samples
Data transfers	USB Signal Stream, programmed I/O

Frequency Generator

Number of channels	1
Base clocks	10 MHz, 100 kHz
Divisors	1 to 16
Base clock accuracy	50 ppm
Output can be available on any output PFI terminal.	

External Digital Triggers

Source	
USB-6210/6211/6215/6218	PFI <0..3>, PFI <8..11>
USB-6212/6216	PFI <0..15>
Polarity	Software-selectable for most signals
Analog input function	Start Trigger, Reference Trigger, Pause Trigger, Sample Clock, Convert Clock, Sample Clock Timebase
Analog output function	Start Trigger, Pause Trigger, Sample Clock, Sample Clock Timebase
Counter/timer functions	Gate, Source, HW_Arm, Aux, A, B, Z, Up_Down

Bus Interface

USB	USB 2.0 Hi-Speed or Full-Speed ¹
USB Signal Stream (USB)	4, can be used for analog input, analog output, counter/timer 0, counter/timer 1

Power Limits

+5 V terminal as output ²	
Voltage	4.6 to 5.2 V
Current (internally limited)	50 mA max, shared with digital outputs
+5 V terminal as input ²	
Voltage	4.75 to 5.35 V
Current	350 mA max, self-resetting fuse



Caution Do not exceed 16 mA per DIO pin.

Protection..... ±10 V

Power Requirements

Input voltage on USB-621x USB port	4.5 to 5.25 V in configured state
Maximum inrush current	500 mA
No load typical current	320 mA at 4.5 V
Maximum load	
Typical current	400 mA at 4.5 V
Suspend current	260 µA, typical

Physical Characteristics

Enclosure dimensions (includes connectors)	
USB-621x Screw Terminal	16.9 × 9.4 × 3.1 cm (6.65 × 3.70 × 1.20 in.)
USB-621x Mass Termination	19.3 × 9.4 × 3.1 cm (7.61 × 3.68 × 1.20 in.)
USB-621x BNC	23.5 × 11.2 × 6.4 cm (9.25 × 4.40 × 2.50 in.)

Weight

USB-621x Screw Terminal	206 g (7.2 oz)
USB-6212 Mass Termination	227 g (8.0 oz)
USB-6216 Mass Termination	231 g (8.1 oz)
USB-6212/6216/6218 BNC	950 g (33.5 oz)
USB-6210 OEM	73 g (2.5 oz)
USB-6212/6216/6218 OEM	76 g (2.6 oz)

I/O connectors

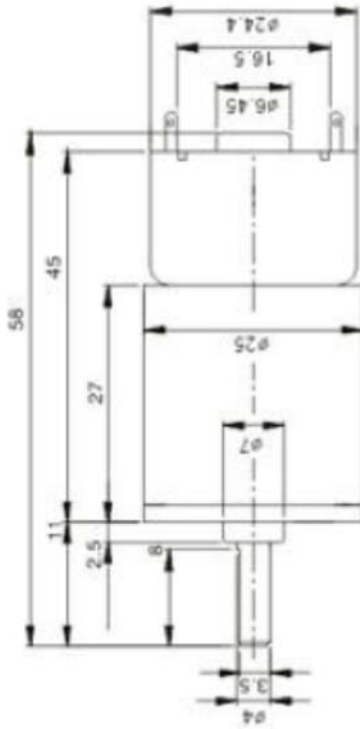
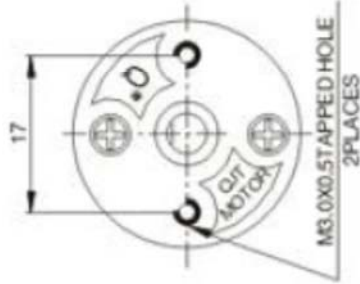
USB-6210/6211/6215	Two 16-position combicon
USB-6212/6216/6218 Screw Terminal	Four 16-position combicon
USB-6212/6216 Mass Termination	One 68-pin SCSI
USB-6212/6216/6218 BNC	19 BNCs and 26 screw terminals

USB connector	Series B receptacle
Screw terminal wiring	16 to 28 AWG
Torque for screw terminals	0.22–0.25 N · m (2.0–2.2 lb · in.)

¹ If you are using a USB M Series device in Full-Speed mode, device performance will be lower and you will not be able to achieve maximum sampling/update rates.

² USB-621x Screw Terminal/BNC devices have a self-resetting fuse that opens when current exceeds this specification. USB-621x Mass Termination devices have a user-replaceable socketed fuse that opens when current exceeds this specification. Refer to the *NI USB-621x User Manual* for information about fuse replacement.

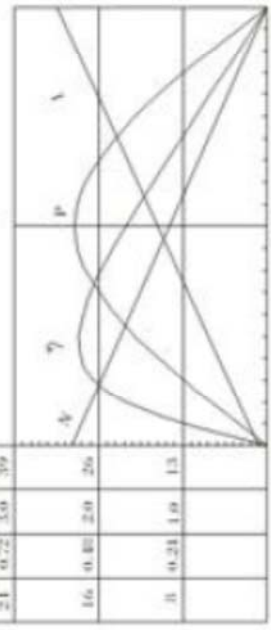
QJT-25JS-B



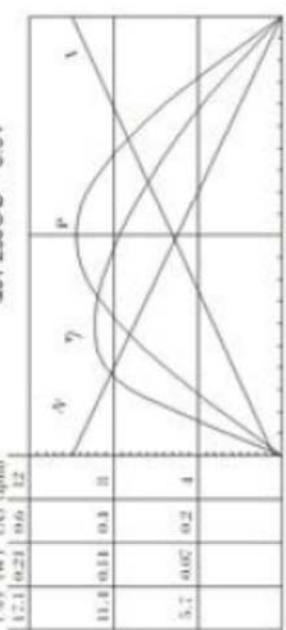
WEIGHT: 74.0g (APPROX)

MODEL	VOLTAGE RATED	NO LOAD			AT MAXIMUM EFFICIENCY			STALL		
		SPEED	CURRENT	SPEED	CURRENT	TORQUE	OUTPUT	TORQUE	TORQUE	CURRENT
	V	rpm	A	rpm	A	g.cm	W	g.cm	mN.m	A
QJT-25JS-B	3	30	0.20	23.5	0.70	1500	0.37	6944	600	2.5
	6	10	0.07	7.3	0.20	1788	0.13	6622	650	0.5

EFF. P I N (%) (W) (A) (rpm)

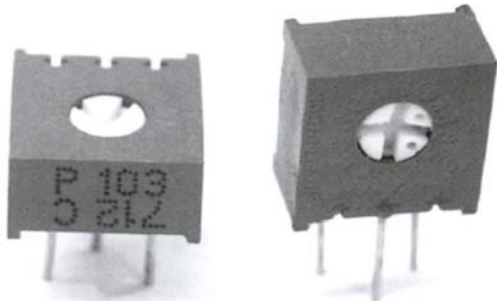


EFF. P I N (%) (W) (A) (rpm)





MODEL NO.3386



FEATURES :

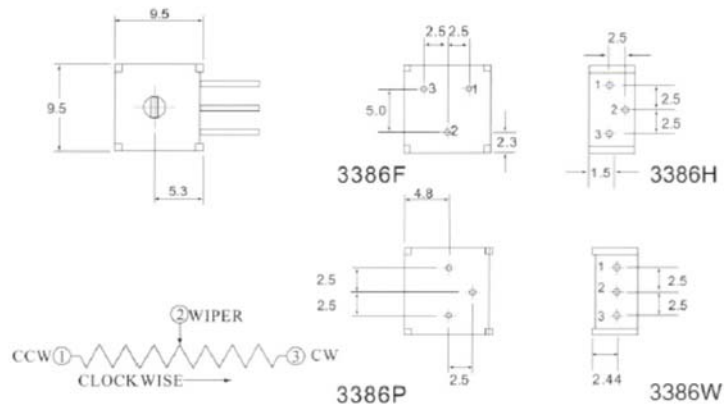
- 3/8" Square Shape
- Cermet/ Industrial/ Sealed
- Single Turn with a Unique Centre Tapped
- Vertical/ Horizontal Adjust Types Available
- Available with Extended Shaft/ Cross-Slot Rotor
- Low PCB Profile (P/ F Models) - Only 1/5" High

HOW TO ORDER

Model 3386 P -103
 Style _____
 Resistance Code _____

OUTLINE DRAWING & DIMENSIONS (mm)

Standard Resistance Table	
Resistance (Ω)	Resistance Code
50	500
100	101
200	201
500	501
1,000	102
5,000	202
10,000	502
20,000	103
50,000	203
100,000	503
200,000	104
500,000	204
1000,000	504
200,000	105



Electrical Characteristics

Power Rating0.5W @ 70°C 0W @ 125°C
Resistance Range50 Ω ~ 1M Ω
Insulation Resistance1G Ω
Contact Resistance Variation1% or 20 Ω
End Resistance1% or 2 Ω
Max. Operating Voltage300V

Mechanical Characteristics

Effective Electrical Travel (Turns)270°
Rotational Torque \leq 35mNm

Environmental Characteristics

Operating Temperature Range	...-55 °C ~ +125 °C
Temperature Coefficient \pm 100ppm/°C

		Pressure	Velocity	Temperature
Models:		Range / Resolution:		
ST650 M	ST650 I	Pressure:		
●		Pa	± 0.4 to 999.9	± 1000 to 5000
●		KPa	± 0.4 to 99.9 Pa	± 100 to 999 Pa ± 1.00 to 5.00 KPa
●		mbar	± 0.000 to 0.999	± 1.00 to 9.99 ± 10.0 to 50.0
●		mmH ₂ O	± 0.000 to 0.999	± 1.00 to 9.99 ± 10.0 to 99.9 ± 100 to 510
	●	inH ₂ O	± 0.000 to 0.999	± 1.00 to 9.99 ± 10.0 to 20.0
●		mmHg	± 0.000 to 0.999	± 10.00 to 37.51
	●	inHg	± 0.000 to 0.999	± 1.00 to 1.47
	●	PSI	± 0.000 to 0.726	
		Velocity : dpm - i Ellipsoidal		
●		m/sec	1.00 to 30.0	2.00 to 90.0
	●	ft/min	197 to 5905	394 to 17700
		Temperature (with K – type probe):		
●	●	°C	± 0.0 to 500.0	
●	●	°F	± 0 to 932	

Accuracy:

Pressure at 20°C,
 Velocity with Ellipsoidal type at 16°C, 1000 mbar:
 Readings < 100 counts ± 2 counts.
 Readings > 100 counts ± 1% of reading ± 1 count

Velocity with dpm-i type at 16°C, 1000 mbar:
 ± 3% of reading or ± 0.05 m/sec (10 ft/min)
 ± 1 count whichever is greater.

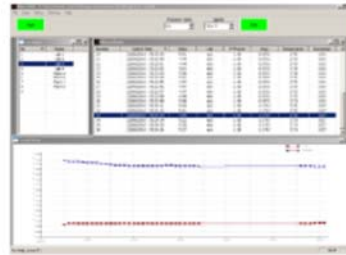
Temperature at 20°C:
 ± 2°C (36°F)

Velocity with Ellipsoidal Pitot Tube:



DpmUsb Software:

Downloading data:



Monitoring:



DpmUsb Software can be used for downloading data and / or for monitoring.

DpmUsb Software allows the engineer to select the Auto Zero time, the Auto Store time and the default temperature and barometer settings; 10 Pitot Tube Factors and 10 K Factors can be stored on the PC.

Data can be viewed and printed in report and / or graph form; it can also be arranged in a database with the engineer choosing the visible fields, location names and how the data is organised.

The on-screen multi-view display offers a choice of digital monitors and gauges with the maximum and minimum values of all gauges being user set.



- L6D load cells are available in the capacities 2.5kg~50kg.
- Aluminum construction with parallel beam.
- Silicon adhesive sealed, surface anodized and anti-corrosion.
- Integral structure and easy installation.
- Suitable for pricing scale, platform scale and other electronic weighing devices.

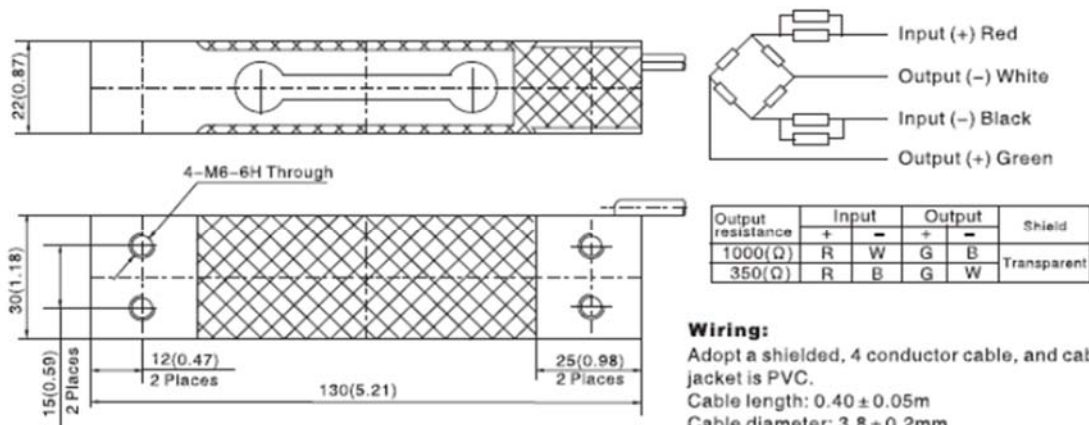
Features

- Capacity: 2.5kg~50kg
- High accuracy
- Max. platform size: 250×350mm
- OIML Certificates No:R60/2000-CN-00.05 Revision 1
- PTB Approval No:D09-03.20 Revision 1



Specifications		2.5/3/5/6/8/10/15/20/30/35/40/50		
Capacity	kg			
Accuracy		C3D	C3	C3G
Approvals		OIML R60 C3		
Maximum number of verification intervals	n _{max}	2500	3000	4000
Minimum load cell verification interval	v _{min}	E _{max} /5000	E _{max} /7000	E _{max} /11000
Combined error	(%FS)	≤ ±0.030	< ±0.020	< ±0.015
Creep	(%FS/30min)	≤ ±0.020	< ±0.0167	< ±0.0125
Temperature effect on sensitivity	(%FS/10℃)	≤ ±0.021	< ±0.0175	< ±0.0131
Temperature effect on zero	(%FS/10℃)	≤ ±0.028	< ±0.020	< ±0.0127
Output sensitivity	(mv/v)	2.0 ± 0.2		
Input resistance	(Ω)	409 ± 6/1065 ± 15		
Output resistance	(Ω)	350 ± 3/1000 ± 10		
Insulation resistance	(MΩ)	> 5000(50VDC)		
Zero balance	(%FS)	2		
Temperature, compensated	(℃)	-10 ~ +40		
Temperature, operating	(℃)	-35 ~ +65		
Excitation, recommended	(V)	5 ~ 12(DC)		
Excitation, max	(V)	18(DC)		
Safe overload	(%FS)	150		
Ultimate overload	(%FS)	300		
Corner correction		0.02%load value/100mm		

Outline Dimension mm(inch)



Wiring:

Adopt a shielded, 4 conductor cable, and cable jacket is PVC.
Cable length: 0.40 ± 0.05m
Cable diameter: 3.8 ± 0.2mm

Appendix D: DERIVATION OF UNCERTAINTY

The following chapter details the derivation of the equations used to calculate the uncertainties in the measured data. A data set was recorded for each test condition that was to be investigated. The loadcell data contained in these sets were the filtered and averaged results of the raw data discussed in chapter 6.3. Each data set comprised the signals from the rolling, yawing and hinge moment loadcells, the potentiometer and the temperature thermocouple.

Signal Uncertainty

The uncertainty in the signal data was calculated by first calculating the standard deviation for the respective data set. The equation below was used for the calculation of the standard deviation.

$$\sigma = \left(\frac{\sum x^2}{n} - \bar{x}^2 \right)^{1/2} \quad \text{D.1}$$

A confidence interval of 1.96, relating to a 95% confidence level, was applied to the standard deviation to calculate the uncertainty in the input voltage. The uncertainties in the excitation voltage, V_{EX} , and loadcell gain, G , were included in the uncertainty for each loadcell strain reading using the equation below.

$$\frac{\Delta\varepsilon}{\varepsilon} = \left(\left(\frac{\Delta V_{in}}{V_{in}} \right)^2 + \left(\frac{\Delta G}{G} \right)^2 + \left(\frac{\Delta V_{EX}}{V_{EX}} \right)^2 \right)^{1/2} \quad \text{D.2}$$

Calibration Uncertainty

The uncertainty in the calibration gradients was calculated using the derived equation, below

$$\frac{\Delta R}{R} = \left(\left(\frac{\Delta\varepsilon}{\varepsilon} \right)^2 + \left(\frac{\Delta L'}{L'} \right)^2 \right)^{1/2} \quad \text{D.3}$$

Where R is the calibration gradient (for the rolling moment loadcell as an example)

The uncertainty in the applied load was calculated using the derived equation below

$$\frac{\Delta L'}{L'} = \left(\left(\frac{\Delta m}{m} \right)^2 + \left(\frac{\Delta x}{x} \right)^2 + \left(\frac{\Delta \theta}{\theta} \right)^2 + \left(\frac{\Delta \alpha}{\alpha} \right)^2 \right)^{1/2} \quad \text{D.4}$$

Where m is the mass of the applied mass pieces, g; x is the moment arm, mm; θ and α is the alignment of the applied load, rad.

Moment Uncertainty

The uncertainty in the rolling and yawing moment loads and aileron deflection was found using the calculated uncertainty in the loadcell signal, given by equation D.2, and the uncertainty due to the calibration process. This uncertainty in the moment loads was derived from the from the calibration matrix, below.

$$\begin{bmatrix} L' \\ N' \end{bmatrix} = [A]^{-1} \begin{bmatrix} Sig_R \\ Sig_Y \end{bmatrix} \quad D.5$$

Where Sig_R Signal from rolling moment loadcell; Sig_Y Signal from yawing moment loadcell; $[A]$ is the calibration matrix in the form

$$[A] = \begin{bmatrix} R_1 & R_2 \\ Y_1 & Y_2 \end{bmatrix} \quad D.6$$

Where R_1, R_2, Y_1 and Y_2 Calibration gradients

The inverse calibration matrix was calculated using the equation below

$$[A]^{-1} = \frac{1}{|A|} \begin{bmatrix} Y_2 & -R_2 \\ -Y_1 & R_1 \end{bmatrix} \quad D.7$$

From equation D.5, the equations for the uncertainty in the rolling and yawing moments, given below, were derived.

$$\begin{aligned} \Delta L' = & \left(\frac{Y_2^2 S_R}{|A|^2} \left(\left(\frac{\Delta Sig_R}{Sig_R} \right)^2 + \left(\frac{\Delta Y_2}{Y_2} \right)^2 + \left(\frac{\Delta |A|}{|A|} \right)^2 \right) \right. \\ & \left. + \frac{R_2^2 S_Y}{|A|^2} \left(\left(\frac{\Delta Sig_Y}{Sig_Y} \right)^2 + \left(\frac{\Delta R_2}{R_2} \right)^2 + \left(\frac{\Delta |A|}{|A|} \right)^2 \right) \right)^{1/2} \end{aligned} \quad D.8$$

$$\begin{aligned} \Delta N' = & \left(\frac{Y_1^2 S_R}{|A|^2} \left(\left(\frac{\Delta Sig_R}{Sig_R} \right)^2 + \left(\frac{\Delta Y_1}{Y_1} \right)^2 + \left(\frac{\Delta |A|}{|A|} \right)^2 \right) \right. \\ & \left. + \frac{R_1^2 S_Y}{|A|^2} \left(\left(\frac{\Delta Sig_Y}{Sig_Y} \right)^2 + \left(\frac{\Delta R_1}{R_1} \right)^2 + \left(\frac{\Delta |A|}{|A|} \right)^2 \right) \right)^{1/2} \end{aligned} \quad D.9$$

The uncertainty in the applied loading and direction of the loading was taken into account in the uncertainty of gradients calculated for each calibration.

The equation for the uncertainty of the aileron hinge moment was simpler as there was no cross coupling between the hinge moment loadcell and any other loadcell. The equation is given below.

$$\frac{\Delta H_a}{H_a} = \left(\left(\frac{\Delta A_H}{A_H} \right)^2 + \left(\frac{\Delta Sig_H}{Sig_H} \right)^2 \right)^{1/2} \quad D.10$$

Where A_H Calibration gradient of hinge moment loadcell.

The uncertainty values and their sources for the equations shown above are discussed in chapter 7.

Aerodynamic Coefficient Uncertainty

The uncertainties in the aerodynamic coefficients were calculated using the following equations, derived from the equations in chapter 2.2.

$$\frac{\Delta C_l'}{C_l'} = \left(\left(\frac{\Delta L'}{L'} \right)^2 + \left(\frac{\Delta q}{q} \right)^2 + \left(\frac{\Delta S}{S} \right)^2 + \left(\frac{\Delta b}{b} \right)^2 \right)^{1/2} \quad \text{D.11}$$

$$\frac{\Delta C_n'}{C_n'} = \left(\left(\frac{\Delta N'}{N'} \right)^2 + \left(\frac{\Delta q}{q} \right)^2 + \left(\frac{\Delta S}{S} \right)^2 + \left(\frac{\Delta b}{b} \right)^2 \right)^{1/2} \quad \text{D.12}$$

$$\frac{\Delta C_{h_a}}{C_{h_a}} = \left(\left(\frac{\Delta H_a}{H_a} \right)^2 + \left(\frac{\Delta q}{q} \right)^2 + \left(2 \frac{\Delta c_a}{c_a} \right)^2 + \left(\frac{\Delta b_a}{b_a} \right)^2 \right)^{1/2} \quad \text{D.13}$$

The values obtained from the above equations are discussed in chapter 8.

Appendix E: LOADCELL RESOLUTION CHECK SETUP AND PROCEDURES

E.1. External Balance Loadcells

Each loadcell that was to be installed in the external balance was rigged up to the rigid steel plates and clamped to a flat surface. In this way it was possible to ensure the loadcell was level and no off axis loading was applied to the loadcell. Once a loadcell was tested it was turned over and the load applied once more, effectively loading the loadcell in both directions.

The following mass pieces were used, with readings being taken with each addition of load, until all 6 mass pieces were applied, and each subtraction of a mass piece until a zero load case was reached. This allow for hysteresis to be checked. All mass pieces were measured to within $\pm 0.05\text{g}$ accuracy.

Table E.1: Mass loads applied during calibration of external balance loadcells

Load order	Applied Load [g]
1	1000.8
2	2001.8
3	2910.5
4	3818.9
5	4727.0
6	5727.6

E.2. Hinge Moment Balance Loadcell

The setup used is shown in Figure E.1. The nylon cable used to suspend the loadcell was tied in such a way as to all the loadcell to freely hang preventing the mass pieces applying a load off the main loading axis of the loadcell.

The following mass pieces were used during the direct calibration of the hinge moment loadcell. All mass pieces were measured to a 0.05g precision.

Table E.2: Mass loads applied during direct calibration of hinge moment loadcell

Load Order	1	2	3	4	5	6	7
Mass (g)	101.6	200.1	299.6	398.9	499.2	597.7	695.9
Load Order	8	9	10	11	12	13	14
Mass (g)	794.3	892.8	992.1	2113.1	2613.4	3113.8	4114.9

The loadcell was tested in tension by suspending the loadcell and applying extra mass slung beneath it. This test was repeated three times to check for consistency. The loadcell was also

checked with a compressive load by resting the loadcell on a flat surface and applying a direct load. This was done simply to confirm that the signal to load relationship was the same in both compression and tension and was not repeated. For each test data was recorded for a minute before the next mass was added.



Figure E.1: Setup used in the calibration of the hinge moment loadcell through the application of load directly to the loadcell.

Appendix F: CALIBRATION SETUP AND PROCEDURES

F.1. External Balance

Both axes, namely rolling and yawing moment, were calibrated separately. A simple rig, involving a T bar was fixed to the balance using the common mount at the top of the balance arm. Holes were drilled into the T bar through which cables could be looped. Pulleys were suspended from the roof of the wind tunnel by cable and anchored to the side wall by a further cable. By using this arrangement the location of the pulleys could be more accurately fixed. This prevented the pulley shifting position as the load was increased, thereby maintaining the direction the load was applied in. An example of this setup, as used for the rolling moment calibration, is shown in Figure F.1.

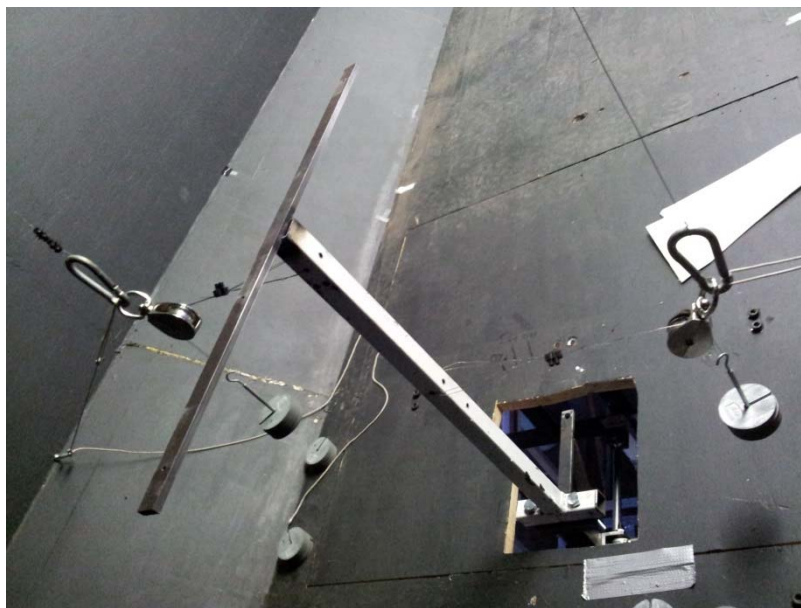


Figure F.1: Calibration setup used for rolling moment calibration

The configuration setup for each axes is shown in Figure F.2 for the yawing (a), and rolling (b) moments. The red lines are indicate how the moments were applied, the direct reversed to create both positive and negative moments. The alignment of the rig and applied loads were done through a combination of digital protractor and by eye. The uncertainty in the alignment of the applied loading was taken as a conservative $\pm 1^\circ$. This was based on the alignment of certain components by eye, the layout and configuration of the calibration rig making other forms of measurement impractical.

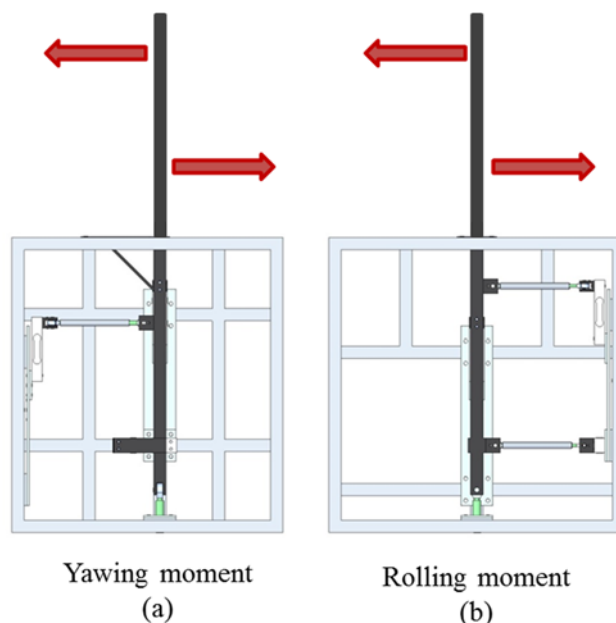


Figure F.2: External Balance calibration configuration

The following mass pieces and moment arms, shown in Table F.1, were used during the calibration of the external balance for the three axes. Mass piece 4 was only applied for the rolling moment calibration as theoretical data did not predict values requiring higher loads for the yawing and pitching moments. Calibrations were repeated multiple times with readings taken for the masses applied and then removed to ensure hysteresis. All mass pieces were measured to within a 0.05g accuracy and dimensions measured to within 0.5mm.

Table F.1: Moment arms and masses applied during calibration

Calibration	Moment Arm [mm]	Load order	Mass [g]
Rolling Moment	195	Mass Piece 1	299.5
Yawing Moment	195	Mass Piece 2	298.1
		Mass Piece 3	295.1
		Mass Piece 4	1223.4

F.2. Hinge Moment Balance

Calibration of the hinge moment balance was accomplished by first securing the wing to a level surface, through the use of the same mounting jigs and a digital protractor. A modified aileron rib, as used in the aileron test pieces, was then secured to the aileron leading edge rod, the rib having a hole drilled in a precise location aft of the hinge line. Nylon coated steel wire was then threaded through the rib and a mass hanger secured on which the load could be applied. This setup is shown in Figure F.3.

Unlike the calibration procedure followed for the rolling and yawing moment, the procedure for the hinge moment balance was seen as being less susceptible to errors. As the load was applied directly to the aileron it would be self-aligning, the mass pieces always pointing downwards in

the direction of gravity. As the wings was then levelled to within $\pm 0.02^\circ$, due to the digital protractor, the alignment of the applied loading was therefore much more accurate than the $\pm 1^\circ$ used for the rolling and yawing moment calibration. The moment arm could be determined using the measurements of the calibration rib and on the deflection of the aileron rib which could be measured due to the calibration specified in chapter 7.3.

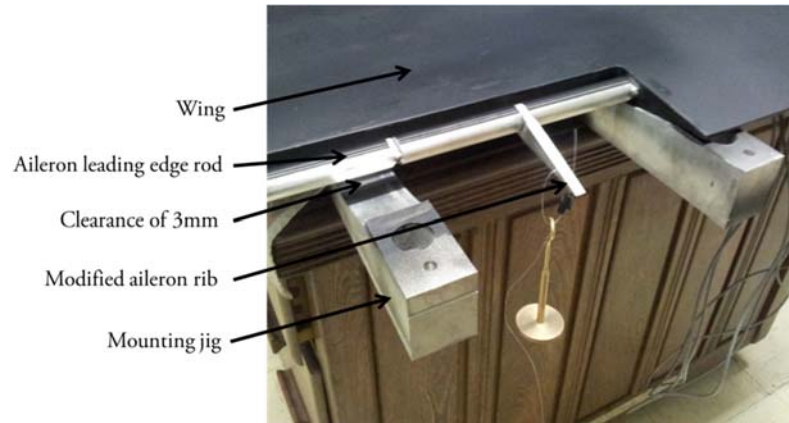


Figure F.3: Hinge moment balance calibration setup.

The following moments were applied during the calibration of the hinge moment measurement balance. A moment arm of 27mm was used. All mass pieces were measured to within $\pm 0.0005\text{g}$ accuracy and moments arms to within $\pm 0.01\text{mm}$. An accuracy of 0.0005g was assured through the use of a chemical balance.

Table F.2: Moment loads applied during calibration of hinge moment measurement balance

Load Order	Applied Moment [N.m]
1	0.0255
2	0.0561
3	0.0868
4	0.1175

Gravity was taken as 9.785m/s^2

F.3. Aileron Deflection

For the calibration of the aileron deflection one of the aileron test pieces was installed on the wind tunnel model and a dial gauge mounted beside it. The dial gauge pin was positioned at a select point on the aileron on the outboard side closet to the potentiometer. Figure F.4 illustrates this configuration. The lateral placement of the gauge pin from the aileron axis was based on the maximum travel allowed by the dial gauge.

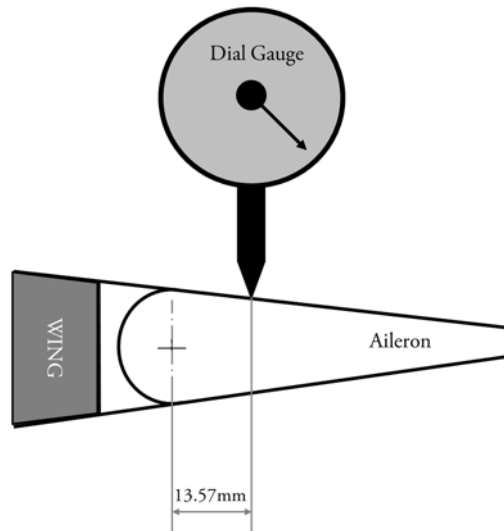


Figure F.4: Aileron Deflection calibration configuration

The dial gauge had an uncertainty of $\pm 0.005\text{mm}$ and its placement from the aileron hinge axis was accurate to within $\pm 0.01\text{mm}$.

The aileron was deflected through its full range of movement. The potentiometer input voltage and dial gauge reading were recorded at each position. Plotting these data points allowed for the relationship between the dial gauge displacement and pot voltage to be determined.

Recreating the system in a CAD software package allowed for aileron deflection to be adjusted and the virtual dial gauge pin displacement to be measured. Measurements added into the CAD software were accurate to $\pm 0.01\text{mm}$. This allowed for the relationship between the dial gauge displacement and aileron deflection to be determined. By combining the two calculated data trends it was possible to calculate the aileron deflection directly from the measured voltage across the potentiometer.

Appendix G: EXTERNAL BALANCE CROSS COUPLING EFFECT

As shown in chapter 7.1 the yawing moment loadcell would experience a negative load as a rolling moment was applied, regardless of the direction of the rolling moment. This meant that separate calibration matrices had to be used depending on whether a positive or negative rolling moment was measured during testing.

Though an unexpected result the reasons behind the data trends can be explained. Figure G.1 shows an exaggerated case that occurred during the rolling moment calibration. Illustrated is the balance arm, yawing moment loadcell and connector arms between the two. Figure G.1 (a) and (c) represent the balance movement during a positive and negative rolling moment respectively. Figure G.1 (b) represents the system in the unloaded case. Movement of the balance arm in the manner depicted is due to the way in which the balance was designed, the resulting cross coupling effect being an unanticipated result.

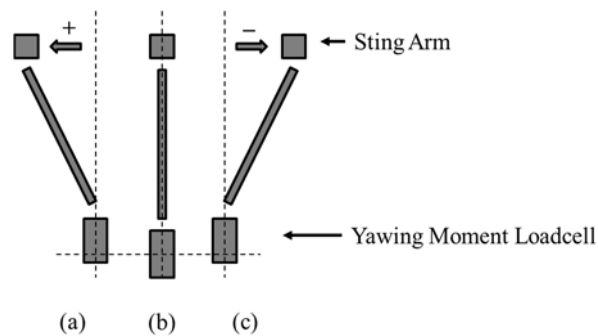


Figure G.1: Diagram explaining yawing moment load direction depending on applied rolling moment direction

As a rolling moment is applied to the external balance system the balance arm will deflect a small amount, this movement exaggerated in Figure G.1. The connection between the loadcell and balance arm is of a fixed distance and as such when the balance arm is displaced the loadcell will have to be displaced as well. This displacement will be picked up by the loadcell's strain gauges and a strain measurement will be recorded. The displacement of the yawing moment loadcell, however, will always be in the same direction, as illustrated in Figure G.1, irrelevant of the rolling moment direction.

This same effect would be encountered by the rolling moment loadcell. It was not taken into account, however, as the applied yawing moments, due to aerodynamic loads, was only expected in one direction.

This would have potentially introduced off axis loadings into the loadcell which could cause damage. The rose joint connections used between the balance arm and loadcells were used to prevent such a case occurring.

Appendix H: TEST PRECAUTIONS

1. Ensure that the battery charger is unplugged during the tests.
2. Before starting a test run the aileron through its full deflection range and check for any lagging or jumping in the movement indicative of an obstruction or clearance issue. Clean the area causing problems if necessary.
3. Do not touch, adjust or rest anything on the external balance during a test.
4. During testing avoid changing the direction in which the aileron is deflected, pick one direction and use that. Should the aileron move too quickly decrease the DC motor supply voltage.
5. Do not operate the aileron beyond the following deflections: $<-35^\circ$ and $>10^\circ$, otherwise it risks serious damage to the hinge moment loadcell.
6. Once the wind tunnel has been turned up to the test speed the aileron must not be deflected as this would vary the zero values for all measured loads, rendering the data obtained as useless.
7. Ensure the bolt at the wind tunnel models quarter chord point is tightened before each test otherwise there is a risk of the wing leaning against the tunnel floor.
8. Using the live plots outputted from Labview as a guideline, the data should only be recorded once a measure of stability in the data has been reached (this typically takes 15 to 30 seconds).
9. Upon conclusion of testing, return the aileron to a zero deflection

Appendix I: FULL LIST OF RESULTS

Contained in this appendix is the full list of results for the investigation of the effect of aileron trailing edge thickness. The results are separated into those for the rolling, yawing and hinge moment coefficients.

Rolling Moment Coefficient

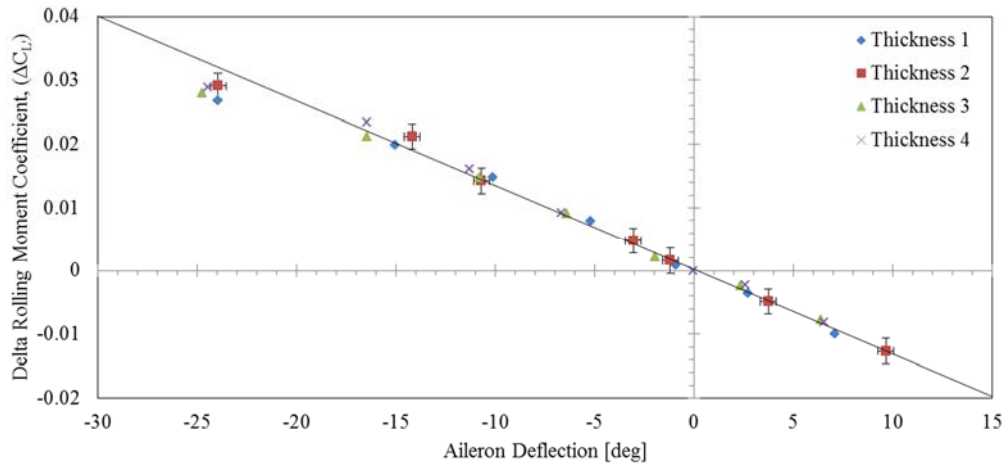


Figure I.1: Comparison of delta rolling moment coefficients for 4 aileron trailing edge thicknesses, 0° AoA, V=14.9m/s

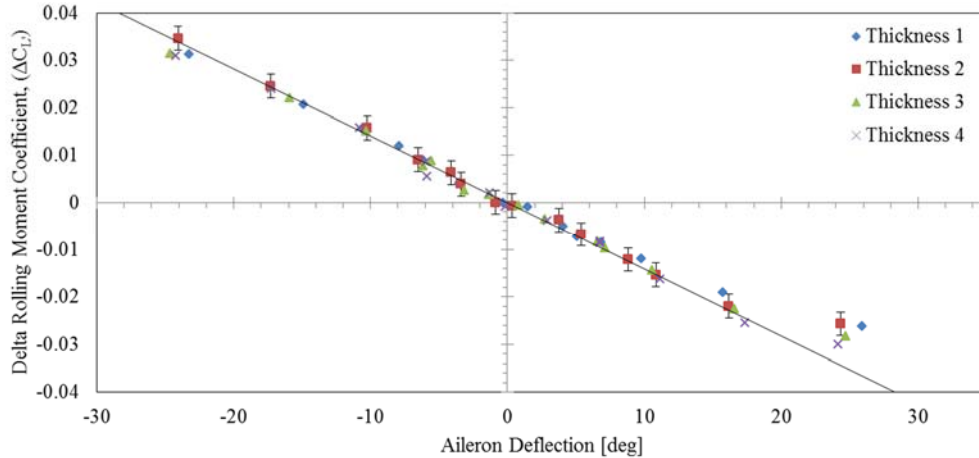


Figure I. 2: Comparison of delta rolling moment coefficients for 4 aileron trailing edge thicknesses, 5° AoA, V=14.6m/s

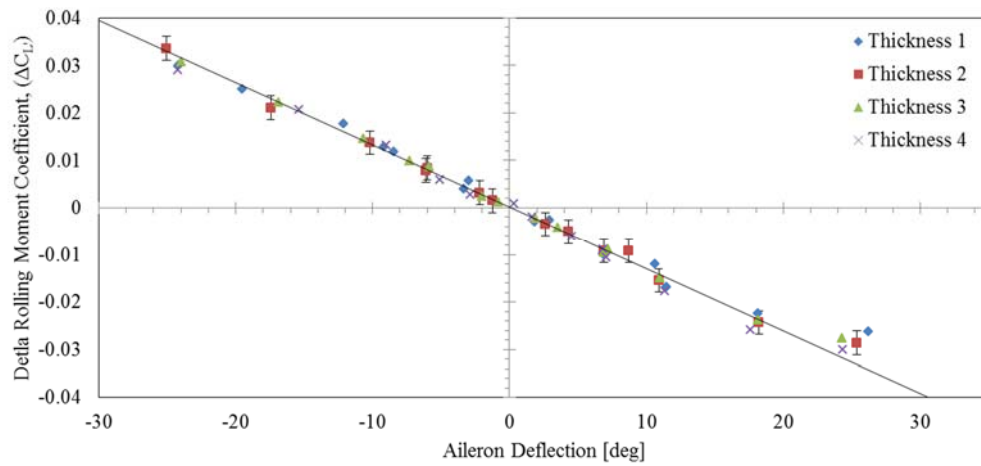


Figure I. 3: Comparison of delta rolling moment coefficients for 4 aileron trailing edge thicknesses, 10° AoA, $V=14.7\text{m/s}$

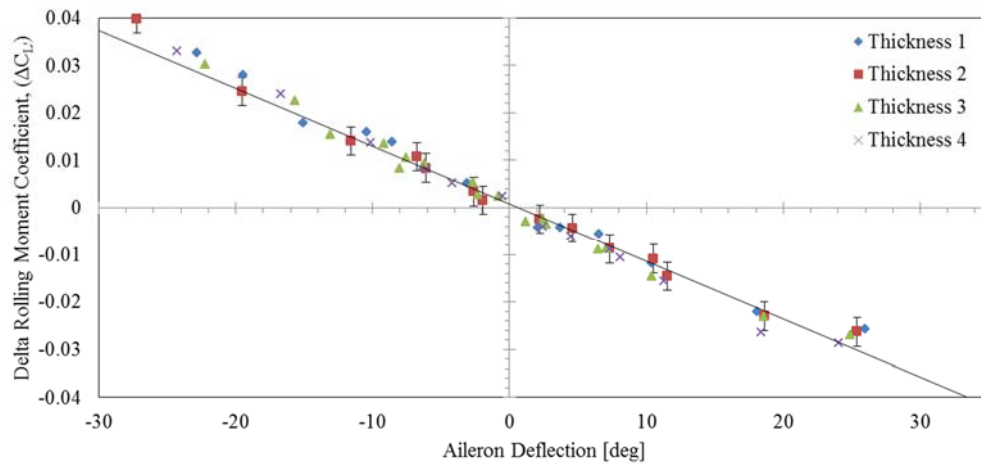


Figure I. 4: Comparison of delta rolling moment coefficients for 4 aileron trailing edge thicknesses, 12.5° AoA, $V=14.6\text{m/s}$

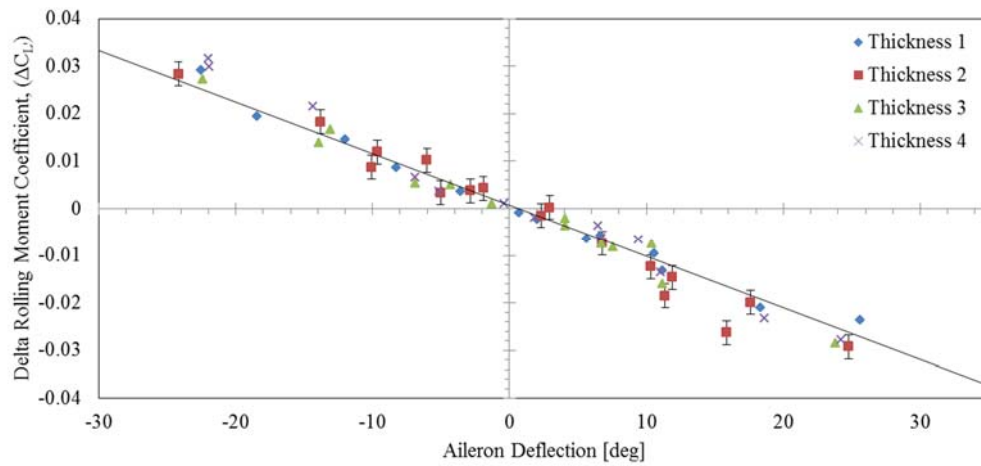


Figure I. 5: Comparison of delta rolling moment coefficients for 4 aileron trailing edge thicknesses, 15° AoA, V=14.5m/s

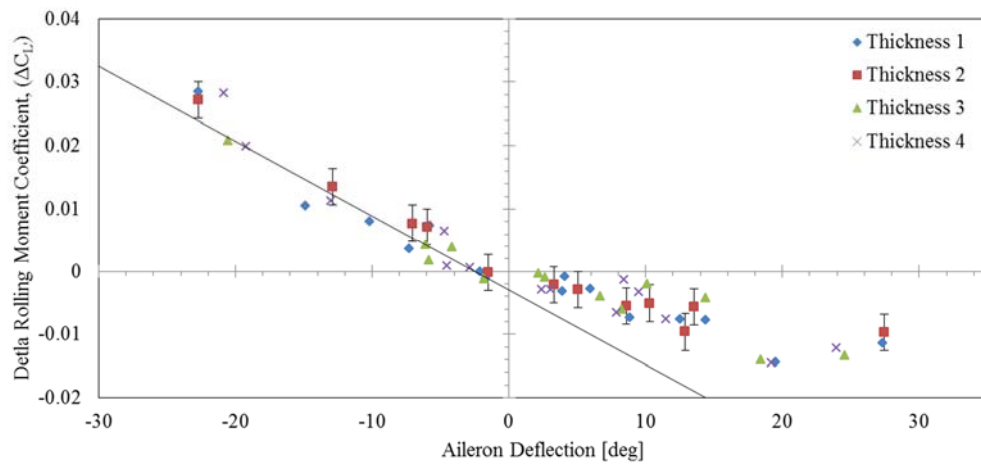


Figure I. 6: Comparison of delta rolling moment coefficients for 4 aileron trailing edge thicknesses, 17.5° AoA, V=14.7m/s

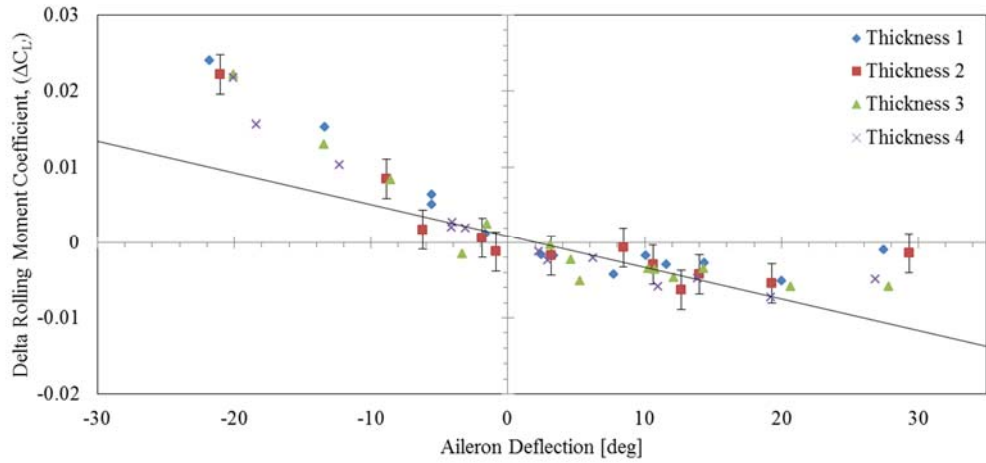


Figure I. 7: Comparison of delta rolling moment coefficients for 4 aileron trailing edge thicknesses, 20° AoA, V=14.8m/s

Yawing Moment Coefficient

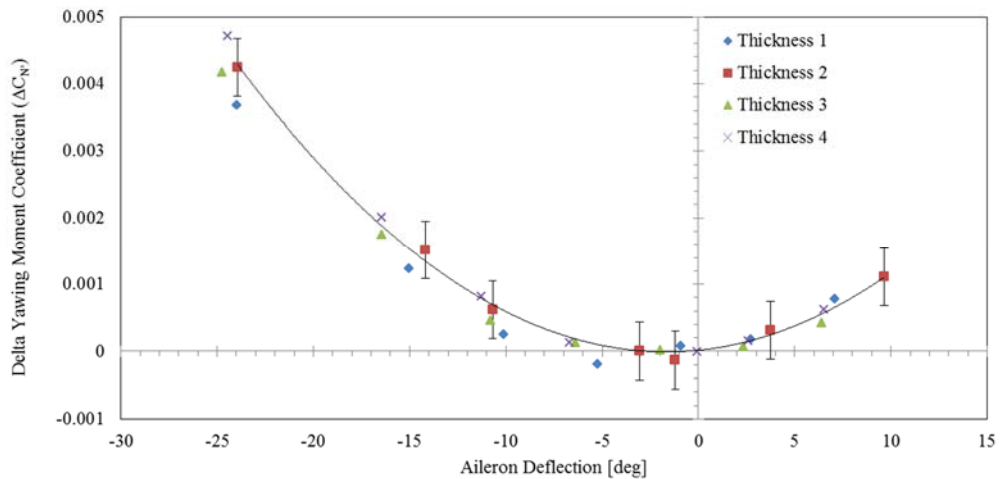


Figure I. 8: Comparison of delta yawing moment coefficients for 4 aileron trailing edge thicknesses, 0° AoA, V=14.9m/s

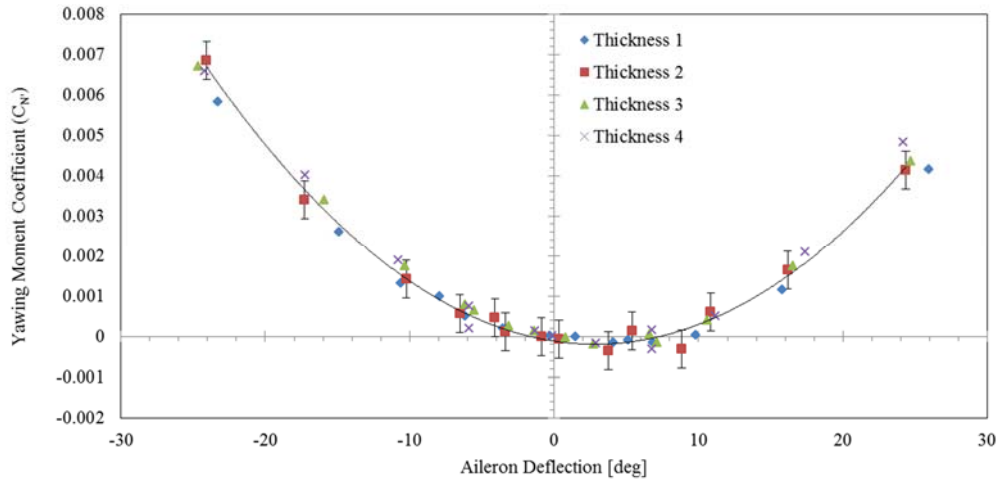


Figure I. 9: Comparison of delta yawing moment coefficients for 4 aileron trailing edge thicknesses, 5° AoA, V=14.6m/s

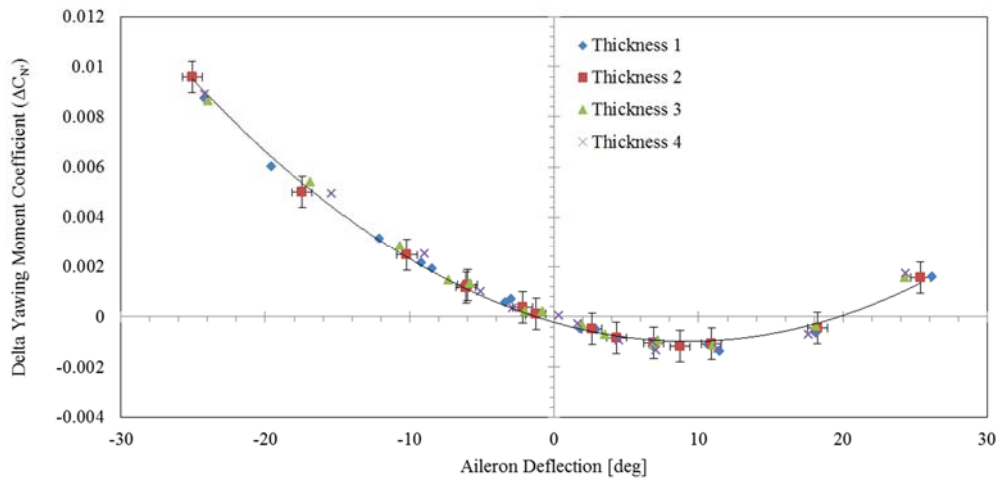


Figure I. 10: Comparison of delta yawing moment coefficients for 4 aileron trailing edge thicknesses, 10° AoA, V=14.7m/s

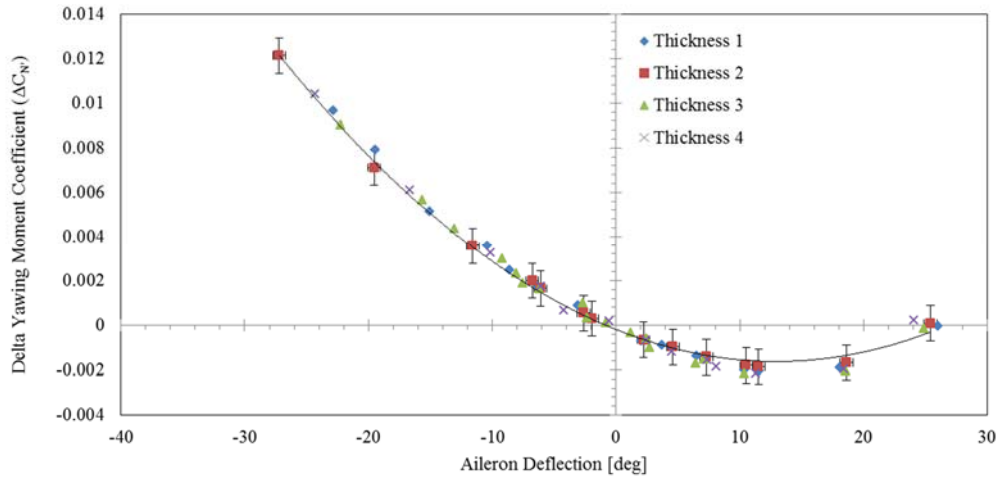


Figure I. 11: Comparison of delta yawing moment coefficients for 4 aileron trailing edge thicknesses, 12.5° AoA, V=14.6m/s

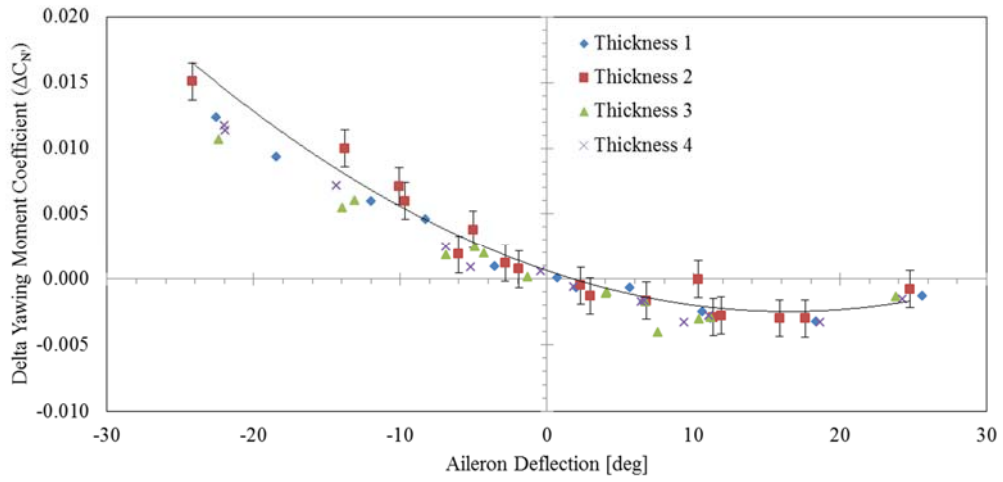


Figure I. 12: Comparison of delta yawing moment coefficients for 4 aileron trailing edge thicknesses, 15° AoA, V=14.5m/s

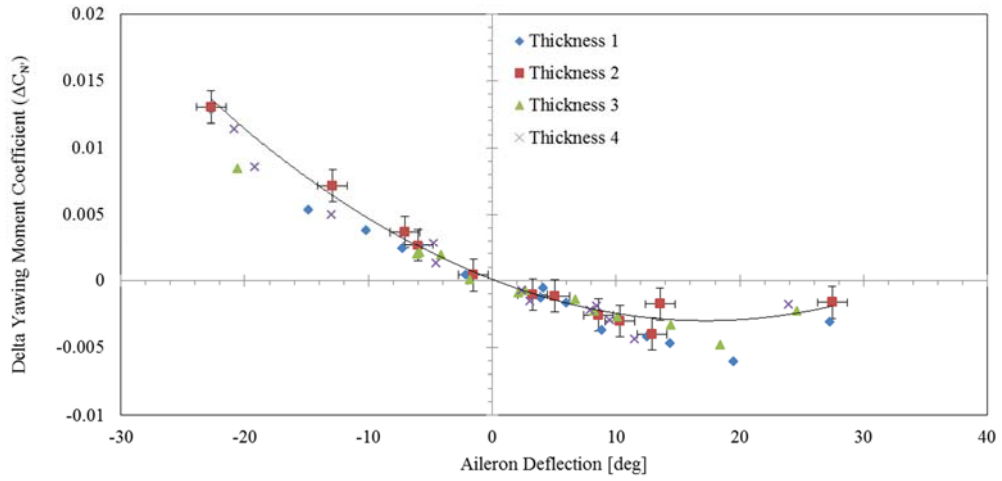


Figure I. 13: Comparison of delta yawing moment coefficients for 4 aileron trailing edge thicknesses, 17.5° AoA, V=14.7m/s

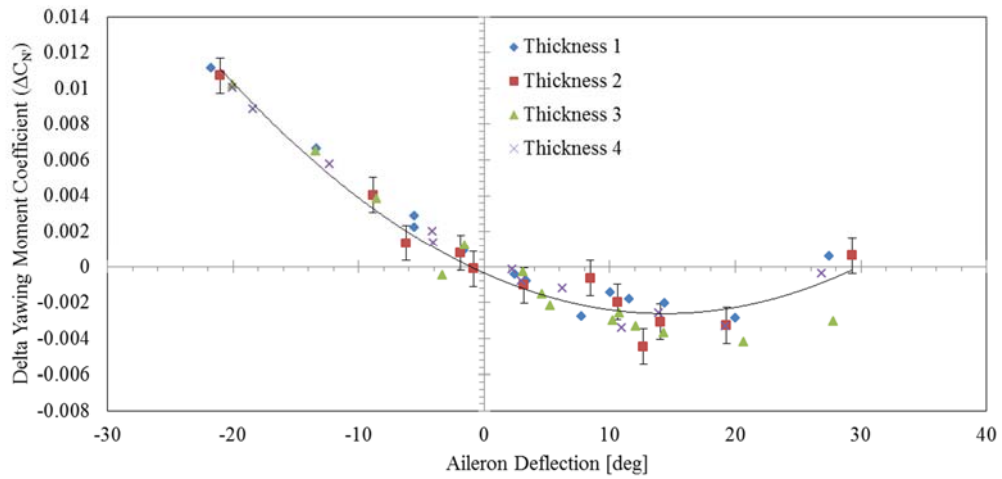


Figure I. 14: Comparison of delta yawing moment coefficients for 4 aileron trailing edge thicknesses, 20° AoA, V=14.8m/s

Hinge Moment Coefficient

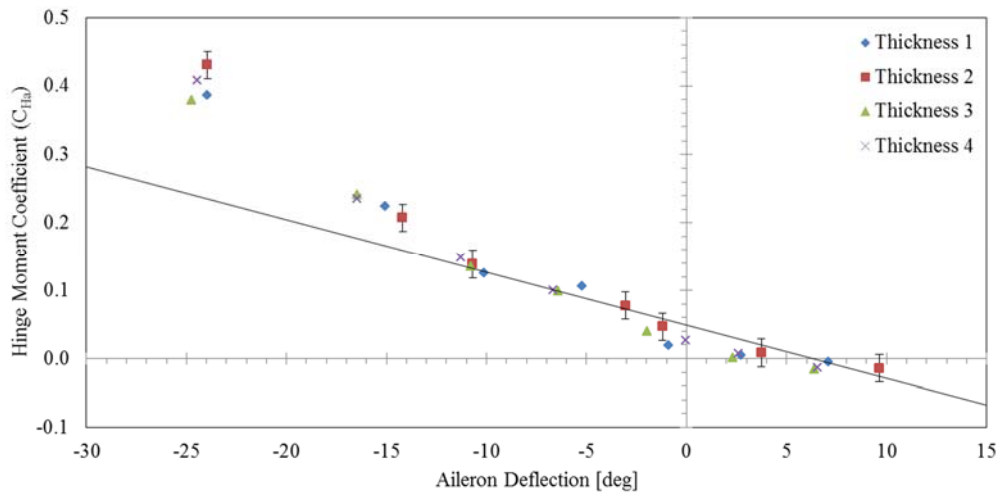


Figure I. 15: Comparison of hinge moment coefficients for 4 aileron trailing edge thicknesses, 0° AoA, $V=14.9\text{m/s}$

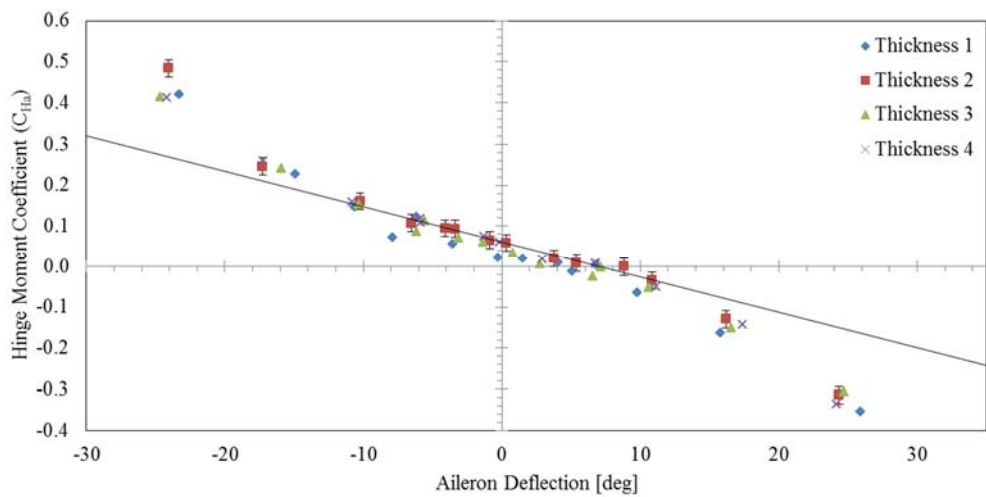


Figure I. 16: Comparison of hinge moment coefficients for 4 aileron trailing edge thicknesses, 5° AoA, $V=14.6\text{m/s}$

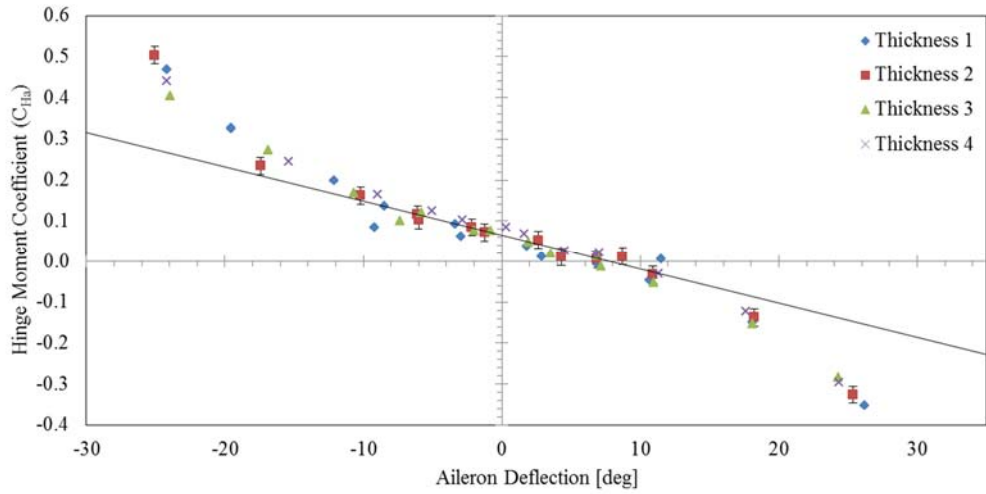


Figure I. 17: Comparison of hinge moment coefficients for 4 aileron trailing edge thicknesses, 10° AoA, $V=14.7\text{m/s}$

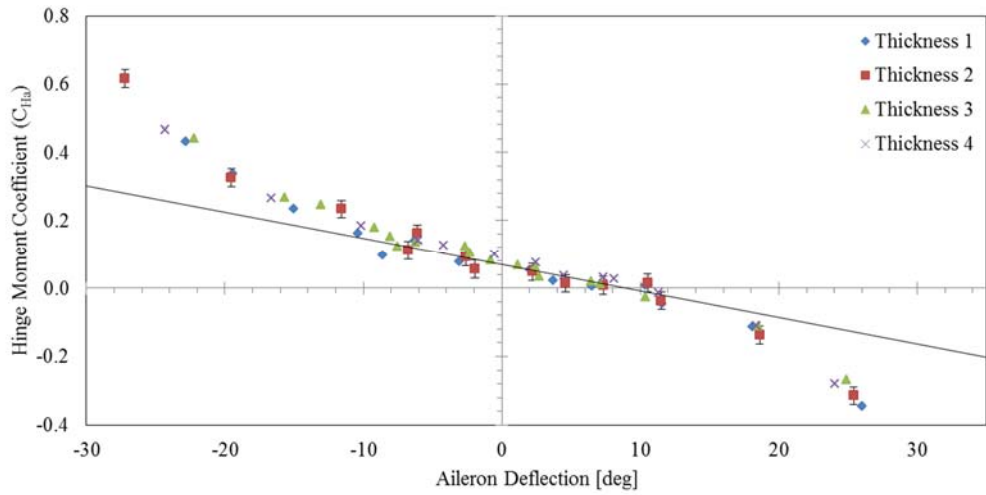


Figure I. 18: Comparison of hinge moment coefficients for 4 aileron trailing edge thicknesses, 12.5° AoA, $V=14.6\text{m/s}$

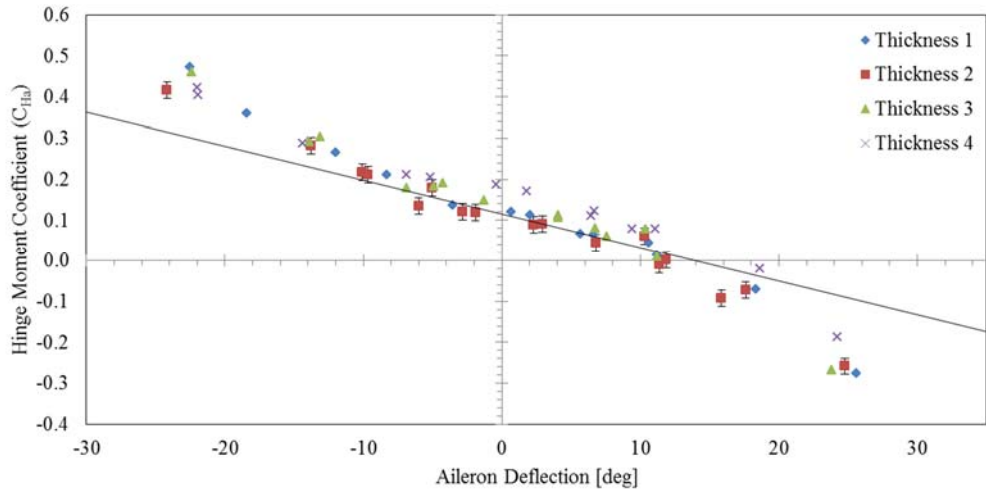


Figure I. 19: Comparison of hinge moment coefficients for 4 aileron trailing edge thicknesses, 15° AoA, V=14.5m/s

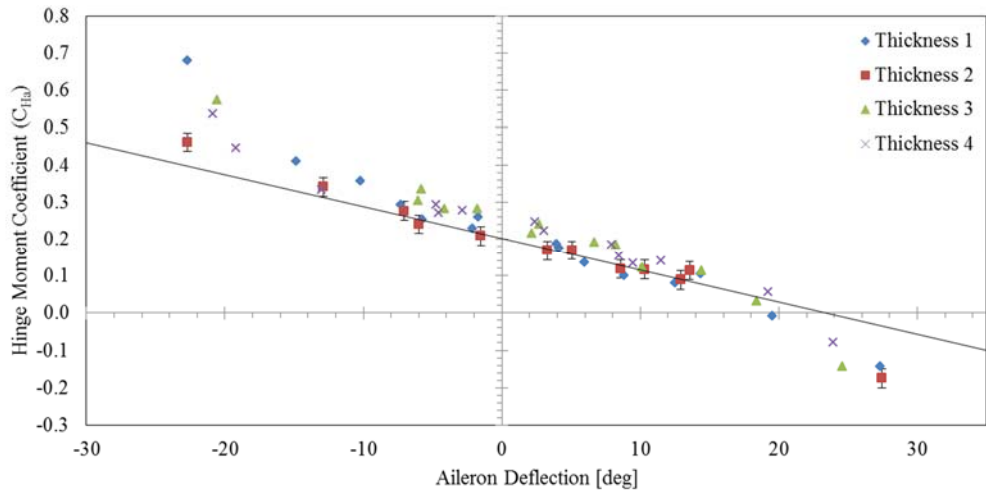


Figure I. 20: Comparison of hinge moment coefficients for 4 aileron trailing edge thicknesses, 17.5° AoA, V=14.7m/s

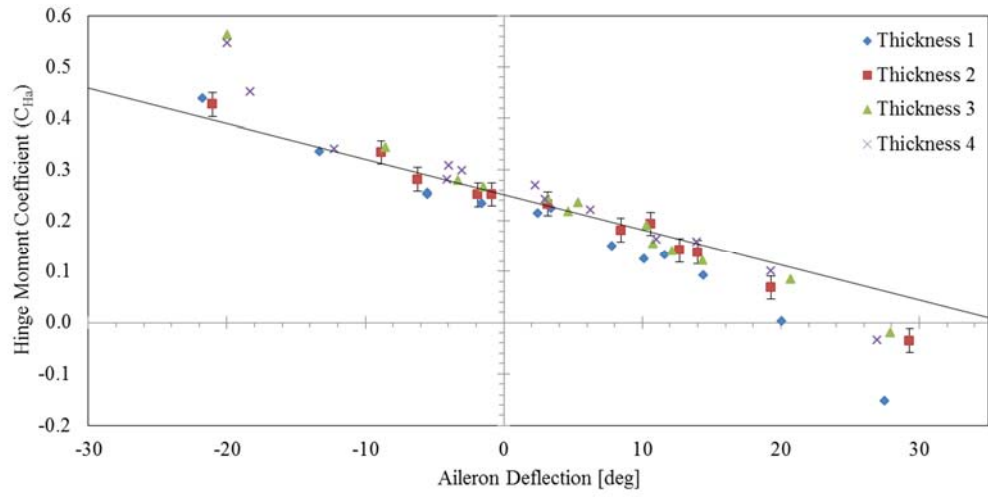


Figure I. 21: Comparison of hinge moment coefficients for 4 aileron trailing edge thicknesses, 20° AoA, V=14.8m/s